12-2013

Utilizing Persistent Scatterer Interferometry to Investigate the Nature and Factors Controlling Nile Delta Subsidence

El Hachemi Yousef Bouali

UTILIZING PERSISTENT SCATTERER INTERFEROMETRY TO INVESTIGATE THE NATURE AND FACTORS CONTROLLING NILE DELTA SUBSIDENCE

by

El Hachemi Yousef Bouali

A thesis submitted to the Graduate College
in partial fulfillment of the requirements
for the degree of Master of Science
Geosciences
Western Michigan University
December 2013

Thesis Committee:

Mohamed Sultan, Ph.D., Chair
William Sauck, Ph.D.
Robert Gillespie, Ph.D.
Richard Becker, Ph.D.

UTILIZING PERSISTENT SCATTERER INTERFEROMETRY TO INVESTIGATE THE NATURE AND FACTORS CONTROLLING NILE DELTA SUBSIDENCE

El Hachemi Yousef Bouali, M.S.

Western Michigan University, 2013

The Nile Delta in Egypt is being threatened by two continuous and relatively slow hazards: encroachment from the Mediterranean Sea as sea levels rise and land subsidence of the delta itself. The magnitude of sea level rise has been actively monitored, while the subsidence of the Nile Delta has not been adequately quantified spatially and temporally. Instead, all previous studies have either focused on measuring average Holocene subsidence rates or modern subsidence rates on local scales (point- or city-scale).

The overall study objective is three-fold: (1) to measure and map the spatial variations in subsidence rates across the entire Nile Delta, (2) to identify the nature of factors (natural and anthropogenic) controlling modern subsidence rates, and (3) to discuss the advantages and limitations of using Persistent Scatterer Interferometry techniques over the Nile Delta.

ACKNOWLEDGMENTS

The work presented is supported by the National Science Foundation (NSF) grant #1103843 to Western Michigan University and data are provided by the European Space Agency (ESA) through the accepted Category-1 Proposal #12455. The Nevada Geodetic Laboratory is thanked for 24-hour GPS solutions and the Delft Institute for Earth-oriented Space Research is also thanked for orbital correction data.

I would like to thank Marco Defilippi and the whole SARMAP Team for the generous amount of time spent sifting through error messages and assisting with the SARscape software. Additional acknowledgements are granted to the Department of Geosciences at Western Michigan University, my colleagues in the Earth Science Remote Sensing (ESRS) Lab (specifically Dr. Mohamed Ahmed, Kyle Chouinard, Racha El Kadiri, and Mustafa Emil), and the members of my committee: Dr. Mohamed Sultan, Dr. William Sauck, Dr. Robert Gillespie (for the in-depth, handwritten edits), and Dr. Richard Becker.

Lastly, I would like to personally thank my family, specifically my mother, Suzanne Leblanc, my sister, Sarah Bouali, and my grandparents, Monique and Roland LeBlanc, whose support and jocularity has fueled my efforts and sculpted me into the person I have become today.

El Hachemi Yousef Bouali

TABLE OF CONTENTS

Table of Contents–Continued

Table of Contents–Continued

CHAPTER

Table of Contents–Continued

CHAPTER

LIST OF TABLES

LIST OF FIGURES

List of Figures–Continued

List of Figures–Continued

CHAPTER I

INTRODUCTION TO RADAR INTERFEROMETRY

Synthetic Aperture Radar and Interferometric Synthetic Aperture Radar

The uses of airborne- and satellite-based Synthetic Aperture Radar (SAR) techniques have become increasingly popular to simultaneously observe and measure spatial and/or temporal ground deformation over large regions of land. SAR is a coherent, side-looking radar system that simulates a large antenna by utilizing the flight path of a platform: the real antenna is located on the platform, which is attached to a moving airborne system or orbiting satellite, which transmits and receives radar signals. The synthetic aperture is a large, simulated antenna, which is created during the transmission and reception of radar signals to and from the airplane or satellite (Cutrona, 1990). Applying T as the length of time between the radar wave transmission and reception over a single target, then the length (L) of the synthetic aperture is equal to the product of T and the velocity (v) of the craft on which the real antenna is fixed:

$$L = Tv \qquad \text{(Eq. 1)}$$

The received radar waves are stored electronically as amplitude (A) and phase (θ), as a function of time. As the moving craft flies over a single target, when the line of sight (LOS) direction changes, with the LOS defined as the mean radar transmission/reception path, then a synthetic aperture is created over that target (Figure 1). One direct benefit of

creating a large synthetic aperture over a single target is that *L* is directly proportional to the resolution of the target, regardless of the altitude of the synthetic aperture, with a maximum possible resolution being approximately one-half the real antenna length (Wolff, 2008).

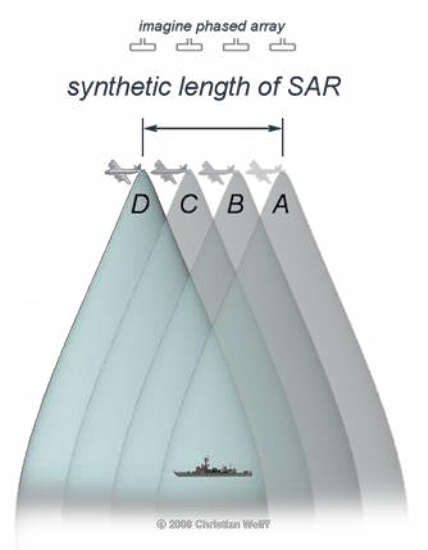

Figure 1: An Example of Synthetic Aperture Radar

Although the real antenna length is small (e.g., a point source antenna at the rear of a plane), the synthetic aperture length (L) of the SAR system depends on the number of different LOS directions (A, B, C, D) obtained for a single target. The synthetic aperture length can be orders of magnitude larger than the real antenna length (Wolff, 2008).

Radar data obtained from the ENVISAT spacecraft were used for this study. ENVISAT utilizes C Band radar waves with an approximate center frequency of 5.3 GHz and a wavelength of 5.6 cm. The Advanced Synthetic Aperture Radar (ASAR) active antenna on ENVISAT was 10 meters long (Karnevi et al., 1993). This allows for a spatial resolution of 25m x 25m. ENVISAT, launched in mid-2002, has a "revisit" period of 35 days. It was decommissioned in 2012 after a ten-year service-life (ESA, 2012a).

Steps for the general acquisition of radar amplitude and phase data over a regional swath are as follows:

Step 1: The satellite transmits a radar beam with a wave-propagation component in the range direction (perpendicular to the azimuth, or flight path, direction). This beam covers a 100-kilometer wide swath. Incoming radar beams have an incidence angle of 23° at the middle of the swath; incidence angles range from approximately 20° at the distal end of the swath and 26° at the proximal end of the swath (Figure 2). These radar waves are emitted as short pulses, or up-chirps, with a specified carrier frequency (5.331 GHz), sidebands, and bandwidth (Desnos et al., 2000). The benefit of using a digital chirp generation is the flexibility of altering the duration of the chirp pulse and the bandwidth for the different operational modes available on ENVISAT (Zink, 2002). Chirp pulses were preferred over other wave pulses, such as a square pulse, for the ability to maintain high resolution in the range direction with the usage of lower peak-power (Resti et al., 1999).

Step 2: These transmitted radar beams reflect and scatter off targets in the swath in a variety of ways. The type of radar wave backscatter observed is dependent on three main variables: (1) the radar wavelength, which for ENVISAT is 5.6 centimeter, (2) the physical size and geometry of scatterers within the target area, and (3) the moisture content of the targets (Dubois, 1995). SAR amplitude imagery (e.g., power (P) or intensity (I) images) is the fractional amount of radar wave return, and is proportional to the brightness of the image (Askne et al., 1997). Bright (or white) areas indicate regions of high backscatter. Dark (or black) areas indicate regions of low, or no, backscatter.

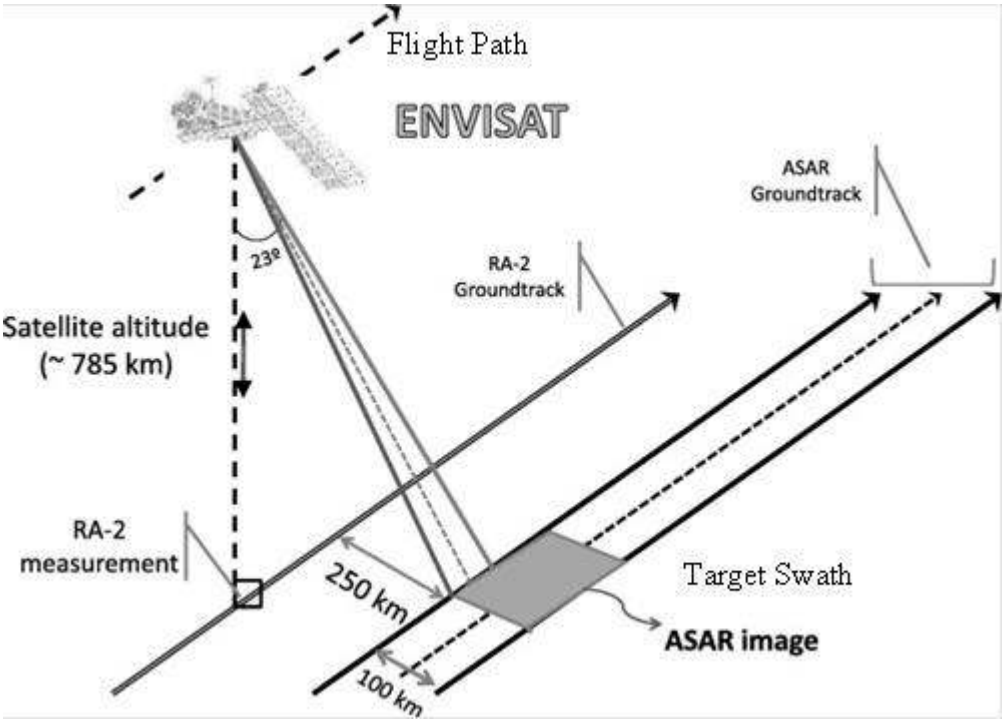

Figure 2: ENVISAT Flight Geometry

Geometry of the ENVISAT ASAR instrumentation with regards to the flight path (Medina et al., 2010). The flight path is the azimuth direction; the range direction is perpendicular to the azimuth direction. In ENVISAT ASAR Image Mode, the target swath is approximately 100 km x 100 km, with an incidence angle of 23° at the middle of the swath. ENVISAT was equipped with ten instruments, including a Radar Altimeter (RA-2), which helped determine the two-way travel delay of the radar return (ESA, 2002).

Because the wavelength of the transmitted radar waves is constant, the size/geometry and moisture content of the targets control the type of backscattering that will occur. There are five general types of radar wave backscattering: (1) specular reflection – this is a pure reflection of the radar waves on a mirror-like surface with no return (appears dark); (2) single bounce – the geometry of the target is oriented orthogonal to the LOS direction (appears bright); (3) double bounce – the geometry of the target is oriented such that

incoming radar waves reflect off surfaces perpendicular to each other prior to returning (appears bright); (4) surface scattering – rough, gravelly surfaces or short vegetation randomly scatter radar waves (appears variable); (5) volumetric scattering – forest canopies and other geometrically complex features cause the random scattering of radar waves in a three-dimensional sense (appears variable – Figure 3). Radar backscatter signatures can become incredibly complex within one pixel (625 square meters, ENVISAT) as combinations of the five backscattering mechanisms are possible. One example would be within a forest: there would be surface scattering (top of tree canopy), volumetric scattering (tree canopy), and double bounce (tree trunks and the ground) all combined at once.

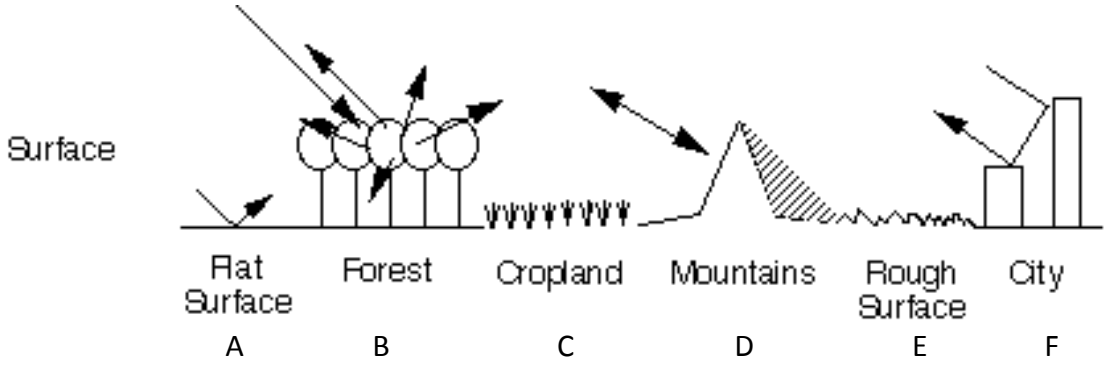

Figure 3: Types of Radar Backscatter

An illustration of the five types of backscatter mechanisms (Freeman & Wong, 1996). (A) The flat surface of a calm lake or a mirror will cause specular reflection. (B) Regions of tall vegetation (forests) will create volumetric scattering. (C) Cropland and other variable surfaces create surface scattering. (D) Geometric features that with faces perpendicular to the LOS direction, such as mountain faces lacking vegetation, will create single bounce reflections. (E) Rough surfaces create surface scattering, just like croplands. (F) Double bounce reflections occur in areas with flat, perpendicular reflectors, such as cities.

Step 3: Received radar waves, or echoes, are electronically recorded as a single-look complex (SLC) image, with a real, in-phase component (amplitude) and an imaginary, quadrature component (phase). Refer to Figure 4. The receiver can indirectly distinguish between various target distances based on radar wave arrival times.

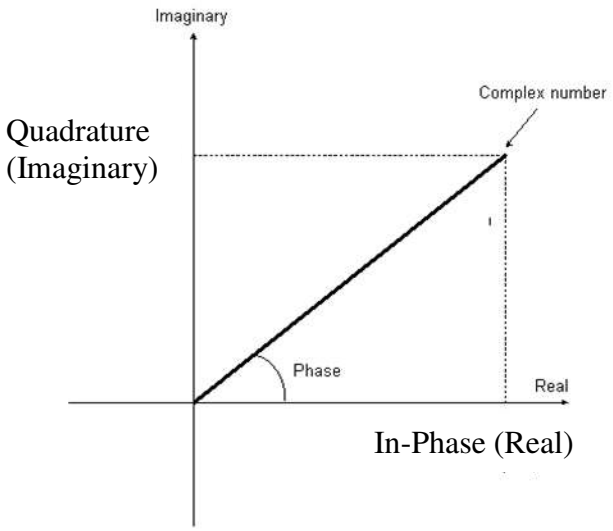

Figure 4: Three Components of a Complex Number: In-Phase, Quadrature, and Phase

Incoming radar wave information is detected and stored as a complex number. This requires the quantification of both magnitude (amplitude) and phase measurements. The digital representation of SAR data includes a real, in-phase (I) component and an imaginary, quadrature (Q) component. The phase is the angle measured between I and Q components (ESA, 2012b).

General SAR applications utilize only the amplitude portion of the received radar waves (Cutrona, 1990). Amplitude, or intensity ($I = A^2$), may be useful in analyzing types of features and/or backscatter mechanisms within a study area (Askne et al., 1997). One major difference between SAR and Interferometric SAR (InSAR) – which is the temporal study of SAR data – is that the prior only uses amplitude information from one acquisition while the latter uses both amplitude and phase information obtained over multiple acquisitions (Kampes et al., 2003).

The InSAR technique utilizes amplitude and phase information, which requires acquisition of at least two radar images, with identical look angles, over the same swath. ENVISAT, as previously noted, had a revisit period of 35 days, and, with the processing of multiple SLC radar images, allows for InSAR applications. The InSAR "technique-of-choice" depends on the number of acquisition scenes: two-pass InSAR requires two scenes (one master, or reference, and one slave acquisition), three-pass InSAR requires three scenes (one master and two slave acquisitions), et cetera (Massonnet et al., 1993; Massonnet et al., 1995). Stacked scenes, with multiple acquisitions over an extended period of time (e.g., many years), may be processed using the "Persistent Scatterers Interferometry" (PSI) technique, which is the method of choice and is described in greater detail below.

The phase (imaginary, quadrature) component is critical for the application of InSAR. A phase shift (ϕ) may be measured between a master scene and a slave scene. The phase shift may then be converted to solve for the change in distance (Δd) between the satellite and the target pixel over the timespan between the two acquisitions:

$$\Delta d = \frac{1}{2}\lambda\left(\frac{\phi}{2\pi}\right) \qquad \text{(Eq. 2)}$$

Phase is the complex component of the SLC record. It effectively measures the location, or the advancement, along the wavelength of the incoming radar waves when they reach the receiver (Figure 5). Therefore, a positive phase shift between two scenes acquired from the same orbital location at different times is proportional to an increase in distance between the satellite and the target pixel. One wavelength (λ) is equivalent to a 2π rotation in phase (an angle along a unit circle), thus the term $\lambda/2\pi$ accounts for the

incoming signal position along the wavelength (modulo 2π). Everything is multiplied by ½ to account for the two-way travel length (transmitter to target, target to receiver), with the distance from the transmitter to the target assumed to be equivalent to the distance from the target to the receiver. This means that *T* is short enough to assume a stationary position of the satellite during radar wave acquisition.

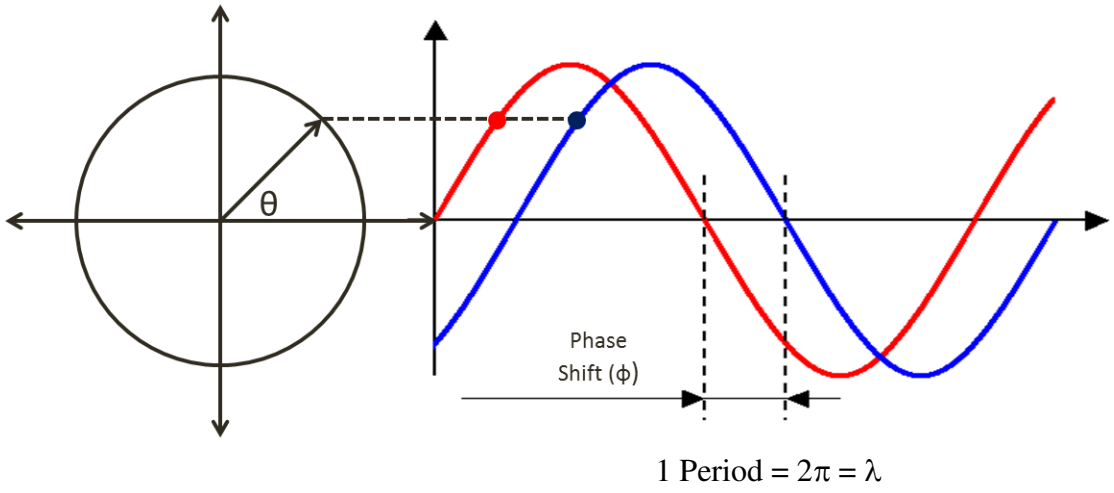

Figure 5: The Relationship Between Multiple Incoming Radar Waves: Wavelength, Phase, and Phase Shift

This is a visual representation of the phase (θ) and phase shift (ϕ) for two incoming radar waves. If the red radar wave was recorded during the master (reference) acquisition and the blue radar wave was recorded during the slave acquisition, then a positive phase shift (counterclockwise rotation) between the two acquisitions is observed. The change in the distance between the satellite and the target is directly proportional to the phase shift.

InSAR inherently fails if $\Delta d > (1/2\ \lambda)$. This would require a change in distance between the satellite and the target greater than 2.8 cm between chronological acquisitions. Note that InSAR fails with a change in distance of one-half the radar wavelength, which is a bit counterintuitive. This is a consequence of the two-way travel length: if the distance between the satellite and the target increases by 2.8 cm, the

transmitted radar waves must travel this distance and the reflected waves must also travel this distance, resulting in the total increased distance travelled by the radar waves to be 5.6 cm. The end result is a phase jump due to the modulo 2π nature of the phase: the phase shift will appear equal for any increased distance (between the satellite and the target) that is a multiple of λ (e.g., λ, 2λ, 3λ, …, $n\lambda$ where n is a positive integer). Therefore to avoid phase jumps one must either acquire a temporally dense set of scenes or avoid locations with relatively high LOS displacements.

Generation of SAR Products

InSAR processing requires the generation and usage of SAR products. The most convenient product to use from ENVISAT is the Level 1 SLC slant-range image, a product generated from Level 0 Advanced Synthetic Aperture Radar (ASAR) Image Mode data, which is obtainable through the online data ordering EOLI-SA Catalogue (Telespazio, 2012). Prior to InSAR processing, the Level 1 SLC images must be imported into the proper SLC format depending on the processing program used. Two processing programs were used for this study: (1) SARscape, a commercial software module of ENVI (Sarmap, 2013), and (2) StaMPS, an open-sourced software created at Stanford University (Hooper et al., 2009). Orbital corrections were then applied based on the ENVISAT precise orbit (EIGEN-CG03C) correction files from the Delft Institute for Earth-oriented Space Research (DEOS, 2008). Once the data have been imported and the orbital correction files applied, then the SAR products are ready for InSAR processing.

InSAR Processing Steps

Seven general InSAR processing steps must be performed in order to convert SLC slant-range image data to LOS ground displacements: (1) baseline estimation, (2) interferogram generation, (3) coherence and adaptive filtering, (4) phase unwrapping, (5) orbital refinement, (6) phase to height conversion and geocoding, and (7) phase to displacement conversion (Ferretti et al., 2000).

Step 1: Baseline Estimation

It is important to understand the exact location of the satellite along its orbital path each time it acquires radar data over the targeted swath. Although the satellite is never in the exact same three-dimensional location each time it passes over the target, knowledge of its actual location allows for the correction of errors that may arise from spatial deviations of actual locations from idealized locations. The baseline (B) is the distance, in three-dimensional space, between the satellite positions at different acquisitions; the perpendicular baseline ($B_{\perp}$) is the distance between the satellite location at the second acquisition and a point along the range direction of the satellite at the first acquisition (Figure 6). The baseline estimation is important because if the perpendicular baseline between a master scene and any slave scene is greater than the critical baseline (≈1,100 – 1,300 meters for ENVISAT), then there is a loss of coherence (see Step 3 for a further discussion of coherence) between the pair and, therefore, a loss of InSAR capabilities (ESA, 2008).

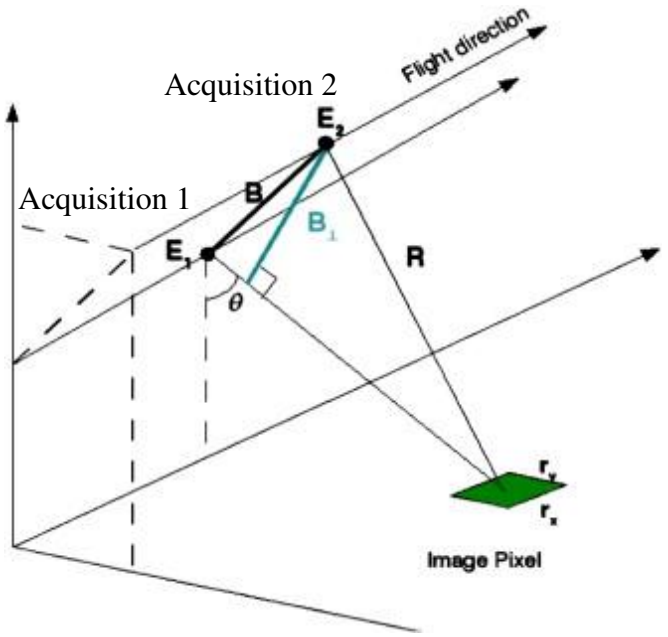

Figure 6: The Baseline Between Two Acquisitions

Schematic of two different acquisitions – Acquisition 1 (E_1) and Acquisition 2 (E_2) – of an orbiting InSAR satellite (Ahmed et al., 2011). The perpendicular baseline ($B_\perp$) is the distance between the satellite location at E_2 and the radar transmission/reception path that, when connected, creates a line perpendicular to the range direction I at E_1. $B_\perp$ is therefore greater than B.

Step 2: Interferogram Generation

This step incorporates five sub steps: image co-registration; complex interferogram generation; spectral shift and common Doppler filtering; interferogram generation, which includes topography; interferogram generation, excluding topography (Hooper et al., 2004).

Image Co-Registration

Co-registration is the process of spatially aligning multiple images geographically, so that pixels with identical coordinates (latitude, longitude) are accurately referenced to one another.

Complex Interferogram Generation

The complex interferogram is purely a mathematical product of the coherence file from the master scene and the complex conjugate of the coherence file from the slave scene (Ferretti et al., 2000). The result is a pattern of fringes (phase jumps) that contains all the information on the slant-range geometry of the study area, including topography (Ferretti et al., 2001). The complex interferogram is too difficult and too noisy to adequately unwrap the phase from (see Step 4: Phase Unwrapping), so further interferograms are created that eliminate topographic features.

Spectral Shift and Common Doppler Filtering

Radar waves are emitted in short pulses with a specified transmitted center frequency. Received incoming radar waves, however, exhibit pulses at various frequencies (usually due to a change in radar wave velocity between transmission and reception). The spectral shift and common Doppler filtering calculate and tune the filters to these changes in center frequency (Bamler & Hartl, 1998), in order to further process the data and create additional interferograms.

Interferogram Generation with Ellipsoid Flattening (Includes Topography)

An individual interferogram that uses a pre-defined ellipsoid as the datum is created in order to reduce the number of phase jumps (Ferretti et al., 2001). The assumption of general ellipsoidal geometry within the study area allows for a better interferogram approximation – one that is closer to the truth than the purely mathematical

complex interferogram – but still includes the local topography, which must be eliminated with the combined use of a Digital Elevation Model (DEM).

Interferogram Generation with Topographic Flattening via DEM (Excludes Topography)

The final interferogram is the third iteration and best approximation. The number of fringes is once again reduced and now excludes information regarding the local topography (Ferretti et al., 2001).

Step 3: Coherence and Adaptive Filtering

The coherence (γ) between two co-registered SAR images (master and slave scenes) is defined as the ratio between the summation of the coherent and incoherent radar data (Ferretti et al., 2000):

$$\gamma = \frac{|\sum s_1(x) \cdot s_2(x)^*|}{\sqrt{\sum |s_1(x)|^2 \cdot \sum |s_2(x)|^2}} \qquad \text{(Eq. 3)}$$

where $s_1(x)$ and $s_2(x)$ are the coherence files from the master and slave acquisitions, respectively, and $s_2(x)^*$ is the complex conjugate of the slave cohere file. The coherence ranges in value between 0 (incoherence or noise) and 1 (completely coherent signal), and is a function of systemic spatial decorrelation, natural scene decorrelation, and additive noise (Askne et al., 1999). Therefore, highly coherent pixels between two acquisitions will have minimal decorrelation (both systemic and natural) and minimal noise.

There are two major purposes of coherence data: (1) coherence assists in the quality assessment of measurements (e.g., phase) by the introduction of a coherence threshold, where all values below the threshold are neglected; (2) coherence, along with

the backscattering coefficient, allows for the extraction of information about objects within the target area (Askne et al., 1999; Ferretti et al., 2000).

The purpose of adaptive filtering is to eliminate the pixels that exhibit high noise (or low coherence) from the generated interferogram (Lopes et al., 1993). The coherence threshold is directly used in adaptive filtering, and is a user-defined variable.

Step 4: Phase Unwrapping

Phase unwrapping is the process that resolves the 2π ambiguity of the SLC phase data, translating the *wrapped phase* values to *absolute phase* values (Figure 7 – Goldstein et al., 1988). The incoming radar wave receiver, as stated previously, records the phase as a function of location along the wavelength. Therefore, the phase ranges in values from 0 to 2π. Once the phase reaches a value of 2π, it then automatically jumps and resets to a value of 0 (Lombardini, 1996). The purpose of phase unwrapping is to create an absolute, continuous phase signature by reconstructing the wrapped phase and by translating the phase jumps into a continuous phase ramp. The absolute phase is devoid of phase jumps and can be used to calculate the change in distance between the satellite and pixels within the target area (Hooper et al., 2004).

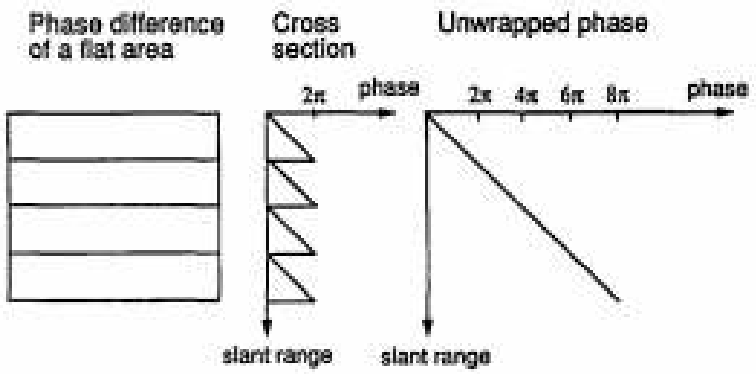

Figure 7: Phase Unwrapping: From Interferometric Fringes to Absolute Phase

Segmented rectangles illustrating fringe lines that indicate a phase difference in the absence of topographic relief (left). Each cycle of fringe lines (rectangles) represent a phase jump due to the modulo 2π nature of the phase (middle). The unwrapping of the phase into the absolute phase, which has no numerical range limitations, may be used to solve for the change in distance between the satellite and the target region (right – Lin et al., 1994).

Step 5: Orbital Refinement

An orbital refinement step is undertaken to correctly transform phase information into height values (Li et al., 2006). This procedure makes it possible to calculate the absolute phase and the phase offset between acquisitions, to refine the satellite orbit, and eventually to reduce the corresponding perpendicular baselines. Orbital refinement accounts for the shift in the azimuth and range directions, the spatial convergence of the orbits in both directions, and the absolute phase (Kohlhase et al., 2003). Put simply, this step is a three-dimensional spatial refinement of the satellite location (in space) at each acquisition point.

Step 6: Phase to Height Conversion and Geocoding

Absolute phase values for each acquisition, which have been calibrated and unwrapped, are then converted to height within each pixel where each value has a set of unique precision and height errors (Bayer et al., 1991). Height information is then geocoded into a user-specified map projection.

Step 7: Phase to Displacement Conversion

Complex interferograms contain information about topography, baseline, ground movement, atmospheric effects, and additive or systemic noises. Phase information obtained at each acquisition is influenced by each of these five variables; the equation below shows the additive nature of the influence of these variables on the total phase shift between two scenes:

$$\phi_{Int} = \phi_{topo} + \phi_{change} + \phi_{disp} + \phi_{atmo} + \phi_{noise} \qquad \text{(Eq. 4)}$$

where the total phase shift in the interferogram (ϕ_{Int}) is the sum of the phase shifts due to the topography (ϕ_{topo}), the change in satellite position (ϕ_{change}), any ground displacement relative to the satellite (ϕ_{disp}), all atmospheric effects (ϕ_{atmo}), and additive or systemic noise (ϕ_{noise}) (Hooper et al., 2004).

The purpose of the previous steps was to eliminate phase shifts due to extraneous factors. The generation of interferograms with topographic flattening using DEMs (step 2) eliminates the phase shift component due to local topography and the curvature of the earth. Adaptive filtering (step 3) eliminates the phase shift due to noise. The orbital refinement procedure (step 5) eliminates any phase shift due to the change in satellite

position. Two components remain: the phase shift due to ground displacements (the variable to be isolated) and the phase shift due to atmospheric effects (which must also be eliminated) (Zebker et al., 1997; Hooper et al., 2004).

Elimination of phase shifts due to an active atmosphere is the most difficult task when solving for ground displacement velocities. The atmosphere, specifically the troposphere, plays a large role in skewing radar wave returns. Dense, moist atmosphere affects radar waves two-fold: (1) particulates, clouds, and precipitation scatter radar waves, resulting in diminished amplitude returns, and (2) the velocity of radar waves decreases when travelling through material with a higher dielectric constant (DC) than air (DC air ≈ 1; DC water ≈ 80 – Telford et al., 1990; Zebker et al., 1997). Without proper atmospheric corrections, the resultant phase shift will yield an overestimation of ground displacement (if radar wave velocity decreases, a greater phase shift will occur, implying ground motion even if no ground motion actually occurred).

There are two methods of dealing with atmospheric effects.

The first method is to use additional weather datasets. The best option when using ENVISAT ASAR data is to utilize the co-acquired weather data from the Medium Resolution Imaging Spectrometer (MERIS), an instrument attached to the spacecraft itself (ESA, 2013).

The second method is to assume there is no significant gradient in atmospheric activity across the study area by segmenting the study area into geographically small sections. This second method was used in this study (the piecewise approach is described in Chapter 2).

Once the atmospheric component of the phase shift has been corrected for (and set to 0) along with all other unrequired component, only then can the remaining phase shift (due to ground motion) be successfully converted from phase shift units (radians) to LOS displacement units (millimeters).

The number of scene acquisitions used in an interferometric stack directly relates to the geodynamic phenomena being studied. Single events, such as earthquakes, can be resolved with a two-pass InSAR analysis (master image: pre-quake and a slave image: post-quake) will suffice. Slow, long-term events, such as ground subsidence or landslide creep, requires a stack of 20+ scenes during multiple years, to observe small ground motions and be able to successfully measured them on millimeter scales (Ferretti et al., 2000; Ferretti et al., 2001; Hooper et al., 2004). PSI is the InSAR "technique-of-choice" for this purpose in this study.

Persistent Scatterer Interferometry

The theory behind PSI is similar to that of InSAR. PSI is an interferometric stacking technique that is capable of measuring small ground deformations throughout long periods of time. The PSI processing procedure incorporates all of the InSAR processing steps, but the output differs due to the fundamental purpose of PSI: the technique searches the study area for consistently coherent features (on a sub-pixel scale) throughout the stack. Consistent coherence requires a surface feature be relatively stable (no spatial or temporal decorrelation) and that it must also be combined with a backscattering mechanism conducive to high-amplitude radar returns to the satellite

receiver (e.g., single or double bounce) (Ferretti et al., 2000). Surface features that fulfill these requirements are usually man-made structures, such as roads, bridges, buildings, and dams. But, they may also be natural features, such as rock outcrops or cliff faces which lack vegetation. Features that consistently yield high radar returns are known as Persistent Scatterers (PS) and are the only points with ground displacement information in the PSI output – all other non-PS pixels, those that do not qualify, are discarded and provide no output information.

The smaller the ground motion to be measured, the longer the period of time needed to adequately observe and measure the deformation (Hooper et al., 2004; Bürgmann et al., 2006). This introduces a problem regarding coherence. PSI requires stable, high-coherence PS over a relatively long timespan, but, coherence decreases throughout time. Because coherence is a function of spatial/temporal decorrelation and noise, the greater the time between two acquisitions, the lower the coherence between them. Conversely, the greater the time between two acquisitions, then the greater the likelihood of geometric differences between the scenes. Vegetation will naturally have low coherence between two acquisitions. For example, if the first acquisition occurred on a windy day, and the second acquisition occurred on a calm day, then radar returns will be completely different. Vegetation, in this case, displays low coherence due to the large number of backscattering mechanisms possible and the ease of spatial decorrelation (e.g., vegetation growth greater than 2.8 cm between acquisitions).

Similar to any other radar interferometric technique, PSI has its advantages and limitations compared to other InSAR techniques. Advantages of using PSI include: (1)

the ability to cover urban areas with high (sub-pixel) spatial resolution with a potential PS density on the order of 1,000s PS/square kilometer, (2) the ability to detect mm/year-scale ground velocities, and (3) the vast historical archive of ESA-funded, compatible SLC radar images, an almost continuous span from 1992 through 2011 between the ERS-1, ERS-2, and ENVISAT spacecraft (Crosetto et al., 2010). Limiting factors, on the other hand, include: (1) the inability to measure relatively quick ground deformations (greater than 2.8 cm between acquisitions), (2) variable spatial sampling (urban areas: 1,000s PS/square kilometer; rural areas: less than 50 PS/square kilometer), (3) PS locations are unknown prior to processing, and (4) all ground displacement measurements are made in the LOS direction (Crosetto et al., 2010 – this is a problem for all radar interferometric applications using satellite-based data recorded at an incidence angle, not just PSI; true vertical ground motion may be solved for with the combined use of descending and ascending paths over a target region).

Many of these limiting factors are a non-issue for the purpose of this study. Subsidence rates across the Nile Delta, and other wave-dominated deltas around the world, exhibit ground motions of less than 1.5 cm/year and do not reach the failure velocity of 2.8 cm per acquisition. Any subsidence acceleration should occur over a relatively long period of time (multiple acquisitions). This assumption can be made because the overwhelming factor of subsidence in the delta is natural sediment compaction and subsidence rates should change gradually, and would not cause a breach of the failure velocity limitation. The high variation in spatial sampling allows for a detailed subsidence analysis of urban areas within the delta, but ignores vegetated

regions. Many small villages and cities appear as ‘urban islands’ in the dense sea of vegetation surrounding them, so the expected PSI output will show this PS density skew. Unfortunately, there is no way to avoid the uncertainty in knowing exact PS locations within urban areas prior to processing.

PSI has been chosen as the best possible radar interferometric technique to measure subsidence rates across the Nile Delta in Egypt. Customizations have been made to effectively use this procedure and to minimize the difficulties that arise when using PSI over such a large area.

CHAPTER II

DATASET AND PROCESSING

Introduction

This chapter is separated into two main sections. The first section, "Dataset," discusses the parameters of the ENVISAT scenes obtained and the criteria that were used when initially choosing the data. The second section, "Procedure and Processing Steps," gives a detailed account of all the processing operations performed on the data, from the pre-processing through the post-processing.

Dataset

There are a total of 116 ENVISAT scenes from four descending orbital tracks (from west to east: 479, 207, 436, and 164) that were obtained from the European Space Agency (ESA) as Level 1 single-look complex (SLC) slant-range images. The scenes range in acquisition date from 2003 to 2010. Orbital tracks cover a substantial area of the Nile Delta – latitude: 30.70°N-31.61°N; longitude: 29.70°E-32.95°E, with regions of overlap between adjacent orbital tracks (Figure 8). A more detailed discussion of the study area (geology, atmospheric activity, and anthropogenic impacts on the delta) is the topic of Chapter 3.

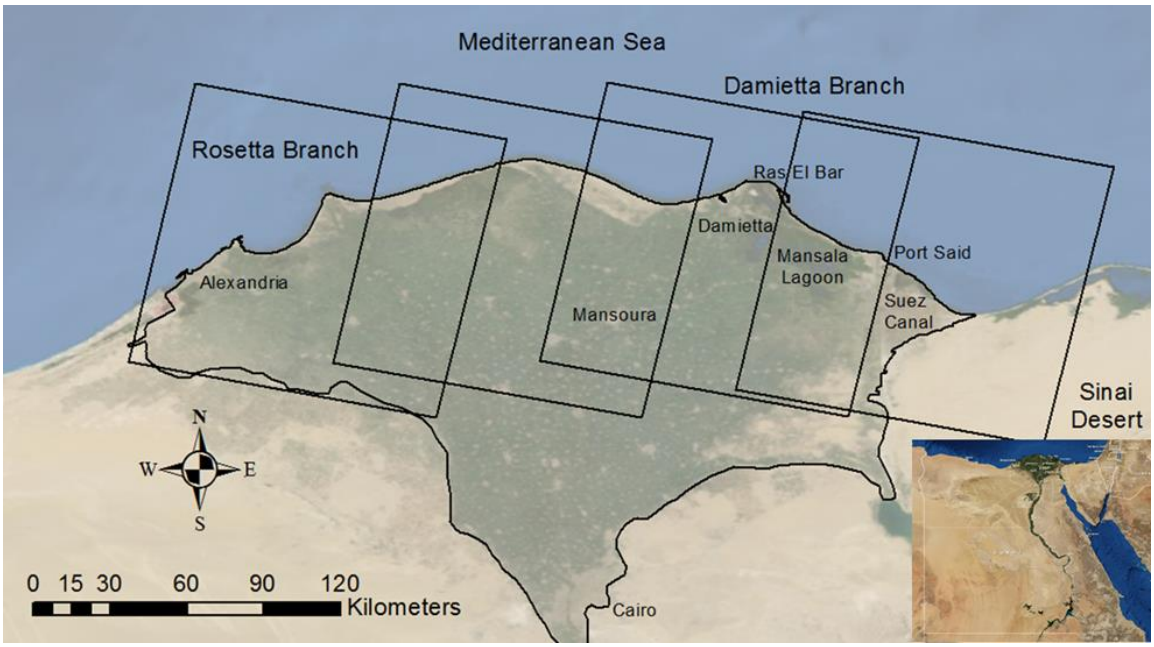

Figure 8: Orbital Tracks

The four descending scenes within respective orbital tracks (west to east: 479, 207, 436, and 164) across the northern Nile Delta of Egypt, as observed by the Moderate Resolution Imaging Spectroradiometer (MODIS) instrument on the ENVISAT satellite (ESRI, 1999).

Three criteria were established for choosing the master scene for each stack of ENVISAT SLC images in each orbital track: (1) the spatial baselines between the master and slave scenes must be less than 1,300 meters (critical baseline), (2) the temporal baselines must be as close to zero as possible (in other words, the master scene must be located near the temporal median of the stack), and (3) the Doppler centroid differences, where the Doppler centroid difference is the frequency difference between the master and slave mean frequencies, must be as close to zero as possible. The complete list of ENVISAT scenes, with all spatial baselines and Doppler centroid differences relative to the master scene, may be found in chronological order in Tables 1-4.

Table 1: 32 ENVISAT scenes processed from orbital track 479.
The master scene (bold) is 2006-04-16.

Acquisition Date	Spatial Baseline (m)	Doppler Centroid Difference (Hz)
2003-08-10	-614.64	23.6667
2003-12-28	849.847	12.0378
2004-02-01	758.629	9.44584
2004-04-11	878.553	28.4031
2004-07-25	379.048	9.43969
2004-10-03	35.9972	12.8026
2004-12-12	-135.828	20.8857
2005-01-16	-155.636	20.3261
2005-03-27	-639.623	-17.4144
2005-05-01	755.024	-5.68982
2005-06-05	-321.208	-2.03962
2005-08-14	-154.115	-8.26303
2005-09-18	183.88	-0.955876
2005-11-27	-78.991	24.0542
2006-04-16	**0**	**0**
2006-07-30	1062.59	2.76325
2006-09-03	515.686	-5.17487
2006-10-08	-442.077	24.6875
2007-02-25	182.625	4.1875
2007-12-02	362.767	22.9757
2008-03-16	-74.2943	25.6475
2008-04-20	347.355	6.63682
2008-05-25	63.7387	35.9046
2008-10-12	35.4951	-32.3367
2009-03-01	329.047	29.343
2009-04-05	558.588	-10.839
2009-07-19	178.552	-15.8744
2009-08-23	125.898	-24.4172
2009-12-06	271.06	0.101476
2010-01-10	-29.7653	26.3208
2010-03-21	210.976	0.987986
2010-04-25	310.607	8.91251

Table 2: 29 ENVISAT scenes processed from orbital track 207.
The master scene (bold) is 2008-07-15.

Acquisition Date	**Spatial Baseline (m)**	**Doppler Centroid Difference (Hz)**
2004-02-17	-708.763	-0.840353
2004-07-06	-580.451	11.7574
2004-08-10	-415.879	1.88883
2004-10-19	583.919	-19.6671
2004-12-28	-104.264	-15.1988
2005-03-08	-64.2455	-15.2008
2005-05-17	53.8612	-14.425
2005-07-26	244.509	-20.0011
2005-11-08	498.531	-20.306
2006-01-17	-1088.77	-15.2154
2006-02-21	-456.777	-9.28647
2006-06-06	-717.079	-12.9959
2006-07-11	803.539	-2.28969
2006-10-24	-576.093	-2.50563
2007-01-02	164.016	-9.72231
2007-02-06	-329.98	-0.728012
2007-03-13	157.831	-5.69176
2007-11-13	43.3676	-3.91855
2008-04-01	40.5777	15.4384
2008-07-15	**0**	**0**
2008-12-02	-290.114	11.8015
2009-02-10	-292.009	7.67295
2009-04-21	-278.089	-13.8832
2009-08-04	-274.171	-14.4271
2009-09-08	119.97	-17.8873
2009-10-13	-396.215	-12.9711
2009-12-22	-304.742	-8.50606
2010-03-02	-334.257	-5.32426
2010-05-11	27.5674	-12.3815

Table 3: 31 ENVISAT scenes processed from orbital track 436.
The master scene (bold) is 2007-03-29.

Acquisition Date	Spatial Baseline (m)	Doppler Centroid Difference (Hz)
2004-03-04	-556.327	30.1142
2004-04-08	384.967	22.9503
2004-06-17	-249.983	11.0567
2004-08-26	-391.265	27.4306
2004-09-30	-661.532	31.6481
2004-12-09	-422.532	23.6488
2005-01-13	-729.381	-1.75272
2005-03-24	-1007.19	10.6616
2005-06-02	-616.853	-8.51868
2005-07-07	484.016	-4.05451
2005-08-11	-749.276	20.0246
2005-09-15	-178.665	2.53875
2005-11-24	-228.329	-5.5361
2005-12-29	-375.885	-1.42167
2006-04-13	-598.871	-3.24943
2006-06-22	34.8683	5.07864
2006-07-27	640.312	14.9744
2006-10-05	-916.617	0.530329
2007-02-22	-190.14	0.69283
2007-03-29	**0**	**0**
2007-11-29	-224.25	2.66907
2008-03-13	-471.09	14.4557
2008-04-17	-195.578	11.7319
2008-09-04	-200.196	17.8794
2009-02-26	-168.678	24.5795
2009-04-02	178.175	4.80872
2009-07-16	-282.388	2.55648
2009-08-20	-367.933	4.01429
2009-09-24	191.588	26.0005
2010-01-07	-378.023	-1.67244
2010-05-27	-443.24	-10.8508

Table 4: 24 ENVISAT scenes processed from orbital track 164.
The master scene (bold) is 2008-07-12.

Acquisition Date	**Spatial Baseline (m)**	**Doppler Centroid Difference (Hz)**
2004-11-20	-241.613	-17.6682
2004-12-25	-247.797	-15.2197
2005-03-05	-154.890	-14.9459
2005-04-09	-216.820	7.37453
2005-06-18	37.1015	-14.3469
2005-07-23	370.864	-11.2927
2005-08-27	344.795	-2.18583
2005-11-05	462.344	2.40533
2006-02-18	-451.968	21.1144
2006-03-25	-59.2598	-16.1295
2006-06-03	-928.069	-15.9736
2006-07-08	753.479	7.41577
2006-12-30	137.779	-12.159
2007-03-10	200.534	-16.9682
2008-03-29	55.7329	-25.1536
2008-07-12	**0**	**0**
2009-01-03	-98.0488	-0.386305
2009-02-07	-463.140	16.3171
2009-03-14	290.607	14.0053
2009-05-23	-181.479	11.7951
2009-11-14	-22.9553	-28.9741
2009-12-19	-399.603	-9.87779
2010-02-27	-479.606	-16.13
2010-05-08	-17.5809	-7.07716

The spatial baseline and the Doppler centroid difference were the two most important variables monitored when obtaining scenes from the ESA.

The spatial baseline is the distance measurement between the satellite locations at different acquisitions (Ferretti et al., 2001). All spatial baselines, in this case, are relative to the master scene. So, the baseline is the distance between the satellite location at the master acquisition point (e.g., 2006-04-16 for the track 479 stack) and the respective slave acquisition point. Positive or negative spatial baselines indicate the relative positioning of the satellite at the slave acquisition (i.e., positive: "in front of" or negative: "behind" the satellite location at the master acquisition).

The Doppler centroid difference is important because it distinguishes the SAR azimuth spectrum location (or the mean frequency of the image mode azimuth bandwidth – ESA, 2008). The bandwidth of the transmitted radar waves from ENVISAT is approximately 1,378 Hz and a Doppler centroid difference greater than the bandwidth results in total decorrelation between scenes because there is no frequency overlap in the azimuth bandwidth (Figure 9). Therefore, the smaller the Doppler centroid difference, the greater the overlap in azimuth bandwidth between two acquisitions, and the better the Interferometric Synthetic Aperture Radar (InSAR) coherence (ESA, 2008).

All ground motions are in the line-of-sight (LOS) direction because only descending ENVISAT scenes were obtained. The incidence angle, denoted as θ, is the angle between the LOS and local vertical varies between 18.50° (east) and 26.75° (west) within each orbital track, and the range direction points towards the west. Lack of ascending scene acquisitions over the Nile Delta (28 ENVISAT scenes between 2004 and

2010 over five orbital tracks) resulted in temporal resolution too low to adequately process and obtain reliable ground motion measurements using Persistent Scatterer Interferometry (PSI). Therefore, true vertical ground displacement was immeasurable via radar interferometry.

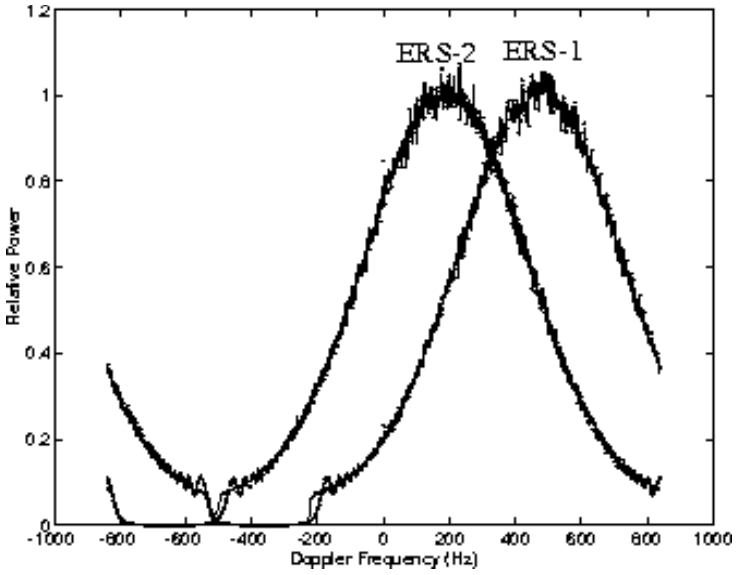

Figure 9: Doppler Centroid Frequencies

Example of Doppler centroid frequencies between acquisitions made by ERS-1 and ERS-2 while on a tandem mission (Barmettler et al., 1996). Because ENVISAT data is compatible with ERS-1 and ERS-2 data, the effects of the Doppler centroid differences are similar. The two acquisitions shown above share a common bandwidth (overlap), between -200 to 600 Hz (range = 800 Hz), because the relative power of the ERS-1 satellite is effectively 0 below -200 Hz. Therefore, this pair of scenes shares approximately 58% of the available 1,378 Hz of potential common bandwidth. The Doppler centroid is the Doppler frequency at which the greatest relative power (normalized to one) is recorded. The Doppler centroid for the ERS-1 acquisition is approximately 550 Hz and for the ERS-2 is approximately 200 Hz. The Doppler centroid difference for this pair is -350 Hz (assuming the ERS-1 acquisition is the master scene).

Procedure and Processing Steps

Many steps are required to completely process four separate stacks of ENVISAT scenes across four descending orbital tracks. PSI processing may be broken up into three categories: (1) the pre-processing procedure (uploading, formatting, and preparation of the ENVISAT images), (2) the processing steps (the actual steps taken to process SLC radar images to obtain interferograms, and ultimately, a PS ground velocity map of each cropped region), and (3) post-processing procedure (conversion of the relative ground velocities obtained via radar interferometry to absolute ground velocities from the known GPS station).

Pre-Processing Procedure

The 116 ENVISAT scenes were obtained from the ESA through the acceptance of project proposal #12455 and were ordered and downloaded as Level 1 SLC slant-range images. These products were generated from Level 0 Advanced Synthetic Aperture Radar (ASAR) Image Mode data (Telespazio, 2012). The Level 1 SLC images were then imported into the proper SLC format, either compatible with SARscape (Sarmap, 2013) or with the open-source Stanford Method for Persistent Scatterers (StaMPS) program (Hooper et al., 2009a). Orbital corrections were then applied based on ENVISAT precise orbit (EIGEN-CG03C orbits) correction files from the Delft Institute for Earth-oriented Space Research (DEOS – Delft Institute, 2008).

Ultimately, a multi-baseline analysis was performed for each scene-stack per orbital track. The purpose of the multi-baseline analysis was to determine the optimal

combination of scenes to include in the PSI, as described above. Resultant stacks are shown in Tables 1-4.

Each ENVISAT scene covers an area of approximately 10,500 square kilometers. Processing an entire scene would be unrealistic due to the amount of time, computer storage/memory required, and due to the active atmosphere effect over the Nile Delta (lateral atmospheric gradients greatly affect radar interferometric outputs, as discussed in Chapter 4). Therefore, scenes were cropped to an area that ranged from 100 to 1,600 square kilometers (depending on geographic location within the Nile Delta). Large cities (areas greater than 4 square kilometers) were first cropped and processed individually. Because large cities are regions of high coherence, they were later reprocessed as part of a larger cropped region, allowing for better co-registration within the stack of scenes. Complications in co-registration arose when areas with a lack of large cities, and an abundance of vegetation, were processed; these regions were usually avoided.

Processing Steps

PSI processing of the cropped scenes was performed using both the SARscape software and the StaMPS program. There were processing strengths and weaknesses associated with each of the two programs, which were observed over the processing period. SARscape yields optimal results in large urban areas. PS density is much greater than using StaMPS. SARscape was able to detect multiple PS points per pixel in highly coherent cities. However, SARscape was unable to detect PS points in small cities (area less than 2-3 square kilometers) and usually left large swaths of the Nile Delta empty or

noisy. StaMPS, on the other hand, performed well over the regions SARscape failed in, but, unlike SARscape, StaMPS yielded much lower PS densities in large urban cities.

One region of the Nile Delta was chosen and processed using both SARscape and StaMPS to make sure that both gave similar results, specifically concerning LOS ground velocity. Once this was confidently determined, the two programs were employed to analyze specific target regions: (1) the focus of the SARscape processing was along the Mediterranean coast and across the Damietta River Branch, where a majority of the large cities are located, and (2) the focus of StaMPS processing was along the southern portions and mid-latitudes of the Nile Delta, where many small villages and towns are sporadically spaced and surrounded by dense agricultural land.

Technical Notes of PSI Processing Steps

The following two sub-sections explain the technical processing procedure used in SARscape and in StaMPS. The general processing steps for PSI are similar to the InSAR processing steps described in Chapter 2. These sub-sections describe technical notes specific to the PSI technique and to each program.

Processing using SARscape

The InSAR PSI processing was executed in SARscape using the *Interferometry – Low Coherence* default values. This default setting was chosen because of the great areal extent of vegetation (low/variable coherence zones) across the Nile Delta.

PSI processing begins with the co-registration of all slave scenes in the interferometric stack to the master reference scene. Co-registration accounts for any

translational, rotational, or scaling differences between the master and slave scenes in order to accurately superimpose the pixels of each scene in slant-range geometry. It requires a Digital Elevation Model (DEM) to co-register the stack of scenes. The co-registration step is automated as presented in the following procedure: (1) Non-parametric shift estimates are computed based on the input DEM and orbital data, (2) windows are placed on the master image (40 windows in both range and azimuth directions), (3) cross-correlations function for each of the windows are computed (the maximum of each function indicates the proper shift), (4) the residual parametric shift is calculated, and (5) a further fine-shift is performed by created "mini-interferograms" on smaller windows (30 windows in the range direction and 50 windows in the azimuth direction).

Interferograms are then created between the master scene and each slave scene. They are flattened to the DEM and projected onto the master scene in slant-range geometry. During the interferogram generation step, the scenes are first multilooked (1 range look, 5 azimuth looks) to reduce speckle in the azimuth direction. Next a spectral shift filter is applied between the master and each slave scene. The spectral shift filter removes non-overlapping portions of the frequency bandwidth, and is useful during cases when the spatial baseline does not equal zero (almost always). A Doppler filter is also available for pairs of master and slave scenes with a large Doppler centroid difference (on the order of 100s of Hz). However, the largest Doppler centroid difference calculated for any pair was 35.9046 Hz, so this filter was not applied. The next step is the actual

generation of interferograms between each master-slave pair, concluding with the interferogram generation with topographic flattening, employing the DEM.

Goldstein Interferogram Filtering (GIF) was then applied to the interferograms. The purpose of GIF is to reduce noise introduced by decorrelation (spatial and temporal) and to improve the fringe signal-to-noise ratio (SNR). The strength (α – the exponent of the power function filtering spectrum of the interferogram data) of the GIF is coherence-dependent: weak filtering ($\alpha = 0.5$) is applied to high coherence ($\gamma = 1$) regions while stronger filtering ($\alpha = 3.5$) is applied to low coherence ($\gamma = 0$) regions. Also, in this case, an additional low pass filter (5%) was applied to remove high frequency phase noise.

The interferograms next undergo phase unwrapping. This step is performed with a minimum decomposition level of 1, which multilooks and undersamples the interferogram data. The interferogram is first unwrapped at a lower resolution (which aids in avoidance of unwrapping errors and reduces the processing time required) and then is reconstructed back to the original resolution. Unwrapping errors may occur in regions of low coherence, especially if these regions are randomly distributed across the interferogram. A decomposition level of 1 is equivalent to an iteration of interferogram resolution decomposition that corresponds to an undersampling factor of 3.

The last major processing step is to estimate the atmospheric pattern throughout the processed area. This is a crucial estimation because an active atmosphere (usually the troposphere, composed of precipitation, humidity, dust, and other particulates), may lower the velocity of and scatter radar waves via a positive atmospheric phase shift. The scene area is segmented into 25 square kilometer regions. Two filters are then applied:

(1) a low-pass spatial filter (1,200 meters) estimates and eliminates atmospheric spatial variations which are assumed to have a low lateral gradient; (2) a high-pass temporal filter (365 days) estimates atmospheric changes over time (365 days – usually includes between 3 to 5 acquisitions in the temporal window).

Typical PS densities within urban areas are 200 PS/square kilometer or greater. They are much lower in rural areas (<50 PS/square kilometer). The PS density is important because it directly relates to the computed mean velocity error, which is estimated and inversely proportional to the PS density. Finally, a product coherence threshold (the minimum acceptable coherence per pixel) is applied to the PS output data. Only PS points with coherence greater than the product coherence threshold (set at 0.75) will appear in the output ground velocity file. All other pixels will not contain any ground velocity information.

Processing using StaMPs

InSAR PSI processing was performed using all default values with the exception of the co-registration window number and size, which had to be changed for the program to properly co-register the slave scenes to the master scene in regions of dense vegetation. Complete discussion of the interferogram generation may be found in the *Delft Object-oriented Radar Interferometric Software (DORIS) User's manual and technical documentation (v4.02)* reference file (DEOS, 2008), and a discussion of PSI processing steps may be found in *StaMPS/MTI Manual (v3.1)* (Hooper, 2009b).

There are a minimum of 18 pre-PSI steps required to properly process SLC image radar data and obtain interferograms between the master scene and each slave scene. A brief explanation of each step, and relevant input values, is described below:

1. M_READFILES: The SLC image mode format of the master scene and information regarding the acquisition satellite are required as inputs.
2. M_CROP: The master SLC image is cropped to a user-defined study area.
3. S_READFILES: The SLC image mode format of the slave scene and information regarding the acquisition satellite are required as inputs.
4. S_CROP: The slave SLC image is cropped to a user-defined study area.
5. COARSEORB: The slave SLC image is co-registered to the master SLC image based on their respective orbital data. This is a coarse co-registration step with an accuracy of approximately 30 pixels.
6. COARSECORR: This is a medium co-registration step, where the offset between the master and slave intensity images is computed in the spectral domain. The accuracy of this step is approximately 1 pixel. The offset between the two images is the mode of the calculated offsets over the cropped area. If medium co-registration was not possible with the default settings, the number of windows and/or the window sizes were doubled until proper medium co-registration was obtained.
7. FINE: This is the fine co-registration step, with an expected accuracy on the sub-pixel scale. The offset is once again computed in the spectral domain. If fine co-registration was not possible with the default settings, the number of windows

and/or the window sizes were increased until proper fine co-registration was obtained.

8. COREGPM: The final co-registration step, where the estimated offsets are modeled using a first-degree two-dimensional polynomial until a certain number of iterations is accomplished or until the least squares adjustment is accepted for all points. Any pixel with a coherence below the product coherence threshold (γ = 0.4) is automatically set to 0 and excluded from the least squares adjustment estimation.
9. RESAMPLE: The slave image is then resampled based on the master image grid. This step reconstructs the original slave image signal with a 4-point cubic convolution kernel interpolation method. The cubic convolution kernel is a continuous and differentiable piecewise third-degree polynomial (Meijering & Unser, 2003) used to smooth out gaps introduced by the product coherence threshold of the previous step.
10. INTERFERO: The complex interferogram is created.
11. COMPREFPHA: This step calculates the phase due to the curvature of the earth by using a reference ellipsoid (e.g., WGS84).
12. SUBTRREFPHA: This step subtracts the phase due to the curvature of the earth from the complex interferogram. The result is an interferogram dominated by topographic fringes.
13. COMPREFDEM: This step calculates the phase due to local topography and requires the input of a DEM.

14. SUBTRREFDEM: This step subtracts the phase due to local topography from the interferogram created in step 12, resulting in an interferogram containing fringes due to ground deformation, atmospheric delay, residuals of topography, and random error.
15. COHERENCE: A complex coherence image is computed from the complex interferogram (step 10). A coherence map is also generated.
16. UNWRAP: The DORIS software does not perform the phase unwrapping step. Instead, additional public domain software – Snaphu (Hooper, 2009b) – is required. An unwrapped interferogram is the output of this step.
17. SLANT2H: The exact position and height of each pixel is calculated using the Ambiguity Method. The Ambiguity Method uses simple trigonometry to convert the slant-range geometry into height geometry (Figure 10) and essentially follows these steps: (1) the perpendicular baseline ($B_\perp$) and parallel baseline ($B_\parallel$) are calculated, (2) the incidence angle (θ) to each pixel is calculated, (3) since both the altitude of the satellite above the reference ellipsoid (H) and the distance between the satellite and each pixel (R_1) are known, the height of each pixel above the reference ellipsoid (h) may be calculated using the following geometric equation:

$$h = H - R_1 \cos\theta \qquad \text{(Eq. 5)}$$

The absolute phase (φ), an indirect measure of change in distance between the satellite and the target, is also converted to height with the following equation:

$$h = -\frac{\lambda}{4\pi}\frac{R_1 \sin\theta}{B_h \cos\theta + B_v \sin\theta} \qquad \text{(Eq. 6)}$$

where λ is the radar wavelength (5.6 centimeters) and B_h and B_v are the horizontal and vertical components of the baseline, respectively.

18. GEOCODE: This step converts height geometry to a pre-defined geocoded coordinate system (e.g., UTM).

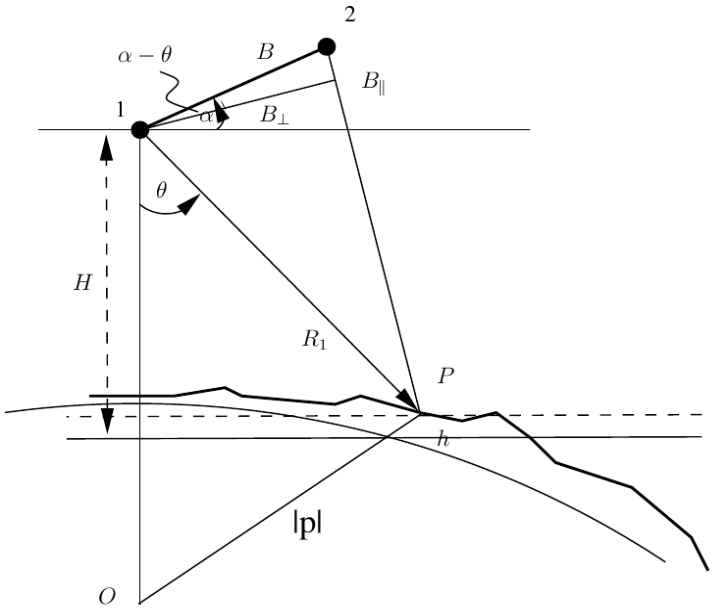

Figure 10: Geometry of Two Satellite Acquisitions (1 and 2)
over the Same Target Pixel (P)

The variables relating to the slant-range to height geometric conversion equations are illustrated in this figure (DEOS, 2008).

StaMPS is able to bulk-process the previous 18 steps (from DORIS), allowing for the set-up of the PSI stacking analysis. The PSI processing itself requires 7 additional steps:

1. Load Data: Uses the interferogram products generated in DORIS between the master and slave scenes.

2. Estimate Phase Noise: This step estimates the phase noise value for every pixel in each interferogram using a Combined Low-pass and Adaptive Phase (CLAP) filter (Hooper et al., 2007).
3. PS Selection: Pixels are selected as potential PS candidates based on coherence and noise information. The default value of 20% is set as the maximum percentage of random phase pixels allowed.
4. PS Weeding: Pixels chosen in the PS Selection (step 3) are included or excluded based on the amplitude (or intensity) of each pixel compared to its neighboring pixels. A pixel is excluded (or weeded out) if the standard deviation of the phase noise for all its neighboring pixels is greater than one standard deviation. A smoothing parameter is introduced, where the time series for each pixel is smoothed using a Gaussian window (default value = 8) with a standard deviation of one; the noise is assumed to be the difference between the original phase and the smoothed phase.
5. Phase Correction: This is a spatial correction step for the wrapped phase of the accepted PS pixels.
6. Phase Unwrapping: Utilizes a 3D phase unwrapping method (Hooper & Zebker, 2007) and attempts to estimate orbital and atmospheric errors.
7. Estimate Spatially-Correlated Look Angle Error: Errors due to DEM are calculated. It is recommended to redo steps 6 and 7 in order to subtract the modeled effects of orbital, atmospheric, and DEM errors to the interferograms.

The PS data can then be plotted in a geocoded coordinate system.

Post-Processing Procedure

One known GPS station, located in Alexandria, Egypt (latitude: 31.197066°N, longitude: 29.910991°E) was used as the reference location. This is a known stationary point (Figure 11 – NGL, 2013).

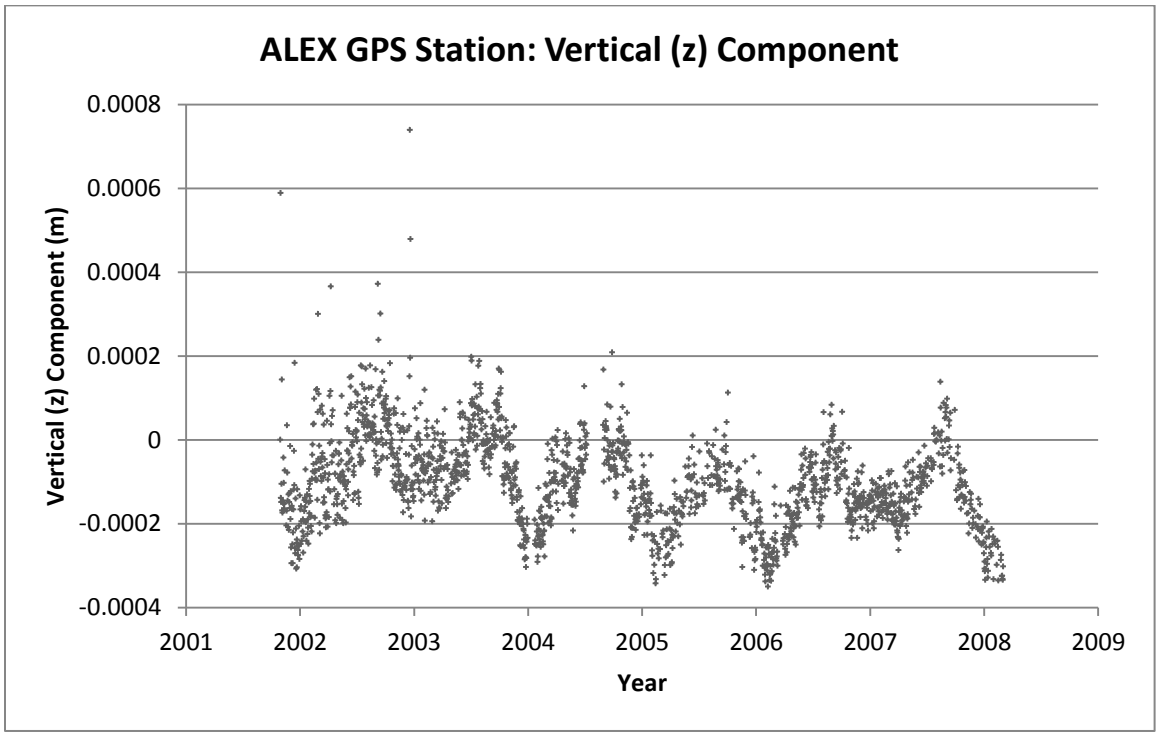

Figure 11: Vertical Ground Motion at the ALEX GPS Station, 2002-2008
The daily (24 hour solutions) GPS station height (meters) from October 10, 2001 to March 5, 2008. The average ground velocity is 0.05 ± 0.28 mm/year – basically stable. This GPS station is located at latitude: 31.197066°N, longitude: 29.910991°E in the city of Alexandria, Egypt (data provided by NGL, 2013).

Because the study area, or even each orbital track, was too large to process at one time, the study area was cropped into regions ranging from 100 to 1,600 square kilometers. The initial cropped region (i.e., Area 1 – refer to Figure 12) included the known GPS station

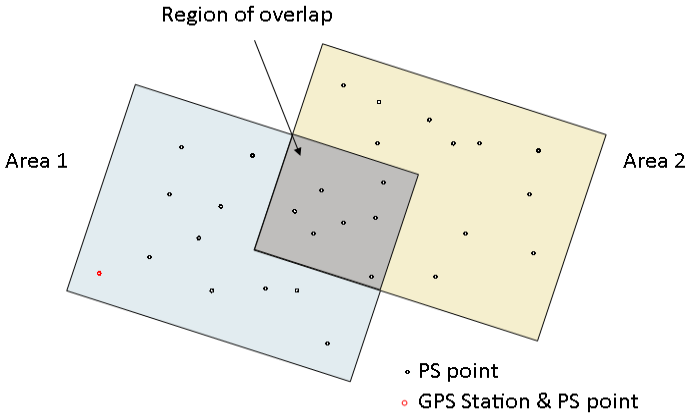

Figure 12: Post-Processing PS Point Ground Velocity Calibration Procedure

(3) Process PSI over two regions ("Area 1" and "Area 2"), making sure there is a RoO. The result is two areas of separate, relative ground velocity measurements. (2) Calibrate the relative velocities in "Area 1" to the absolute velocity measured at the known GPS station. (3) Calibrate the relative velocities in "Area 2" to the now-established absolute velocities in "Area 1". (4) Repeat this process in a piecewise fashion, always calibrating back to the initial, known GPS station in Alexandria.

In Alexandria, Egypt. Because all InSAR ground velocities are relative, an absolute GPS ground station was needed to convert the relative InSAR ground velocities to absolute velocities. After "Area 1" was processed and calibrated, a second region was then cropped (i.e., Area 2 – refer to Figure 12), making sure a region of overlap (RoO) was present. "Area 2" was then processed. After "Area 1 and 2" were individually processed, the RoO would presumably contain pixels with PS points from each processing step because PS locations are unknown prior to processing, sufficient PS points must be present in the RoO. When there are not enough PS points available in the RoO, one, or both of the areas would be re-processed with a different RoO target region between them.

The relative ground velocities from "Area 2" could then be calibrated to the now absolute ground velocities from "Area 1" by calculating the average difference between overlapping PS points in the RoO:

$$\Delta = \frac{\sum_{i=1}^{n}(Vel1_n - Vel2_n)}{n} \qquad \text{(Eq. 7)}$$

where Vel_1 and Vel_2 are the velocities of PS points in "Area 1" and "Area 2", respectively, and n is the total number of PS pairs. The value of n normally ranged from 50 to 100 PS pairs that could be used to calculate the ground velocity difference between respective RoO of each other (as long as each pair of PS points was within one DEM pixel length – based on Shuttle Range Topography Mission (SRTM) DEM resolution of 90 meters).

This piecewise procedure was performed across the entire Nile Delta. The acceptable root-mean-square error threshold of the difference in "Area 1 and 2" velocities was 0.5 mm/year or less. One concern with this piecewise procedure is the potential for cumulative error, as this was iterated (velocity differences were calculated over 50 times) across the study error. Unfortunately, with only one GPS station, there was no acceptable alternative method, with the exception of comparing ground velocities from this study to previous studies to see if similar trends could be observed. There is a discussion of results and potential errors in Chapter 4.

CHAPTER III

FACTORS INFLUENCING SUBSIDENCE RATE MEASUREMENTS IN THE NILE DELTA

Introduction

This chapter focuses on factors that influence subsidence rates in the Nile Delta. The first two sections, "Geology of the Nile Delta" and "Anthropogenic Influences on the Nile Delta," discuss variables that created and/or currently shape the delta and the roles they may have on influencing ground motion. The third section, "The Atmosphere above the Nile Delta Region," discusses the use of radar interferometry in such an atmospherically active region and the inherent difficulties that arise.

Geology of the Nile Delta

Geologic activity in the Nile Delta may be divided into two relevant parts for the for this study: (1) pre-Neogene tectonics, which increased the accommodation space for later sediments, and (2) Neogene and Quaternary sedimentology, which was the time period when the present Nile Delta region switched from being an inactive continental slope to an active delta system.

Pre-Neogene Tectonics

Tectonic activity, that still impacts ground motion in the Nile Delta today, began during the Jurassic period when a crustal break created the present-day blind fault boundary between the South Delta Block and the North Delta Basin (Figure 13). Currently, this crustal break is a tectonically inactive hinge zone surrounded by a 30-40 kilometer-wide flexure zone. Normal faulting within the flexure zone separates the North Delta Basin, a hanging wall block that dropped approximately 5 kilometers, from the northward tilting South Delta Block, which is part of the stable African plate (Schlumberger, 1984; Kamel et al., 1988, EGCP, 1994). The division between the South Delta Block and the North Delta Basin is evinced in north-south trending seismic surveys across the flexure zone, as shown by the interpreted seismic reflection profile from Barakat (2010) (Figure 14). This 31 kilometer survey, with a two-way travel time (TWT) of 8,000 milliseconds (8 seconds), illustrates the complexity of listric normal faults and rotated fault blocks that separate the South Delta Block and North Delta Basin.

The tectonic history of the Nile Delta can be separated into three phases (Zaghloul et al., 2001). Phase 1 occurred during the Mesozoic with rifting of the African Plate along with creation and expansion of the Tethys Sea (predecessor of the Mediterranean Sea). Phase 2 spanned the Late Cretaceous Period through the Eocene Epoch when the area underwent compression, creating thrust faults and forming the Paleo-Levant micro-continent (present day Israel, Lebanon, Syria, Palestine, and Jordan). Phase 3 occurred during the Oligocene Epoch, when the Nile Delta region transitioned to an extensional

tectonic regime. Vertical and listric normal faults that reach to basement rock created the offset between the North Delta Basin and the South Delta Block (Figure 14).

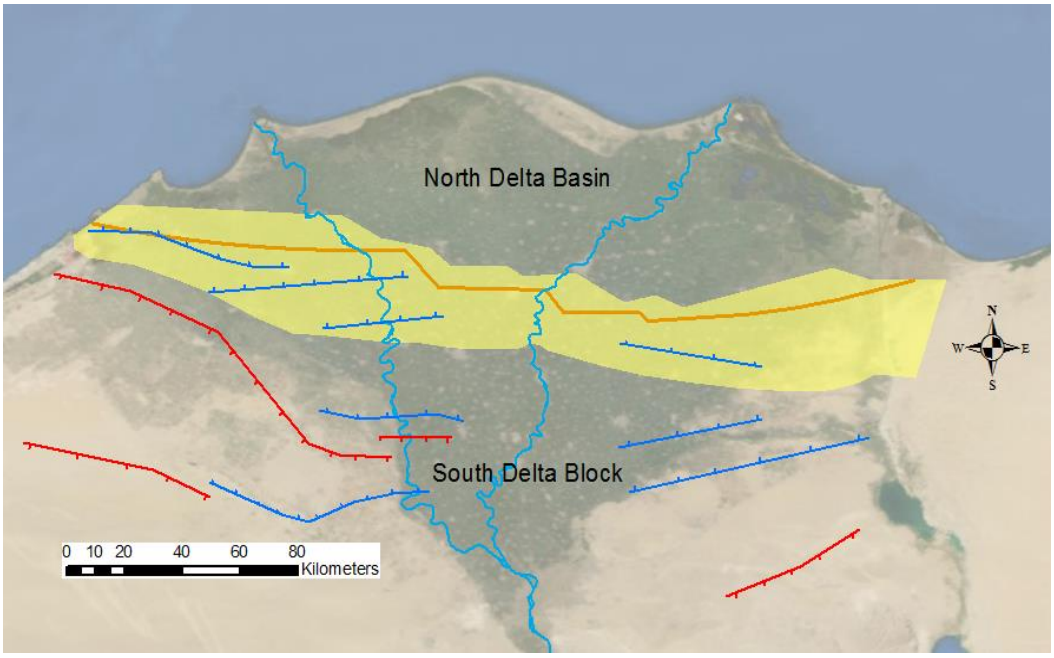

Figure 13: Subsurface Structures in the Nile Delta, Egypt

Subsurface structure of north-central Egypt showing heavily-faulted flexural zone (yellow), approximate location of west-east trending hinge line (orange), and north- and south-dipping normal faults (blue and red, respectively) that compose the quasi-horst and graben setting of the Nile Delta. (Redrawn from Sestini, 1989)

Sedimentology of the Nile Delta

Both the River Nile and the Nile Delta are thought to have their beginnings near the start of the Neogene Period. Beginning in the Miocene, five stages of the River Nile, Eonile, Paleonile, Protonile, Prenile, and Neonile, have all helped to shape the landscape of present-day Northern Egypt (EGPC, 1994). There have also been three main sedimentary cycles identified during this same time period (Zaghloul et al., 1977).

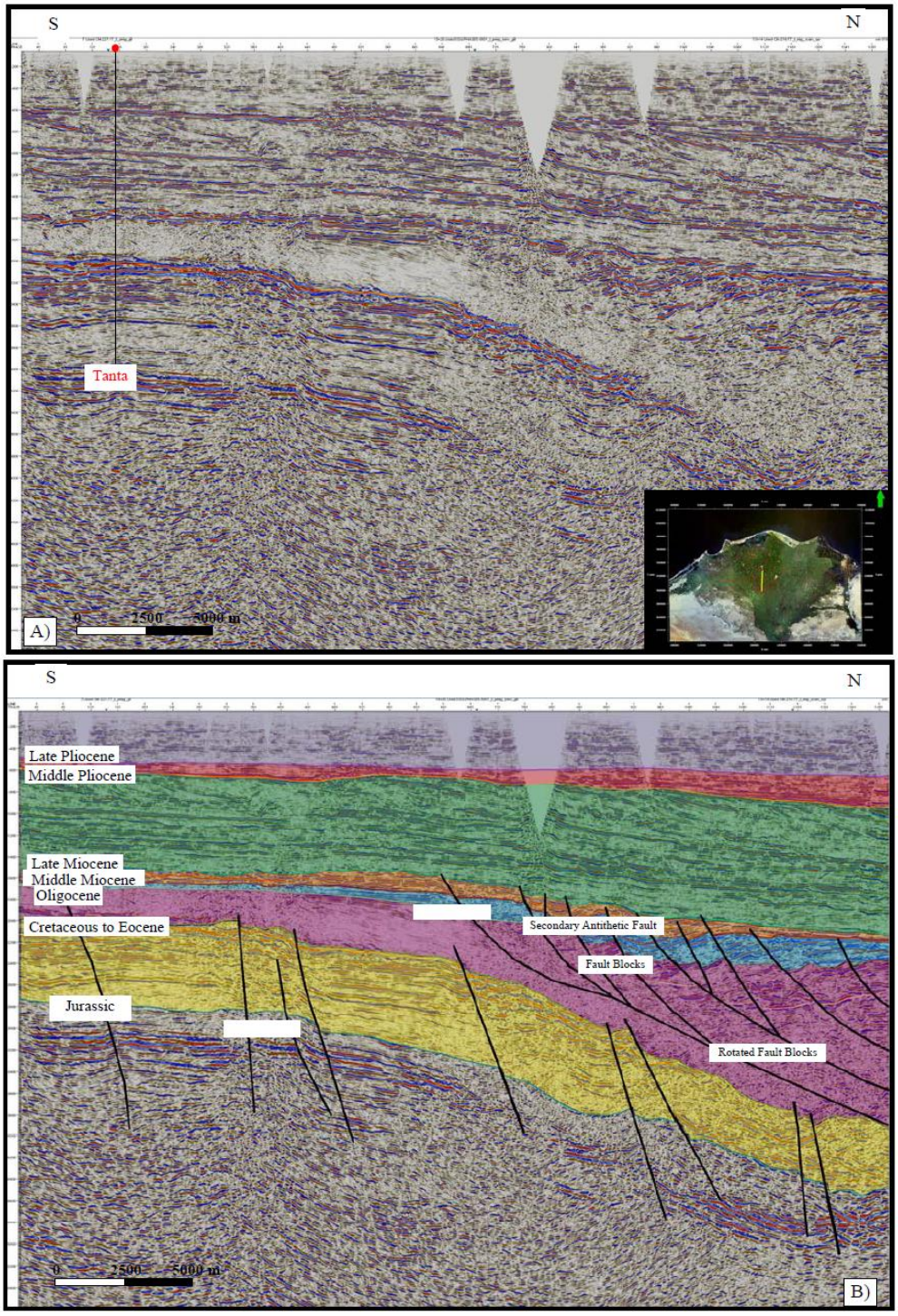

Figure 14: North-South Trending Seismic Profile across the Flexure Zone in the Nile Delta, Egypt (Barakat, 2010)

Neogene Period

Eonile Stage

The first sedimentary cycle occurred during the Miocene Epoch, when sea levels rose, and numerous transgressive sediments were deposited. The North Delta Basin also began taking shape during this time. Increased accommodation space allowed for deposition of thick Neogene sediment packages in the north (Said, 1981). Evidence of the flexure zone is observable in the deltaic stratigraphic column, which shows the increase in sedimentation in the North Delta Basin as structural contours to the top of the Oligocene boundary (Figure 15). The closely-spaced, west-east trending contours generally align with the hinge line/flexure zone shown in seismic profiles, indicating a rapid increase in accommodation space (from 600 meters just north of Cairo to >4,200 meters in the northeastern Nile Delta) in post-Oligocene periods.

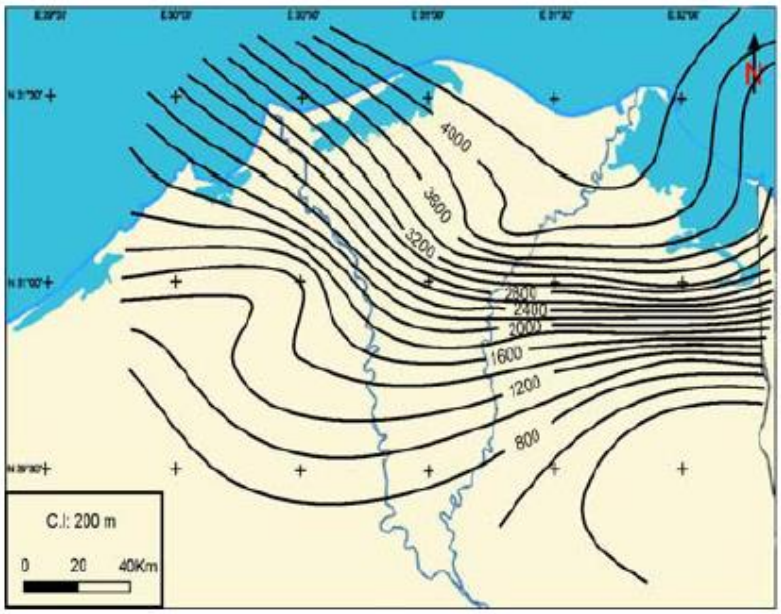

Figure 15: Structural Depth Contours to the Top of the Oligocene Boundary (meters) (Zaghloul et al., 1999; Barakat, 2010).

The sea level began to fall by the Late Miocene, and a period of regression initiated the second sedimentary cycle. Increased stream gradient allowed for the formation of a high-velocity Eonile, which incised through these Miocene sediments (Ross & Uchupi, 1977; Barakat, 2010). The second sedimentary cycle continued into the Pliocene Epoch.

Paleonile Stage

The relatively brief period of sea regression (Late Miocene) transitioned into a large Mediterranean Sea transgression during the Early Pliocene. Sea level rise drastically lessened the flow of the Nile, forming the Paleonile (second stage). The deltaic setting during this period was similar to the Nile Delta today. High sea level and high flow of the Paleonile continued through the Pliocene (EGPC, 1994). By the end of the Pliocene, a tectonically active west-east trending belt, representing the flexure zone, had completely divided the Nile Delta into two distinct regions: (1) the mobile North Delta Basin, and (2) the stable Mesozoic platform South Delta Block (Zaghloul et al., 1977).

Quaternary Period

The third and final sedimentary cycle of sea regression began in the Pleistocene Epoch. The Paleonile stopped flowing north during the large glacial event of the Middle Pleistocene. This glacial event, while covering Scandinavia, Canada, and Siberia, created harsh desert conditions in North Africa; the hot, dry conditions led to evaporation of the Paleonile and a blanketing of sand dunes across the river channel in northern Egypt (Figure 16) (Barakat, 2010).

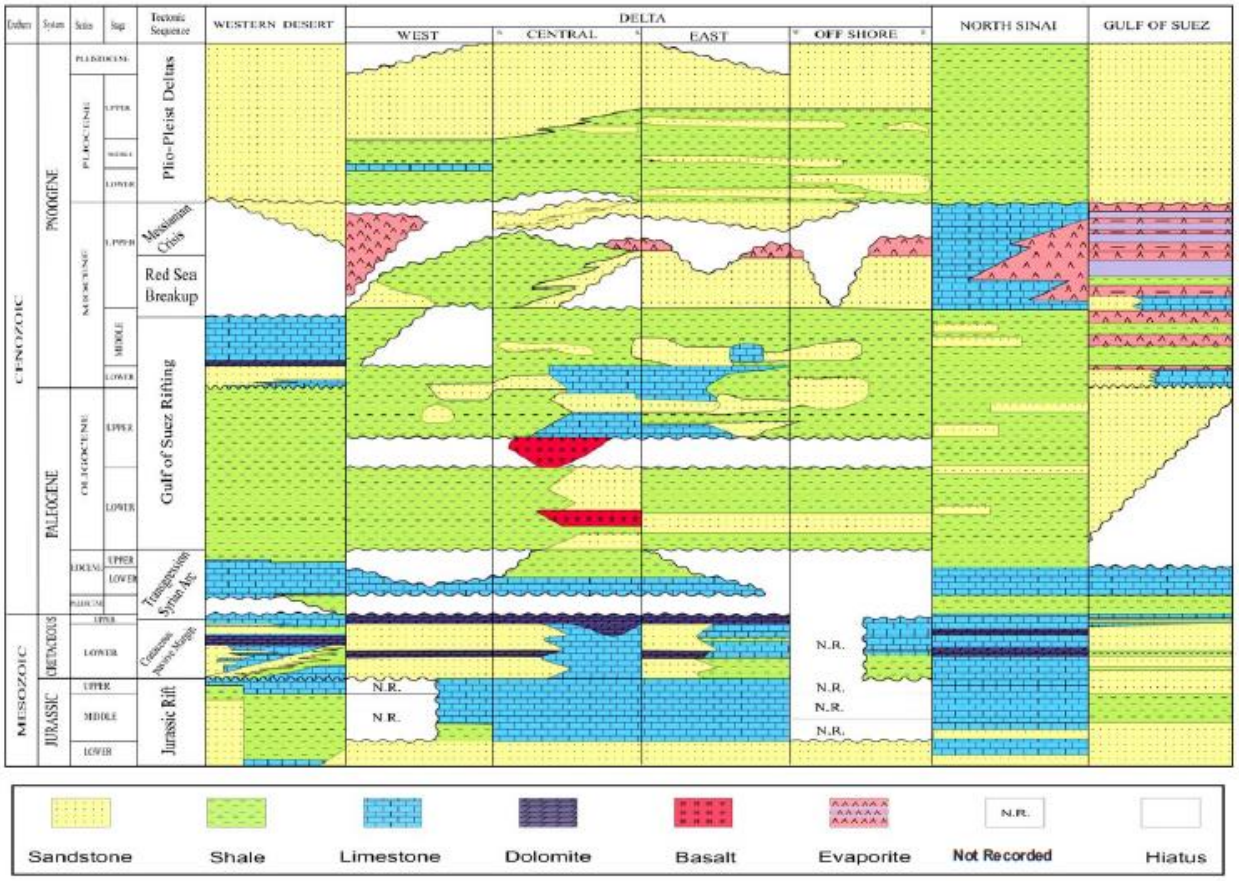

Figure 16: Stratigraphic Column of Northern Egypt, Mesozoic to Recent

Stratigraphic column of (1) the Western Desert (west of the Nile Delta), (2) Nile Delta (west, central, east, and off shore), and (3) the Gulf of Suez (east of the Nile Delta) from the early Mesozoic to recent (taken from Schlumberger, 1984).

Protonile Stage

The post-glaciation period, starting in the Middle Pleistocene, initiated the reconnection of the Mediterranean Sea to southern Egypt via the Protonile (third stage). The change in climatic regime from arid to temperate contributed to the reestablishment of the Protonile. Coarse sands, gravels, and conglomerates were deposited during this time (Said, 1981).

Prenile Stage

The fourth stage was the Prenile, the largest and most high-energy of any of the river stages. Widespread and thick floodplain deposits are evidence of the vigorous nature of the Prenile. It was in existence approximately 700,000 to 200,000 years ago (Said, 1981).

Neonile Stage

The fifth and final river stage is the Neonile. It was established during a wet period approximately 120,000 years ago and still flows to this day. The Neonile was not just one or two river distributary branches. Instead, beginning about 12,000 years ago at the beginning of the Holocene Epoch, the Nile Delta underwent many wet-dry cycles. This in-turn led to a wide distribution of meandering distributaries. During the Neonile, the distribution system built the Nile Delta its widest spread. It extended as far eastward as the ancient Pelusiac branch and as far westward as the Canopic branch (Figure 17). There were as many as nine discharging outlets that have so far been identified (Hamza, 2001). Only two of the outlets are active today: the Rosetta Branch, which receives more than 70% of the water flow through the Nile system, and the Damietta Branch, which receives the remaining 30% of the flow (Figure 18 – Barakat, 2010).

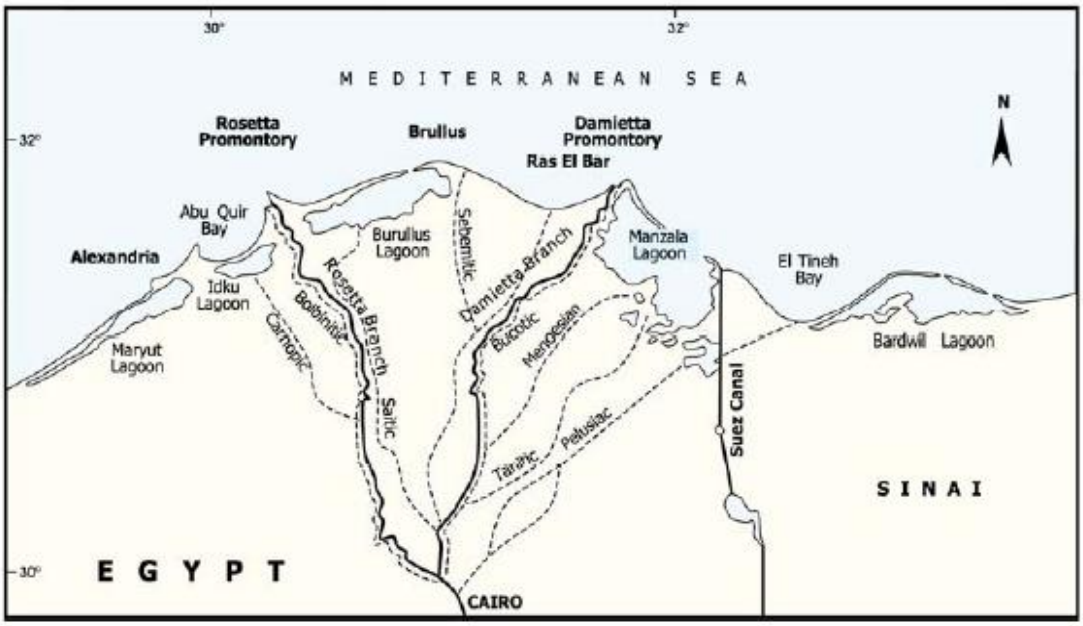

Figure 17: Current and Ancient Boundaries of the River Distributary Branches and Outlets of the Nile Delta. (Image taken from Hamza, 2001)

Figure 18: Satellite Image of the Nile Delta in Egypt

A satellite image composite of the Nile Delta, Egypt, as observed by the Moderate Resolution Imaging Spectroradiometer (MODIS), an instrument on ENVISAT. The River Nile bifurcates just north of the city of Cairo into the Rosetta and Damietta branches.

Anthropogenic Influence on the Nile Delta

The Nile Delta has been heavily adapted to suit increased human population growth over the last half-century. Now that the population is nearing 50 million (of a total 80 million in Egypt), anthropogenic influences on the delta are pronounced. Possibly the greatest consequence of population growth is the apparent change in deltaic sedimentation. The Nile Delta is now receding because sediment erosion is greater than sediment accumulation along the Mediterranean coast. The switch from delta progradation to regression has been clearly correlated to increased human activity within and around the Nile Delta (Stanley, 1996).

In 1902 and 1964 the Aswan Low Dam and High Dam were built, respectively, forming a reservoir known as Lake Nassir behind the High Dam (Figure 19 – Sharaf El Din, 1977). The resulting reduced Nile River flow rate and the man-made obstructions lessened the sediment load downstream past the dams. Many barrages (or small dams) have also been built along the River Nile, south of Cairo and the Nile Delta, to further regulate river flow (Elassiouti, 1983). Also, within the Nile Delta, a complex series of canals for irrigation and water usage drastically reduces the water flow, in some places to the point of stagnation, which results in deposition of silts, clays, and sands within the canals. These sediments never reach the Mediterranean Sea (Figure 20). The canals are occasionally flushed, thereby exhuming these fine-grained deposits. This sediment-laden water is eventually released into coastal lagoons (Stanley, 1996: e.g., Manzala Lagoon, Idku Lagoon, Barullus Lagoon, or Maryut Lake – all extremely shallow water bodies).

Figure 19: Landsat Imagery of Egypt from Google Earth

The Aswan High Dam is located in southern Egypt, just north of Lake Nassir (or Lake Nasser). The Aswan Low Dam is located 6 kilometers downstream (north) from the Aswan High Dam.

Maryut Lake has its deepest point at 2.2 meters (Abdel-Moati & El-Sammak, 1997). Prior to the emplacement of barrages and the Aswan High and Low Dams, approximately 80 million cubic kilometers of water was discharged into the Mediterranean Sea from outlets within the Nile Delta (Eldardir, 1994). Presently, approximately 7 to 10 million cubic kilometers of water is discharged per year from the lagoons, and less than 6 million cubic kilometers of water is discharged per year from the Rosetta and Damietta Branches (Sestini, 1992).

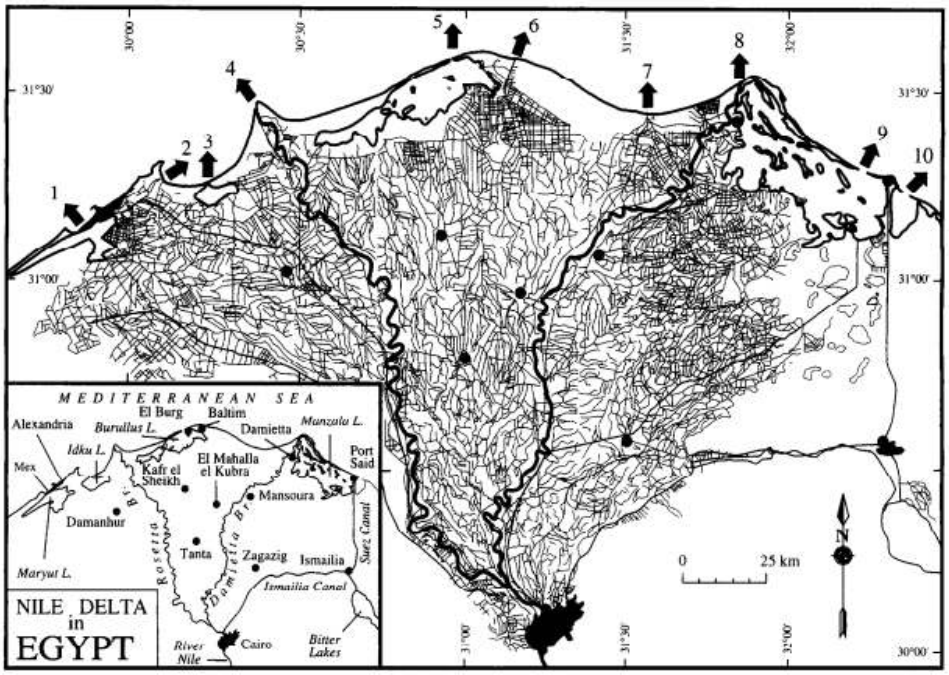

Figure 20: 1993 Map of Irrigation Canals in the Nile Delta

Irrigation canals and drainages across the Nile Delta (image from Stanley, 1996 – data compiled by the Defense Mapping Agency between 1970 and 1993 – DMA, 1993). Back in 1993, there were already over 10,000 kilometers of man-made, flow-regulated canals. Cairo is the large black area at the south-center of Figure 20. The Rosetta Branch (west) and Damietta Branch (east) are shown as bold black lines meandering northward from Cairo to the coastline. Ten points of discharge are marked by arrows and numbers. Only two of the ten outlets are 'natural flows' (4: Rosetta; 8: Damietta). The remainders are heavily influenced by irrigation canals and drainage systems that mainly discharge from lagoons or lakes.

Other, more noticeable changes within the Nile Delta are due to population increase. Consequently, conversion of land use from "uninhabited" to "urban cities" and "agricultural lands," has accelerated to sustain human growth throughout the last century. The Nile Delta is now the most densely populated delta in the world with approximately 1,920 people per square kilometer (Stanley & Warne, 1998). The sheer density "of everything" (people, irrigation canals, agricultural land, and general man-made

structures) has led to the expansion and "reclamation" of areas along the desert-delta boundary in the southwest and southeast Nile Delta (Bakr et al., 2010). The population increase in urban areas has created the need for: (1) construction of buildings and other man-made structures, (2) more diverse sources of water (e.g., groundwater pumping), and (3) continued conversion of barren land (or presently arid land) into agricultural plots or villages/cities. Stanley & Warne (1993) provided a grim prediction of the status of the Nile Delta in the year 2050 (Figure 21).

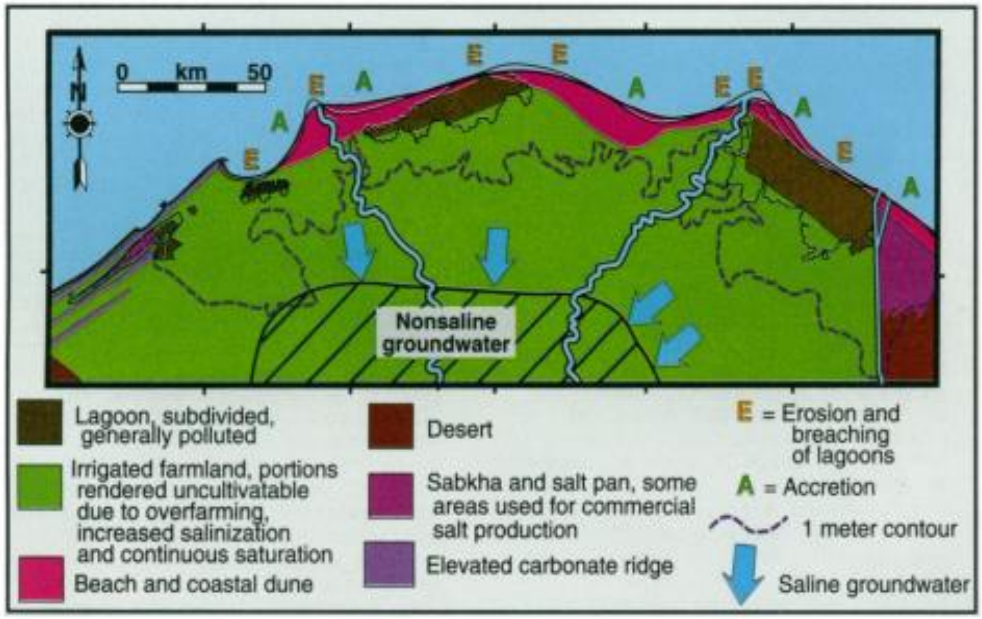

Figure 21: A Prediction Model of the Northern Nile Delta in 2050
Stanley & Warne (1993) predict the status of the Nile Delta in the year 2050. The current shoreline, elevation (1-meter contour), and river branches are also shown as a comparison.

The anthropogenic factors discussed above (blockage of sediment transport, population growth, land use changes, and subsurface groundwater extraction) have all played a role in the increase of subsidence rates across the Nile Delta over the past few

decades. How each of these variables affects, or stimulates, subsidence in a deltaic environment is discussed further in Chapter 4.

The Atmosphere of the Nile Delta Region

The atmospheric conditions over the Nile Delta are highly variable. Although this indirectly applies to the geology and subsidence of the Nile Delta (e.g., in the form of precipitation), it is important to understand the atmosphere, and its effects, upon satellite-borne radar waves travelling through it.

The term "atmospheric activity" is shorthand for discussing the spatial distribution of solids, liquids, and gasses in the troposphere. The troposphere is the lowest and most active portion of the Earth's atmosphere. It is the densest part of the atmosphere and contains 99% of all atmospheric water vapor (McGraw-Hill, 1984). The troposphere also contains turbulence and air flow (e.g., the jet stream), temperature and pressure gradients, and a majority of the aerosols (e.g., pollution, water vapor, precipitation, dust and particulates, et cetera) found in the atmosphere.

The troposphere above the Nile Delta carries variable amounts of water vapor (measured as the water vapor column) in a seasonal cycle, and concentrations of other aerosols in a quasi-seasonal cycle. The water vapor column is thickest during autumn months (Figure 22). Aerosol concentrations in the atmosphere vary widely throughout the year. Remote sensing observations that use the aerosol optical depth (AOD) calculation show concentration peaks in the spring (Figure 22), while data obtained via field measurements over the same region show concentration peaks during the summer

(Figure 23). Regardless of when peak aerosol concentration occurs, both studies (Favez et al., 2008; El-Askary & Kafatos, 2008) conclude that aerosol levels are relatively high throughout the entire year throughout the Nile Delta. Both atmospheric spatial (lateral) and temporal variations in aerosol concentrations are also observed (Figure 24).

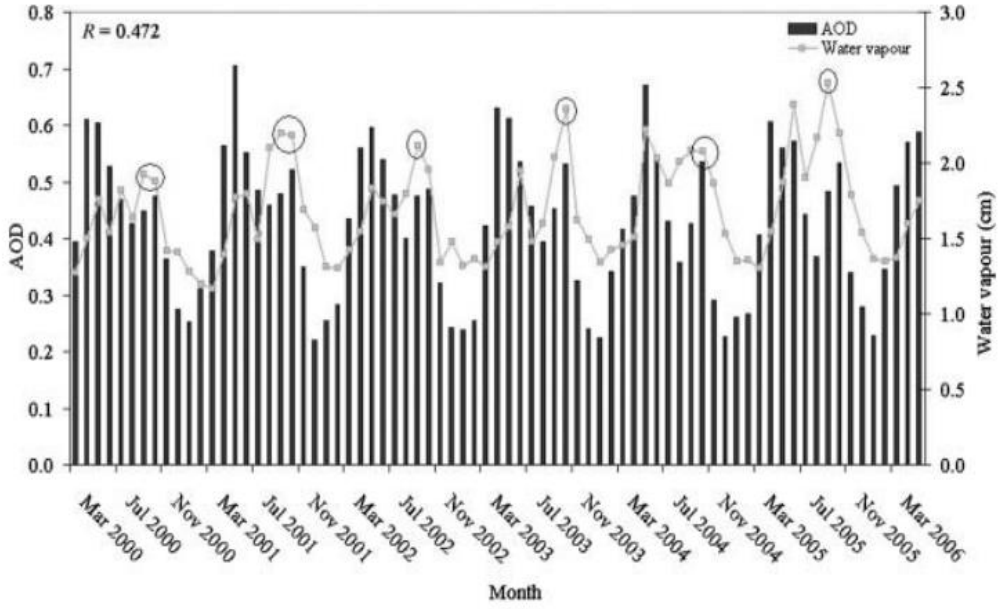

Figure 22: Water Vapor Column and Aerosol Optical Depth over the Central Nile Delta, March 2000 – March 2006

Monthly averages of water vapor column in centimeters and aerosol optical depth (AOD – a measure of transparency). The AOD is the percentage of light that has been scattered or absorbed by aerosols in the troposphere. Graph from El-Askary & Kafatos (2008). It shows the cyclical nature of the water vapor column and AOD over the central Nile Delta, from Cairo to the Mediterranean Sea.

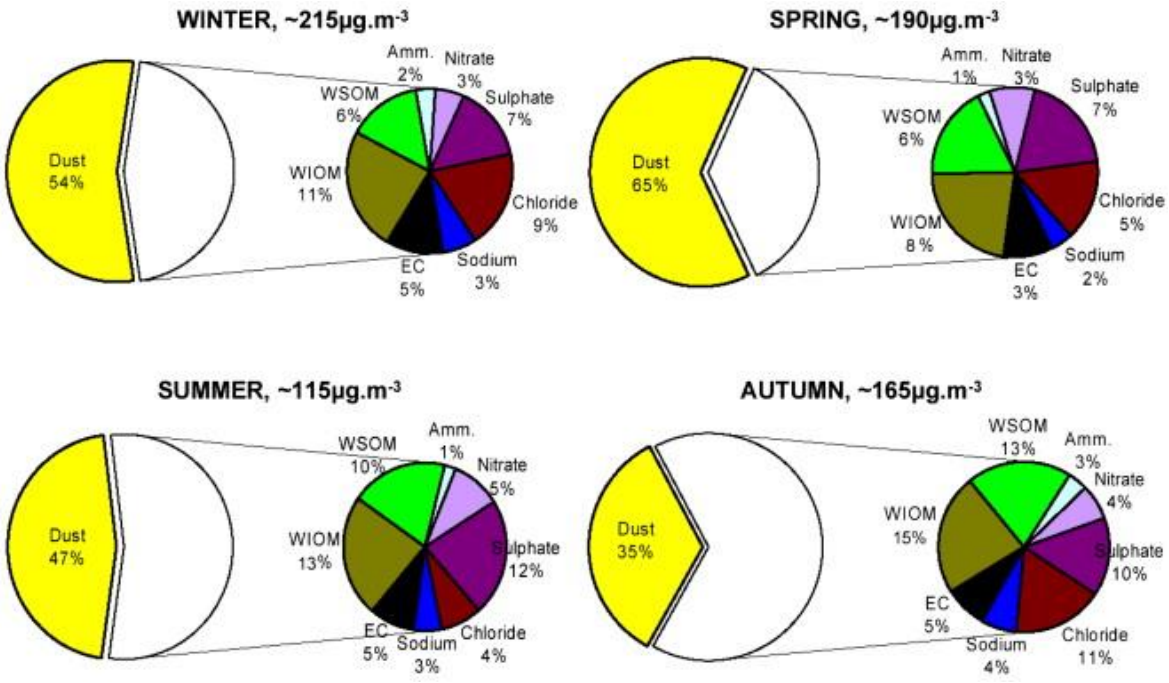

Figure 23: Aerosols in the Atmosphere – by Type – over Cairo, Egypt.

Aerosol contributions (by type) divided into seasonal sections (image from Favez et al., 2008). Field data were obtained from two sites located within the Cairo metropolitan area between January 2003 and May 2006. Types of aerosols include: dust, ammonium (Amm), nitrate, sulfate, chloride, sodium, water soluble organic carbon (WSOC), water insoluble organic carbon (WIOC), and elemental carbon (EC).

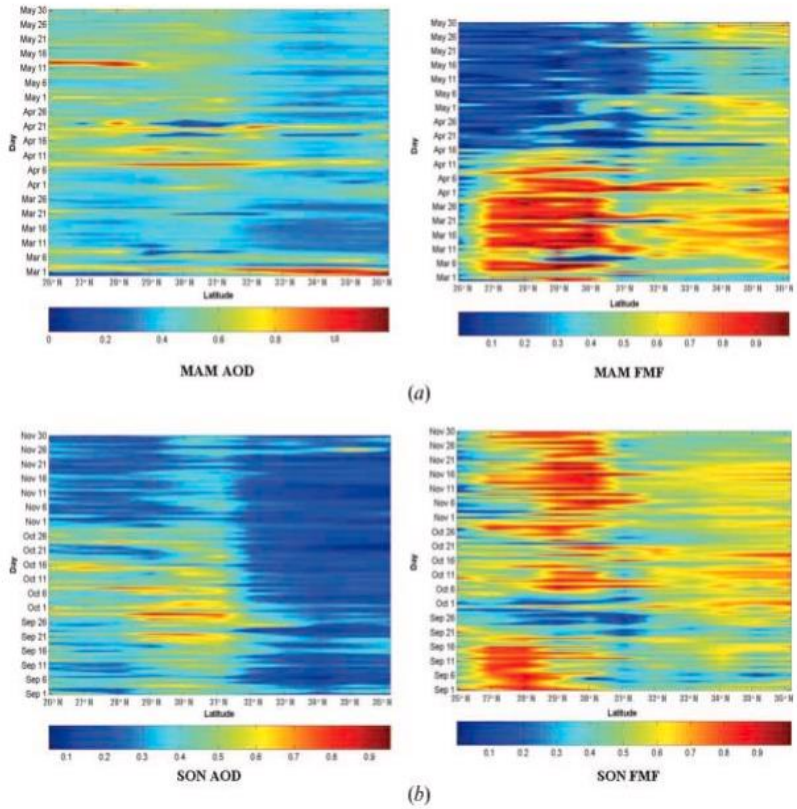

Figure 24: Spatial and Temporal Distribution of Aerosol Optical Depth and Fine Mode Fraction across the Nile Delta

AOD and fine mode fraction (FMF) over the central Nile Delta from Cairo to the Mediterranean coastline in the spring (a) and the autumn (b) (El-Askary & Kafatos, 2008). FMF is the fraction of AOD attributable to fine aerosols (radius between 0.1 and 0.25 micrometers).

The dynamic and variable atmosphere poses problems for radar interferometry usage for two reasons: (1) floating solids and liquids physically scatter radar waves, and more importantly (2) moisture decreases the velocity of radar waves traveling through this medium. The first problem decreases the return amplitude, but the second problem actually changes the phase of the incoming radar waves. Positive phase changes result in calculations of *greater distance* between the satellite and its target. Subsidence

measurements, in terms of the Nile Delta, would appear to be greater than actual rates obtained via field measurements. Atmospheric effects contribute to the largest error in radar interferometric techniques. The method used to avoid, or to at least assume null atmospheric variability was described in Chapter 2.

The extent of the atmospheric effect on radar waves can be observed in Figures 22-24. The peaks in the water vapor column and AOD (Figure 22) are offset by 4-5 months. AOD values range drastically, from approximately 0.2 to 0.7. The average AOD value (0.4) is still relatively high. Water vapor column thickness ranges from approximately 1.4 to 2.5 centimeters. Not only are radar waves scattered by floating solids/liquids (AOD), but they are slowed down "twice" by the water vapor column due to two-way travel distance. Figure 23 illustrates the density and wide range of aerosol composition. Geometry, size, and abundance of each type of aerosol scatter radar waves differently. Figure 24 shows the high lateral and temporal variability of the AOD and fine mode fraction (FMF) across the Nile Delta. The use of radar interferometry becomes much more difficult over areas where atmospheric effects (and phase changes) completely differ between locations within one cropped area. Normally, one usually tries to avoid cropping (and processing) a region with high atmospheric variability, because it is so difficult to create a model that corrects for these spatially complex errors.

The next chapter (Chapter 4) will discuss the results and interpretations of subsidence rates across the Nile Delta, and will address potential measurement errors that relate particularly to lateral atmospheric gradients when applying PSI to a large region.

CHAPTER IV

RESULTS AND DISCUSSION

Introduction

The Nile Delta is a vital economic asset to the country of Egypt and its millions of inhabitants. Unfortunately, due to the increased effects of climate change and additional natural phenomena, such as land subsidence, the well-being and livelihood of future generations in the delta is at risk. Encroachment of the Mediterranean Sea on the Nile Delta has been well-documented (Stanley & Warne, 1993; Frihy et al., 1994; White & El Asmar, 1999; El Banna & Frihy, 2009) and the magnitude of the rise in regional sea level is being actively monitored (Cazenave et al., 2001; Cazenave et al., 2002; Calafat & Jordà, 2011). Measuring subsidence rates within the Nile Delta has also been a major focus throughout the past few decades (Stanley & Warne, 1993; Aly et al., 2009; Becker & Sultan, 2009; Poscolieri et al., 2011; Aly et al., 2012; Marriner et al., 2012). Radar interferometric techniques are the recent method of choice. However, the application of radar interferometry to the Nile Delta has only been performed on a city-scale, and not on a regional (deltaic) scale. This study attempts to expand this analysis to the broader regional scale.

Subsidence rates across the Nile Delta have been measured using PSI. This is a radar interferometric technique that requires consistent high-amplitude radar returns (high

coherence) on a sub-pixel level over a relatively long period of time (e.g., multiple acquisitions over multiple years). The delta is highly populated, yet large in area and densely vegetated. This results in a spatially complex framework of pixels ranging from highly coherent to incoherent. Therefore, there is a preference to assess the subsidence of the Nile Delta within urban areas where PSI works well. Here, regions of high vegetation become incoherent due to the seemingly random nature producing surface and volumetric backscattering.

A conundrum arises when trying to adequately describe subsidence rates using PSI. How does one portray the detail and complexity found at city-scale, inherent in this interferometric synthetic aperture radar (InSAR) technique, while simultaneously discussing subsidence trends at a regional delta scale?

One answer is that this spatial sampling problem may be addressed by the systematic confinement of PSI to urban areas. This constrains possible locations of coherent pixels and mandates a city-scale focus. However, this does require a detailed analysis of the delta in a piecewise fashion.

Another reason these satellite-based subsidence measurements must be compiled piecewise is due to the large areal extent of the delta. It is too large to be encompassed in one stack of single-look complex (SLC) radar images. Also, further errors arise when processing large regions in a single stack (see the Error Analysis section below). Understanding the complexity of subsidence signatures measured by PSI within urban areas is vital to an understanding of the necessity for simplification at a regional level.

Therefore, a few city-scale subsidence results are presented prior to the discussion of regional-level subsidence throughout the Nile Delta.

Nile Delta Subsidence Results

Subsidence rates measured via radar interferometry, using the SARscape and StaMPS programs, cover a large area of the Nile Delta (Figure 25). PSI results are best discussed on two spatial scales: (1) the complex subsidence signatures found at the city-scale, and (2) a comparison of average subsidence rates (per city) on a regional scale.

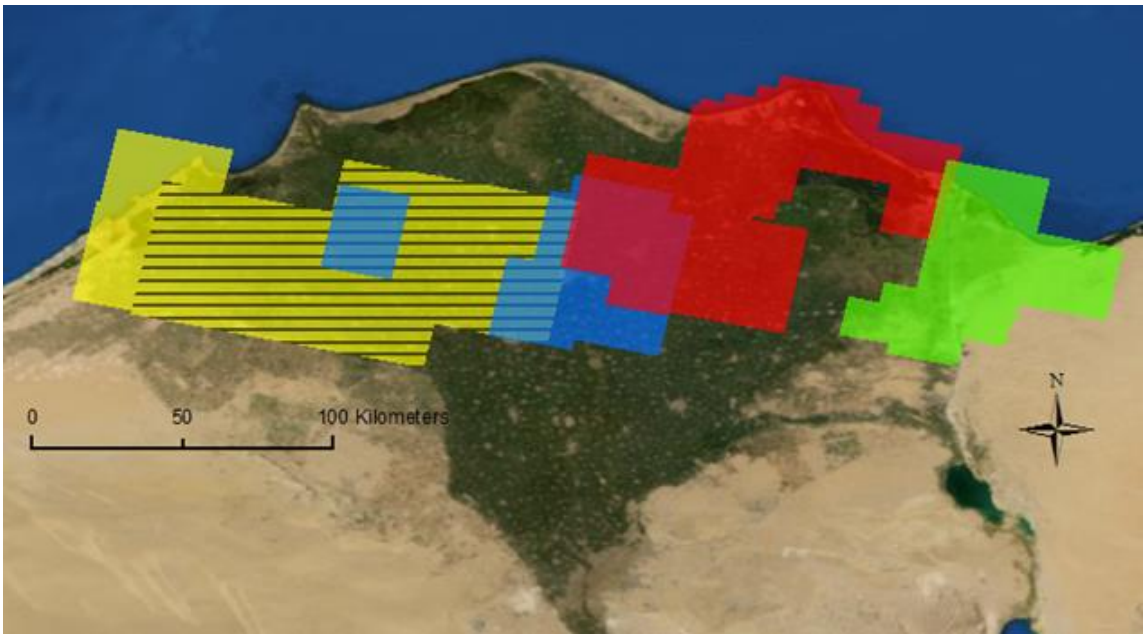

Figure 25: Processed Regions of the Nile Delta using PSI

Regions of the Nile Delta processed with PSI, divided by track: Yellow – Track 436, Blue – Track 164, Red – Track 436, and Green – Track 479. Regions marked with horizontal lines were processed using StaMPS. Regions without horizontal lines were processed using SARscape.

City-Scale Results

It would be misleading to discuss the averaged regional subsidence rates without mentioning the fact that many cities display a wide range of ground motion velocities in a spatially complex manner. Figures 26 and 27 show the distribution of subsidence rates in the cities of Damietta and Alexandria, respectively. These two cities were chosen to show the two extremes of the subsidence signature spectrum: (1) Damietta: variable, wide-ranging, subsidence rates that appear segmented on the neighborhood scale; (2) Alexandria: mainly stationary, a large portion of the city is stable, with small subsiding pockets. Most other cities in the Nile Delta exhibit a subsidence signature complexity

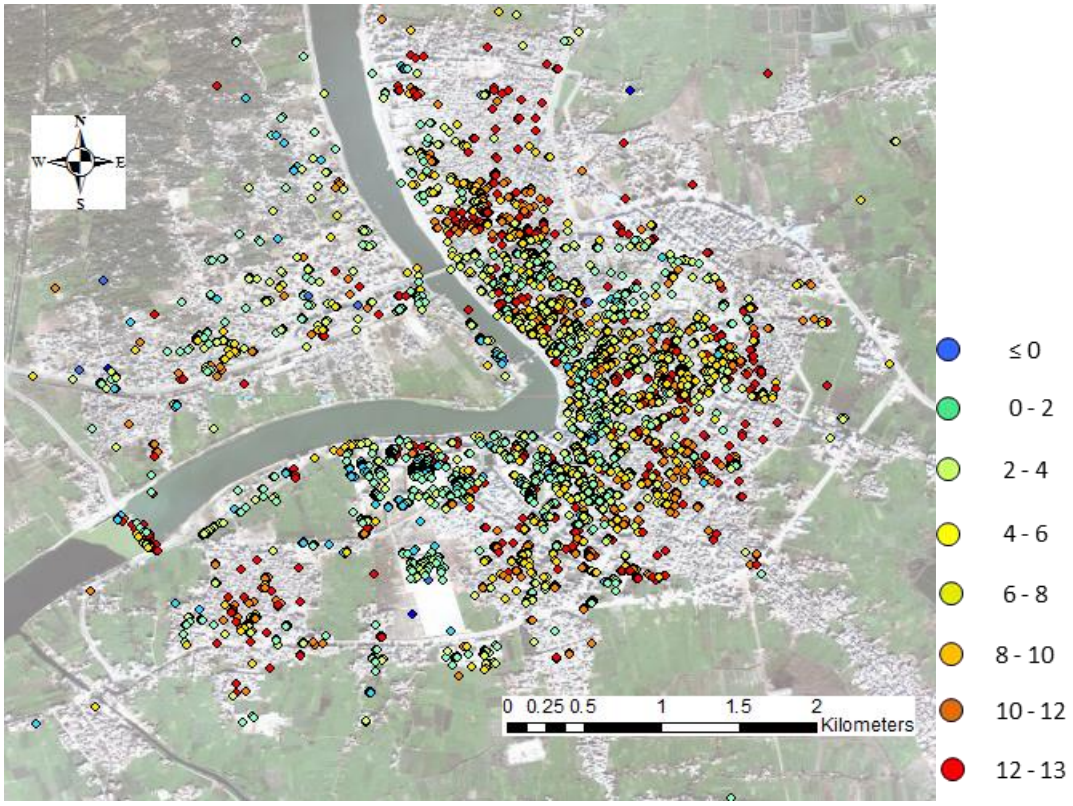

Figure 26: Subsidence Rates (mm/year) in Damietta, Egypt.
The data were processed using the SARscape program.

Somewhere between Damietta and Alexandria. For example, the average subsidence rate for Port Said is 0.5 mm/year (standard deviation: 0.86 mm/year, range: 7 mm/year) compared to Damietta which is 6 mm/year (standard deviation: 1.5 mm/year; range: 10 mm/year), Ras El Bar is 10 mm/year (standard deviation: 2 mm/year, range: 10 mm/year), and Mansoura is 6 mm/year (standard deviation: 2 mm/year, range: 12 mm/year).

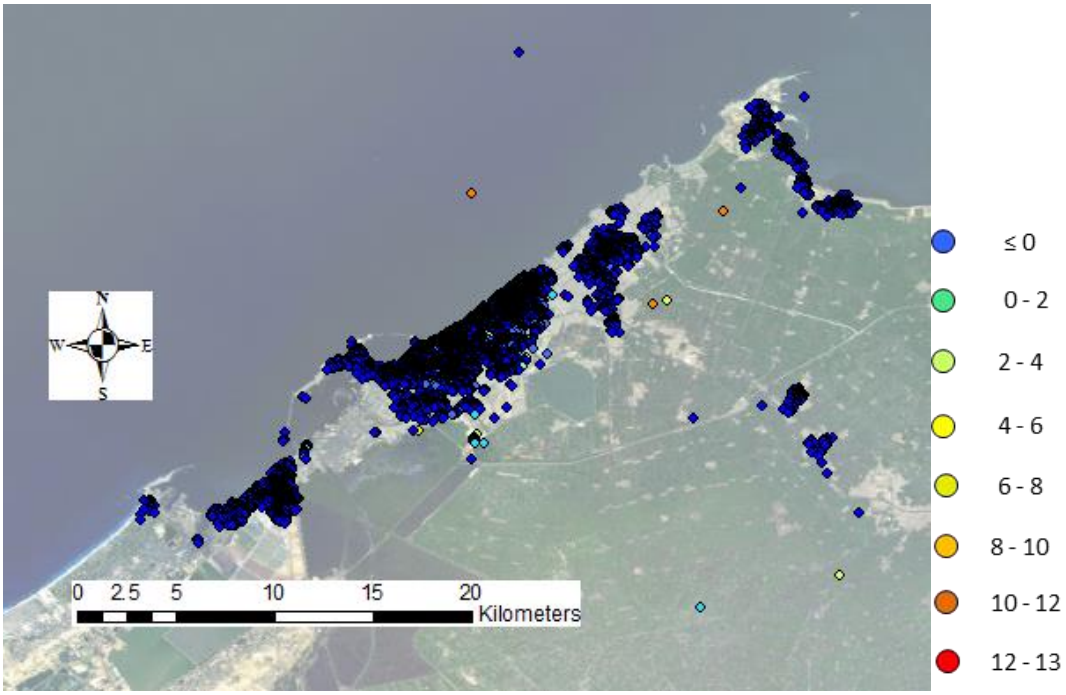

Figure 27: Subsidence rates (mm/year) in Alexandria, Egypt.
The data were processed using the SARscape program.

Regional Results

Figure 28 displays the spatial distribution of average subsidence rates of 338 high coherent cluster locations across the Nile Delta. Average subsidence rates vary from 0 mm/year to 10 mm/year. Subsidence rates are rounded to the nearest millimeter. Positive values imply downward movement in the line-of-sight (LOS) direction, which is away from the satellite.

The spatial distribution of subsidence rate measurements illustrates the goal of the study. This is to understand the ground motion of the Nile Delta as a system.

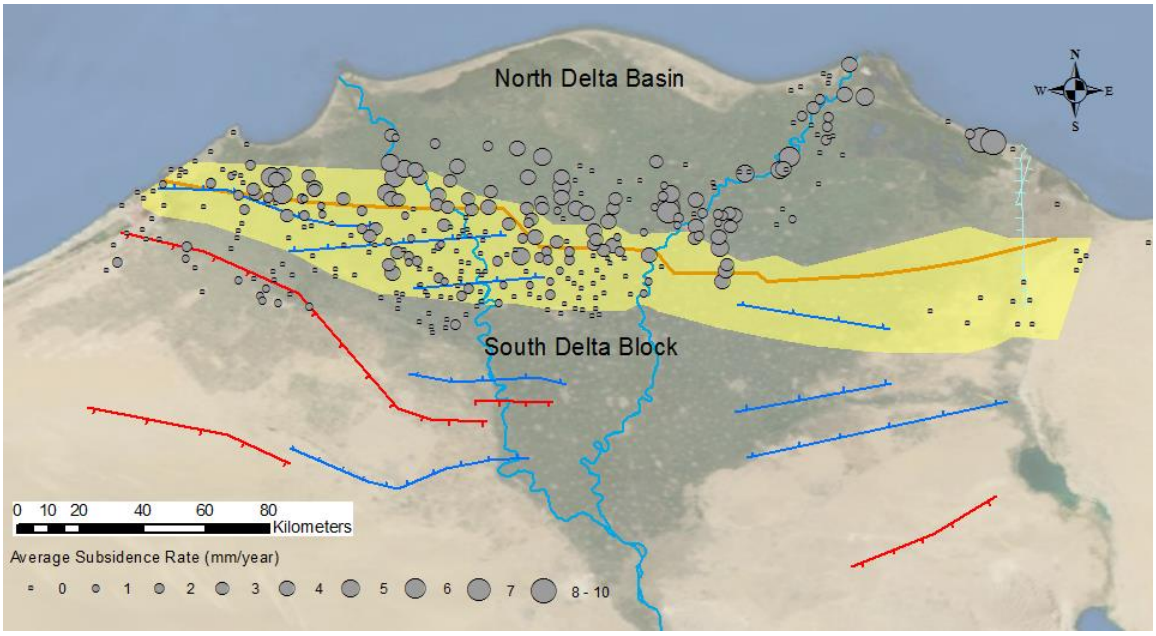

Figure 28: Average Subsidence Rates (mm/year) Throughout the Nile Delta

Subsurface structures are also marked on the map: west-east trending hinge line (orange), flexural zone (yellow), north-dipping normal faults (blue), and south-dipping normal faults (red).

Coastal margins and highly populated cities along with Rosetta and Damietta River Branches have been greatly studied (Aly et al., 2009; Becker & Sultan, 2009; Poscolieri et al., 2011; Aly et al., 2012). Aly et al. (2009) measured average subsidence rates of 7 mm/year in Cairo, Egypt using 34 ERS-1 and ERS-2 radar scenes from 1993 to 2000. Becker & Sultan (2009) focused on ground motion at the mouth of the Damietta Branch (basically from the city of Damietta to Ras El Bar, Egypt). They measured subsidence rates ranging from 0 mm/year in regions away from the Damietta River Branch and Manzala Lagoon, to 8 mm/year in Ras El Bar and in the Manzala Lagoon, using 15 ERS-1 and ERS-2 radar scenes from 1992 to 1999. Poscolieri et al. (2011) used 38 ENVISAT scenes, from 2003 to 2009, to measure subsidence rates as high as 7 mm/year in the Greater Cairo Metropolitan Area, confirming rates measured by Aly et al. two years prior. Aly et al. (2012) also processed 39 ERS-1 and ERS-2 scenes, between 1993 and 2000, in the cities of Mansoura and Greater Mahala along the Damietta River Branch. Maximum subsidence rates up to 9 mm/year and 5 mm/year, respectively were measured. These four studies illustrate the general subsidence trend in the Nile Delta. Average subsidence rates increase toward the northeast of the delta. Although all four of these studies focus on cities along the Damietta River Branch, there are still large spatial gaps between Cairo, Mansoura, Damietta, and Ras El Bar (Figure 18) and, therefore, large gaps in our understanding of the nature of subsidence between these large cities.

Therefore, the goal of this study was to reprocess and connect much of these previously examined regions (e.g., Ras El Bar, Damietta, Mansoura, and Alexandria), along with previously unprocessed parts of the Nile Delta (e.g., along the flexural zone

on the delta-desert boundaries), to further develop an understanding of ground motions occurring on a regional, deltaic scale. The Nile Delta may generally be divided into two subsidence regimes: north and south of the flexure zone.

Subsidence rates are generally greater north of the flexure zone when compared to the south. North of the flexure zone, in the North Delta Basin, cities with the greatest average subsidence rates (≥4 mm/year) are located near the Damietta River Branch, in the east where present-day and geologically recent (Holocene) sediments have been deposited, and directly north of the hinge line, such as in the west where subsidence rates are as high as 6 mm/year. Maximum average subsidence rates (10 mm/year) were measured at the mouth of the Damietta River Branch. South of the flexure zone, in the South Delta Block, there are small regions of subsidence (<4 mm/year), but the vast majority of cities are experiencing no subsidence or slight uplift (Mahmoud et al., 2005). There can be traced an imaginary west-east trending line across the delta between the region of subsidence and that of little-to-no subsidence, which approximates the location of the line of flexure (and hinge zone) separating the North Delta Basin from the South Delta Block (Sestini, 1989; Stanley & Warne, 1998); the city of Alexandria may be considered as the northernmost extent of the stable South Delta Block in the western Nile Delta, and the flexure zone/hinge line step southward towards the east.

Interpretation and Discussion

The Nile Delta appears to have two subsidence regimes throughout the region covered by interferometric analysis (Figure 28). These are (1) the North Delta Basin and (2) the South Delta Block. These regions display subsidence rates that differ from each other, sometimes with abrupt boundaries (e.g., the hinge line approximates the spatial decrease in subsidence rates from the North Delta Basin to the South Delta Block in the western Nile Delta). The dominant natural factor controlling subsidence is interpreted for each of these two regions.

Ancient tectonic boundaries, primarily blind Mesozoic normal faults, play a major role in separating subsidence and no subsidence or uplift regions (Figure 29). The region of greatest subsidence (as much as 6 mm/year) in the western delta appears directly north of the hinge line. Another region of higher subsidence is located in the very southwest portion of the study area. This area displays moderate subsidence rates (2-3 mm/year) and is situated southwest of a south-dipping, normal fault. The higher subsidence rates are in the two graben (basin) locations, with the footwall of the ancient normal faults as a stable, horst region of no subsidence.

The flexure zone and hinge line are locations of crustal bending and, just like the subsurface faults, are not locations of active slip. According to the USGS Earthquake Database, there has been only one earthquake (M = 4.1) within the Nile Delta proper since the early 1980s (USGS, 2013). Instead, the dramatic change in subsidence rates, probably due to variations in sediment thickness caused by compaction, create a natural

boundary between subsidence variations that aligns with these faults and the flexure zone (Figures 28 and 29).

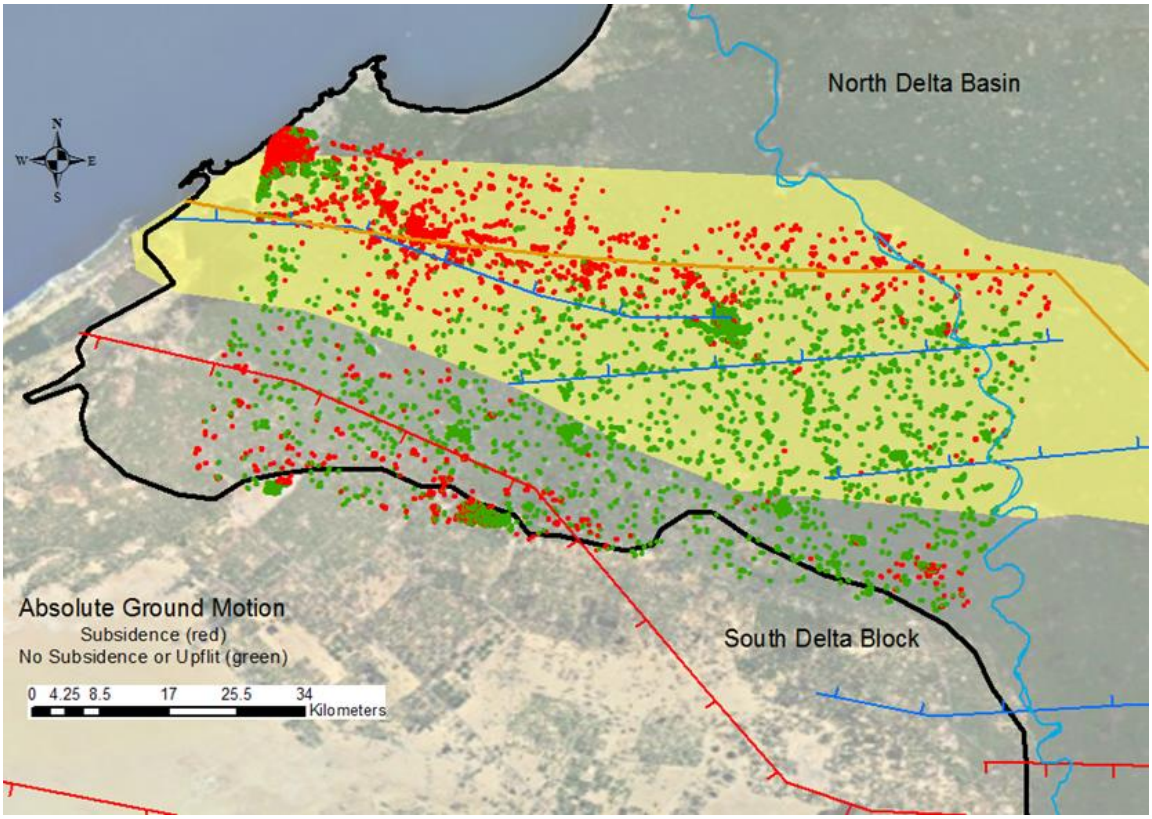

Figure 29: The Western Nile Delta: Positive and Negative Ground Motion
Ground motions are divided into two subsets: the PS points that are subsiding are shown in red and the PS points that are either stable or slightly uplifting are shown in green. Stable PS points are those that have no absolute vertical velocity. The maximum measureable uplift was 1-2 mm/year. Boundaries between subsidence and stability/uplift roughly follow the subsurface normal faults. Subsidence occurs on the hanging wall side of the normal fault where the thickness of Quaternary sediments was greatest. The data were processed using the StaMPS program.

It is hypothesized that ancient west-east trending normal faults created a horst and graben landscape that later filled in with variable-thickness deltaic sediment packages. The grabens are regions of greater accommodation space. This includes the entire North Delta Basin which is covered (filled) with thicker sediment packages than the horst areas.

The young, partially-unconsolidated Quaternary sediments naturally compact. Therefore, regions with thicker Quaternary sediments will compact more, and for a longer period of time, than regions with less Quaternary sediments. The flexure zone (which includes the hinge line and numerous blind, normal faults) and normal faults in the South Delta Block act as tectonic boundaries between these Quaternary sediment packages of various thicknesses. This results the spatial distribution of various subsidence rates delineated by ancient, inactive fault lines.

It is important to note that this region is composed of many blind normal faults, and the locations of these faults are highly debatable (Schlumberger, 1984; Sestini, 1989; Sestini, 1995; Aal et al., 2001; Dolson et al., 2001; Vandr et al., 2007; Bakarat, 2010). Two Sestini (1995) figures were compiled to establish a backdrop of regional subsidence rates (Figure 30). This was done to (1) the differentiate between the hinge line and the flexure zone and (2) recognize the large, west-east trending normal faults in the South Delta Block (although highly simplified, these faults form structures that are recognized and supported by subsurface geophysical exploration – Barakat, 2010).

Radar interferometry can be utilized to help define major normal fault locations. There are a few subsidence measurements in the western and central Nile Delta, for example, that do not follow the Sestini (1995) fault boundaries (Figures 28 & 29). The potential for redrawing major fault lines using radar interferometry (in the absence of lateral subsurface geophysical data) is evident. However, it must be done with caution, and the understanding that although fault line retracing has previously been performed (ESA et al., 2013), the lack of actual subsurface data could limit redrawn fault line

locations as only hypothetical. Normal fault retracing has been attempted with this major caveat and results do not deviate too much from previously published basement fault maps of the region (Figure 31).

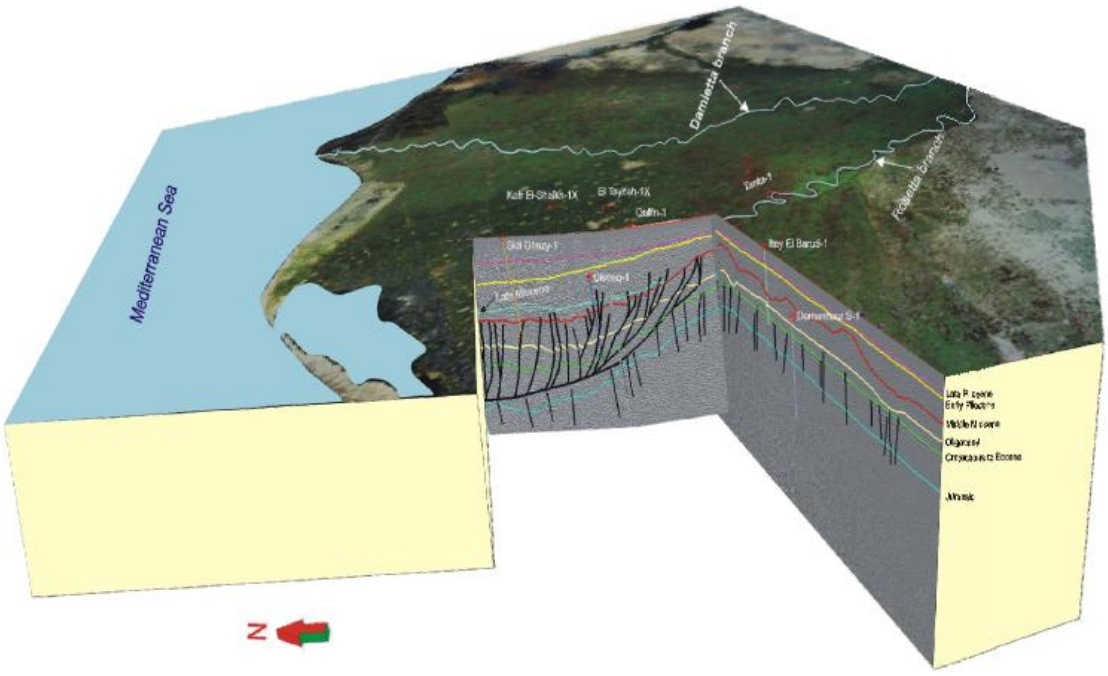

Figure 30: Subsurface Structural Model Created Using Seismic Reflection Data

A three-dimensional subsurface structural model created by Barakat (2010) utilizing Petrel software. This model displays both the complexity and density of subsurface, normal faults in the Nile Delta.

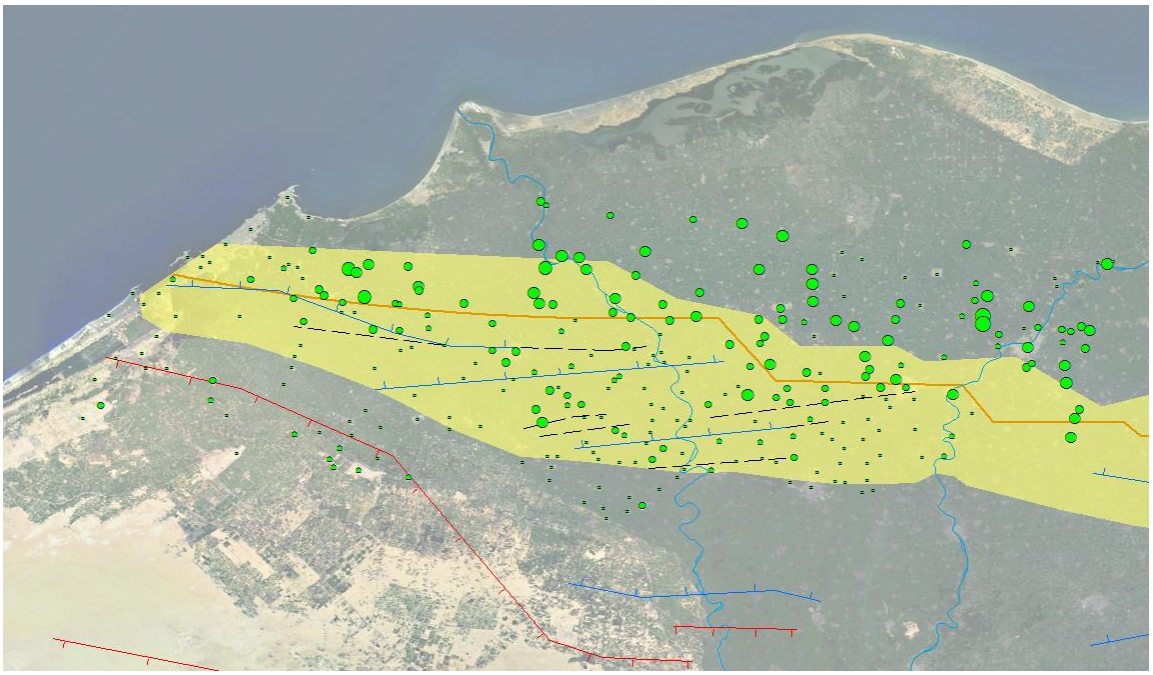

Figure 31: Fault Tracing using Radar Interferometry

An example of using radar interferometry results to trace possible normal fault locations (black dashed lines). No subsurface geophysical data (e.g., seismic lines) or GPS locations were available to assist in the interpretation.

Ground motion and subsidence rates appear less bounded by tectonic boundaries and more influenced by proximity to present-day Nile River meanders in the eastern portion of the Nile Delta. The highest subsidence rates measured (13 mm/year) occur within 5 kilometers of the Damietta River Branch (in the cities of Ras El Bar and Damietta). The lowest subsidence rates (<3 mm/year) occur at more distal locations. Although this region is almost entirely north of the hinge line, some cities along the Damietta River Branch south of the hinge line exhibit subsidence rates equal to or greater than cities farther north (downstream). This indicates that this region of the Nile Delta may be less influenced by ancient tectonic boundaries, and more influenced by recent sediment compaction or other anthropogenic factors. Also, tectonics may play less of a

role in this region because the North Delta Basin: (1) does not contain many large, normal faults, and (2) pre-Holocene sediment thickness is relatively constant (especially along the Damietta River Branch). Holocene sediment thickness, on the other hand, is highly spatially variable (Figure 32).

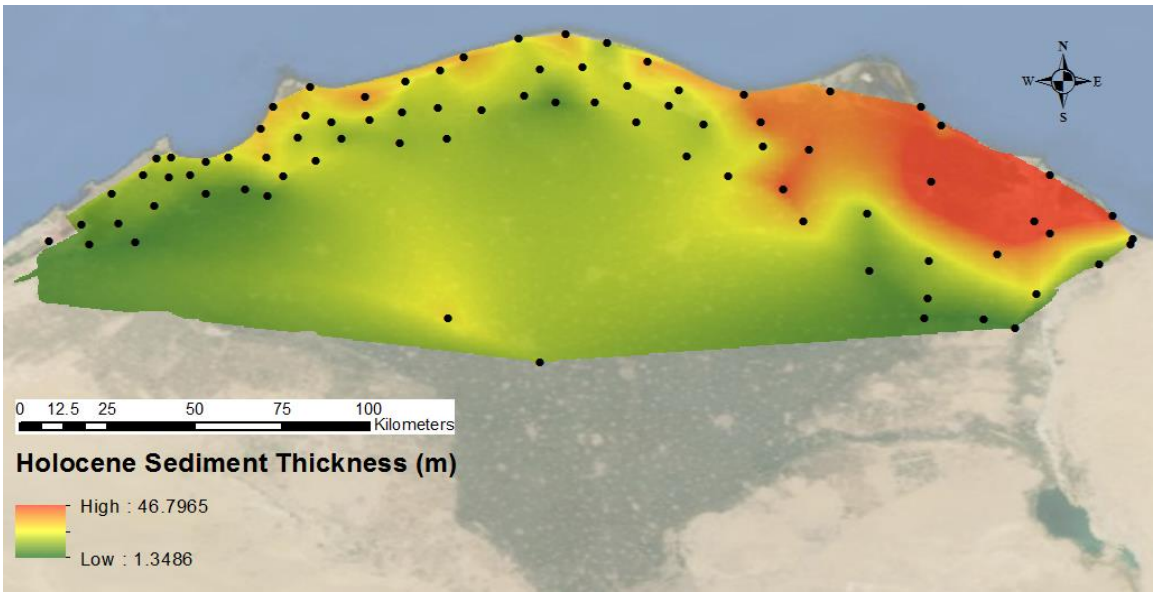

Figure 32: Holocene Sediment Thickness Across the Northern Nile Delta
Holocene sediment thickness (in meters), interpolated, using the natural neighbor interpolation method (Boissonnat & Cazals, 2001), from the 83 Smithsonian wells (black dots) that were drilled to the Holocene-Pleistocene boundary (Stanley et al., 1996).

The Damietta River Branch and Manzala Lagoon are areas of substantial Holocene sediment deposition. Clays, silts/muds, peat, and sands were all deposited during the last 12,000 years. Thick sections (up to 50 meters) of compactable Holocene sediments (along with partially-compacted Pleistocene sediments) have been considered to be the cause of the high subsidence rates observed in this area of the Nile Delta (Becker & Sultan, 2009). Results of this study appear to agree. Subsidence rates appear to be greatest near present-day river meanders or areas of recent sediment deposition.

Subsidence rates decrease along the Damietta River Branch to the south and near the Sinai Desert (both are regions of little to no Holocene sedimentation).

One reason for the high subsidence rates observed in the northeastern Nile Delta may be the fact that the Manzala Lagoon was a recent depocenter of sediment accumulation (< 3,500 years) (Becker & Sultan, 2009). Figure 33 shows the thickness of these Holocene sediments deposited within the last 3,500 years. Thicknesses range from 0 to 19.5 meters across the northern Nile Delta. Thickest Holocene sediment packages are

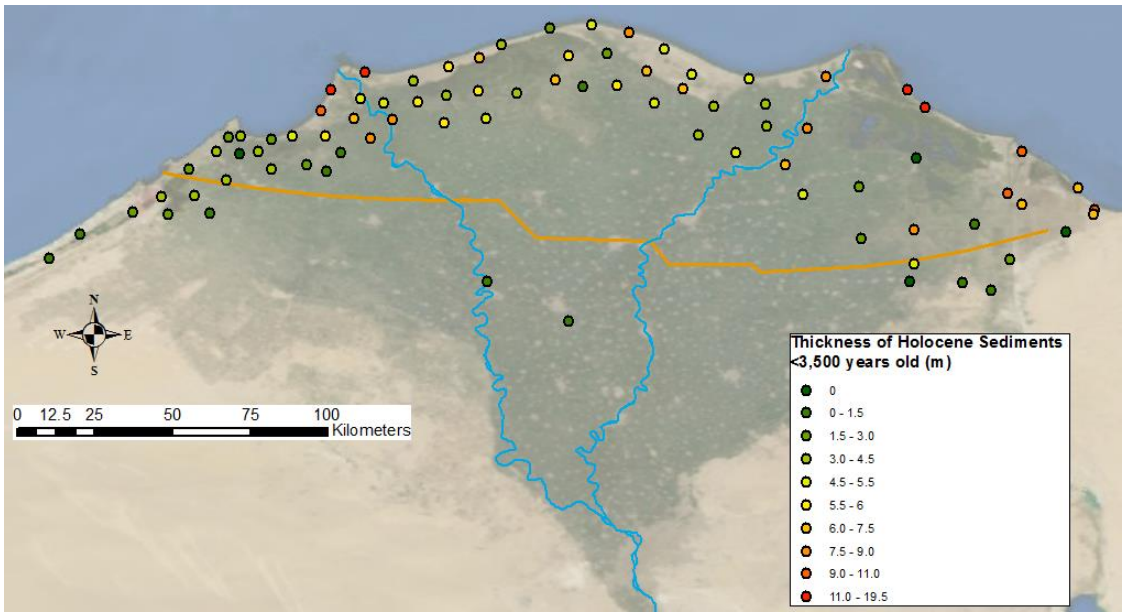

Figure 33: Thickness of Holocene Sediments <3,500 Years Old

Young Holocene sediments range in thickness from 0 to 19.5 meters. Thickest sediment packages are located around the mouths of the Rosetta and Damietta River Branches and north of the Manzala Lagoon.

Located along the two active branches of the Nile River (Damietta and Rosetta) where thicknesses range from 19.5 meters at the mouth of both rivers to 6.0 meters farther upstream. Holocene sediment thickness rapidly decreases away from the two river branches (with the exception of the Manzala Lagoon) as sediment thickness decreases to less than 3.0 meters south of the hinge line.

Summary

PSI results indicate that the study area within the Nile Delta may be divided into two broad categories based on observable subsidence regimes: (1) the western Nile Delta, where subsidence appears to be more spatially controlled by inactive fault boundaries and the magnitude of subsidence rates is directly proportional to natural sediment compaction, and (2) the eastern Nile Delta, where the subsidence appears to correlate well with the proximity to geologically recent and presently active depositional regions (e.g., proximal to the Damietta River Branch north of the city of Mansoura) and, once again, is directly proportional to natural sediment compaction. This broad division of the delta is based on natural factors controlling subsidence rates – such as tectonics, sediment thickness, sediment age, and compaction rates – but the use of radar interferometry yields the total subsidence at all measureable points. That is, subsidence rates via radar interferometry do not differentiate between controlling factors, whether they may be natural and/or anthropogenic. Further spatial analyses must be conducted in order to define additional potential man-made influences on subsidence rates. In a region such as the Nile Delta, where humans have basically been shaping the landscape for thousands of years, anthropogenic effects on subsidence rates are to be expected.

Anthropogenic Subsidence Factors in Urban Areas

Obtaining ground motion data over a relatively large area using PSI is a reliable first step when attempting to discuss the factors that influence motion. Unfortunately, because PSI is only usable over urban areas, it is difficult as how to discern these separate anthropogenic causes from natural factors if both possibly play a role in establishing subsidence rates. If one were able to obtain PS points in a desolate, vegetated region away from (but still proximal to) urbanized areas, one may argue that subsidence rates at these PS points are influenced only by natural factors and then compare them to anomalous values found in the nearby city. The assumption that all nearby cities are influenced by a similar magnitude of subsidence may be valid. However, because PSI can only be used in cities, there is no way to differentiate between anthropogenic and natural factors. Measured subsidence rates are therefore a *combination* of all factors, and without additional datasets (e.g., groundwater extraction rates, structural loading of man-made features on partially-unconsolidated sediments), it is impossible to separate subsidence rates into categories without making further assumptions.

So let us assume the following argument: the only natural factor controlling vertical subsidence rates is the compaction of young deltaic sediments. All other potential factors are due to anthropogenic factors such as: (1) subsurface resource extraction of groundwater, natural gas, oil, et cetera, (2) the increased use of water for irrigation purposes, and (3) increased compaction due to urban loading. This assumption may actually prove rather reasonable. There is no direct evidence for recent tectonics influencing subsidence rates, and excluding coastal regions of the delta that are

undergoing high rates of erosion, the rise in sea level does not directly affect a majority of the Nile Delta. The anthropogenic influence on subsidence in the Nile Delta may be estimated by examining the compaction model results from previous studies (Stanley, 1990). Total subsidence may be divided into two parts:

$$TS = NS + AS \qquad \text{(Eq. 8)}$$

where the total subsidence (TS) is the unbiased subsidence value obtained via radar interferometry. The natural subsidence (NS) is the subsidence rate due to compaction and anthropogenic subsidence (AS) is the combination of all the additional man-made influences on the subsidence rates. Simply solving for AS from Equation 8:

$$AS = TS - NS \qquad \text{(Eq. 9)}$$

NS values depend on the natural compaction rates of sediments found in the Nile Delta. Complete Holocene lithological logs across the northern Nile Delta were created from eighty-seven wells drilled and analyzed between 1985 and 1994 as part of the Smithsonian Mediterranean Basin Program (Stanley et al., 1996). Eighty-three of the eighty-seven wells reached deep enough to penetrate the Holocene-Pleistocene boundary (most wells do not reach depths much greater than the Holocene-Pleistocene boundary, which appears to have been the target depth – see Figure 32). Four types of sediments were observed in these logs: (1) sand, (2) clay, (3) silt/mud, and (4) peat. These detailed lithologic logs denote sediment package thicknesses to the nearest 0.1 meters in each well. Therefore, total column thickness of each sediment type deposited in the Holocene may be calculated (Figure 34).

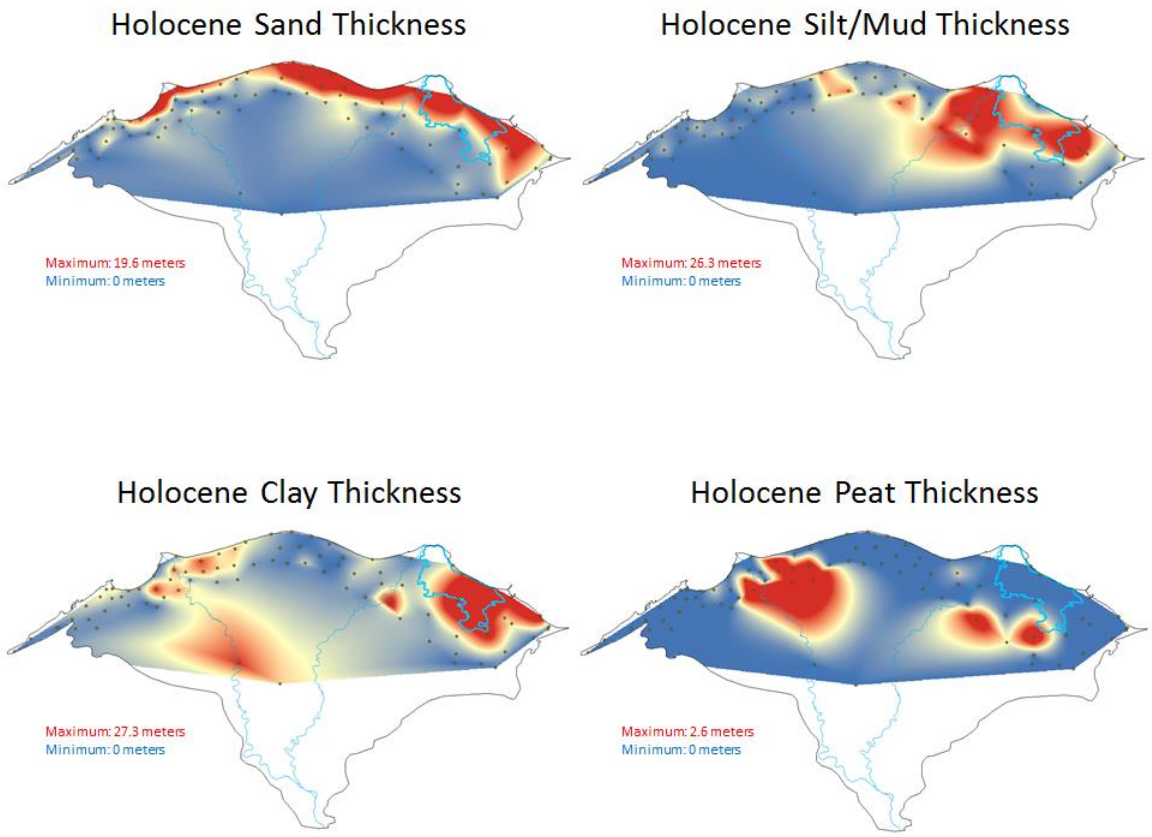

Figure 34: Thickness of Holocene Sand, Silt/Mud, Clay, and Peat

Total Holocene thickness of each of the four sediment types (sand, silt/mud, clay, and peat across) the Nile Delta. Each sediment thickness map is interpolated using the natural neighbor interpolation method.

Natural compaction rates are dependent on lithology and burial depth (thickness reduction), so total porosity (φ) values were obtained (Table 5 – Yu et al., 1993). The weighted total porosity (φ') describes the overall porosity within each well weighted based on sediment thickness. The idealized pore space (Hφ') is equal to the product of the weighted total porosity and the depth to the Holocene-Pleistocene boundary (H); Hφ' quantifies the maximum vertical compaction available in meters (Figure 35).

Table 5: Sediment Porosity of Sand, Clay, Silt/Mud, and Peat (Yu et al., 1993)

Sediment Type	**Total Porosity (φ)**
Sand	0.41
Clay	0.42
Silt/Mud	0.45
Peat	0.80

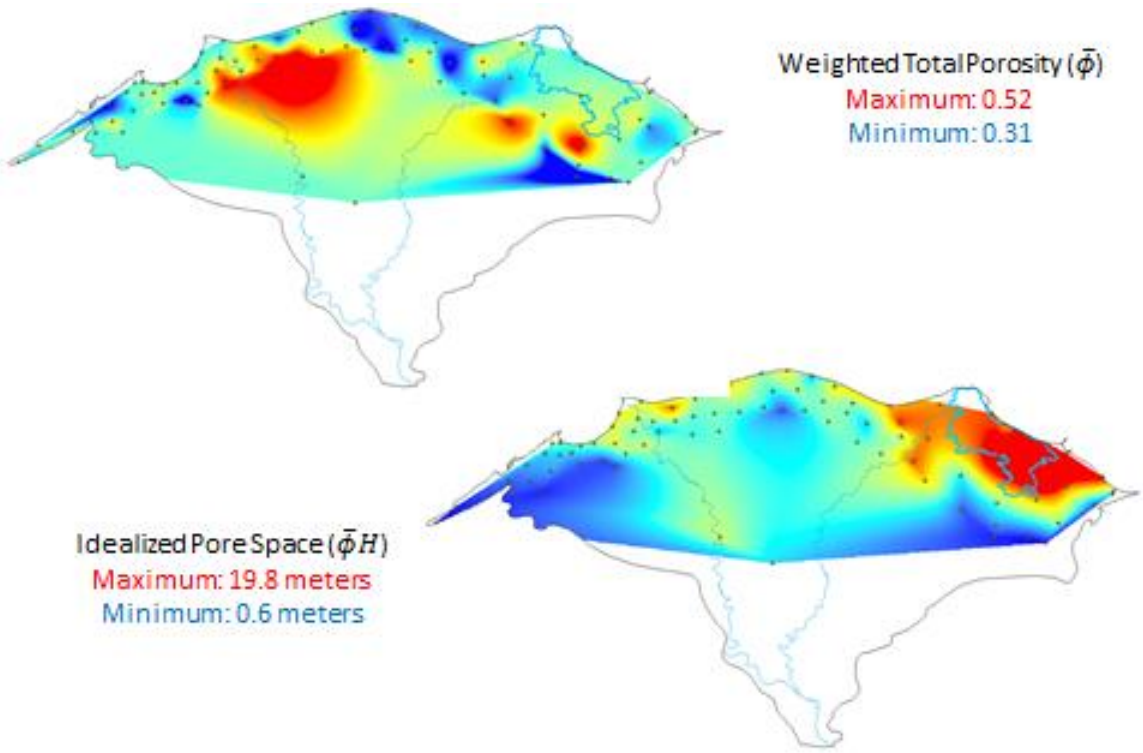

Figure 35: Weighted Total Porosity and Idealized Pore Space Across the Northern Nile Delta

Top: weighted total porosity interpolated (natural neighbor interpolation method) across the Nile Delta; $\bar{\phi}$ range from 0.31 (dark blue) to 0.52 (red). Bottom: idealized pore space interpolation; $\bar{\phi}H$ range from 0.6 meters (dark blue) to 19.8 meters of maximum vertical compaction potential.

The northeastern Nile Delta, as shown in Figure 34, contains thick packages of Holocene sediment. Maximum thickness of sand, silt/mud, and clay all occur within the Manzala Lagoon or along the Damietta River Branch. The idealized pore space (Figure 35) illustrates the maximum columnar thickness of pore space present in the Holocene sediment layer and closely resembles the total Holocene sediment thickness (Figure 33) across the Nile Delta. All of these images show the sediment basin or depocenter (over the last 3,500 years) surrounding the Manzala Lagoon.

Available data present a handful of limitations:

1. The distribution of Smithsonian wells to cities within 30-50 kilometers of the Mediterranean coast limits the compaction estimation area. Sediment thicknesses must be interpolated between wells.
2. Eighty-three of these Smithsonian wells reach the Holocene-Pleistocene boundary. Therefore, only subsidence rates due to the compaction of Holocene sediments may be estimated. Subsidence rates in the northeastern Nile Delta are mainly controlled by recent Holocene compaction, so, compaction estimations only make sense if performed in the northeastern Nile Delta, mainly along the Damietta River Branch (distribution area of Smithsonian wells).
3. Actual subsidence rates due only to compaction are not known. Stanley & Warne (1993) created a model estimating subsidence rates across the Nile Delta margin. They estimated subsidence rates ranging from 0 mm/year to >4 mm/year. The following assumptions are used for this study: (1) Idealized

pore space is directly proportional to subsidence rates, ranging from 0 mm/year to 4.5 mm/year (based on Stanley & Warne, 1993). (2) Natural subsidence rates may be approximated along the Damietta River Branch and around Manzala Lagoon. (3) Residual subsidence may be calculated by subtracting the NS estimated values from the subsidence rates obtained via radar interferometry (Figure 36). This residual subsidence is equivalent to AS and estimates the man-made influences on deltaic subsidence.

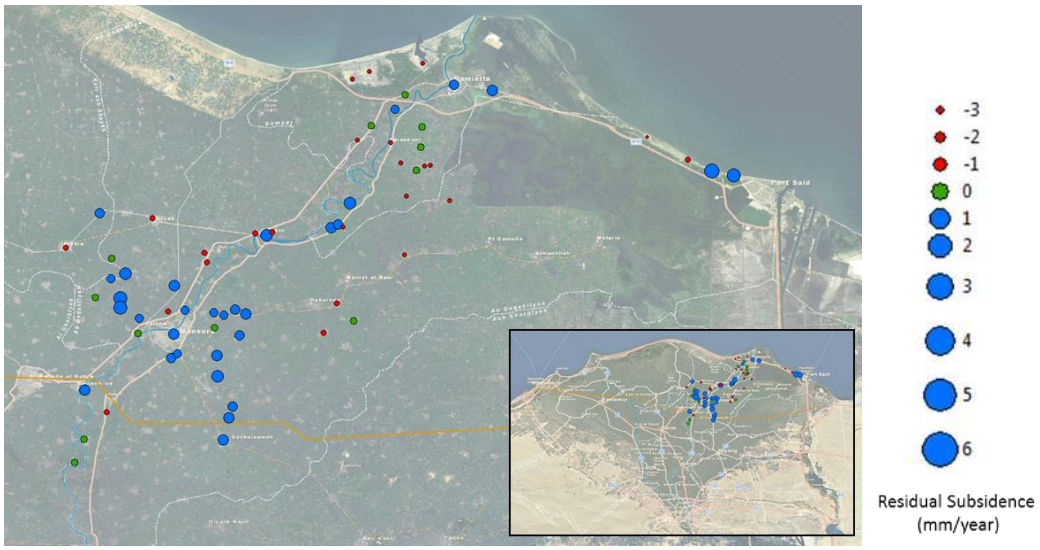

Figure 36: Residual Subsidence (mm/year) for Urban Centers Around the Manzala Lagoon and Damietta River Branch

Positive residual subsidence value (blue dots) indicate a lower measured subsidence rate (from radar interferometry) than the compaction model predicts. This may indicate anthropogenic influences on subsidence rates. Negative residual subsidence values (red dots) indicate a higher measured subsidence than the compaction model predicts, which may indicate an underestimation of the compaction model. Zero residual subsidence values (green dots) are locations where measured subsidence rates equal modeled compaction rates.

Any pure remote sensing approach cannot precisely differentiate between factors influencing ground motion without incorporating field observations and third-party datasets. Also, any regional approach, on its own, is unrealistic for defining anthropogenic influences on subsidence rates. Instead any ground motion investigated must be done on a city-by-city basis. This is because human-made effects in one city may have no effect on ground motion in a neighboring city. Anthropogenic factors that may potentially contribute to increased subsidence rates both must be understood and quantitatively accounted for on all geographic scales.

Subsurface resource extraction has been a documented cause of increased local subsidence (Foster & Chilton, 2003); Zekster et al., 2005). Common, wide-spread extracted resources include groundwater, oil, natural gas, rocks or sediments, and metallic or non-metallic minerals. In the Nile Delta, specifically the North Delta Basin, the most highly extracted resources are groundwater and natural gas.

Groundwater Extraction or Ablation

The Nile Delta is heavily populated. Approximately 50 million people permanently live in the delta (refer to Chapter 3). The land surface of the Nile Delta has also been heavily altered, from barren land to residential, agricultural, or industrial land. High population density yields logistical difficulties for the government and for industry when trying to provide an acceptable quality of life. One of the most important issues is water demand. The problem of providing enough water for the domestic and industrial demand usually results in the extraction (ablation) of groundwater.

Ninety-six percent of water usage in Egypt comes from the Nile River via upstream sources (the Nasser reservoir behind the Aswan High Dam in southern Egypt) or from rainwater (Rayan & Djebedjian, 2005).

Groundwater accounts for the remaining four percent. The groundwater systems in Egypt may be divided into six major aquifers. Two of these aquifers are present in the subsurface of the Nile Delta: (1) the Coastal Aquifer and (2) the Nile Aquifer (Figure 37). During the mid-1990s, Yakoub (1996) calculated the groundwater pumping potential for each aquifer at specified locations. Groundwater potential from the Nile Aquifer within the confines of the Nile Delta was approximately 1,956 million cubic meters per year. Maximum potential from the Coastal Aquifer maxed out at approximately 1 million cubic meters per year. Recently, due to over-extraction of fresh groundwater, the Coastal Aquifer has become more saline (Stanley & Warne, 1993).

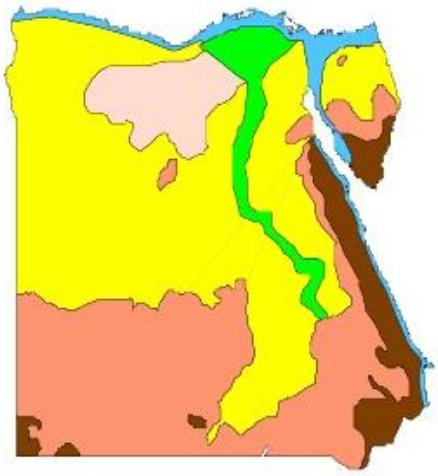

Figure 37: The Six Major Aquifers in Egypt

They are: (1) Coastal Aquifer (light blue), (2) Nile Aquifer (light green), (3) Moghra Aquifer (pink), (4) Karstified Carbonate Aquifer (yellow), (5) Nubian Sandstone Aquifer (peach), and (6) Fractured Rocks Aquifer (brown). (Image taken from Attia, 1999)

The Nile Delta also receives approximately 380 million cubic meters of rainfall. This also supplement irrigation needs (Ibrahim et al., 1994).

To understand current requirements and future potential for groundwater extraction, an assessment of the spatial distribution of the water demand is important. Figure 38 illustrates water demand (domestic and industrial combined – excluding agricultural usage) in the governorates of Egypt. The highest concentration of water demand is found in the Nile Delta, where the minimum domestic and industrial volume of water demand is approximately 100 million cubic meters per year per governorates. There is much evidence of over-pumping of groundwater in the Nile Delta (refer to Figure 21). Stanley and Warne (1993) created a prediction model for saline sea water intrusion into the Coastal and Nile Aquifers by the year 2050 (assuming pumping rates trend the same as the early 1990s). Figure 39 shows the distribution of subsidence rates superimposed on the annual domestic and industrial water demand by governorate, from Figure 39. Figure 40 shows the general trend of groundwater extraction rates observed in 1992, which is that extraction rates increase southward, for many reasons: (1) the largest city in Egypt (Cairo) is located at the southern tip of the Nile Delta, (2) the delta transitions to more arid regions toward the south and the only source of water is groundwater, and (3) rainfall amounts decrease away from the Mediterranean Sea.

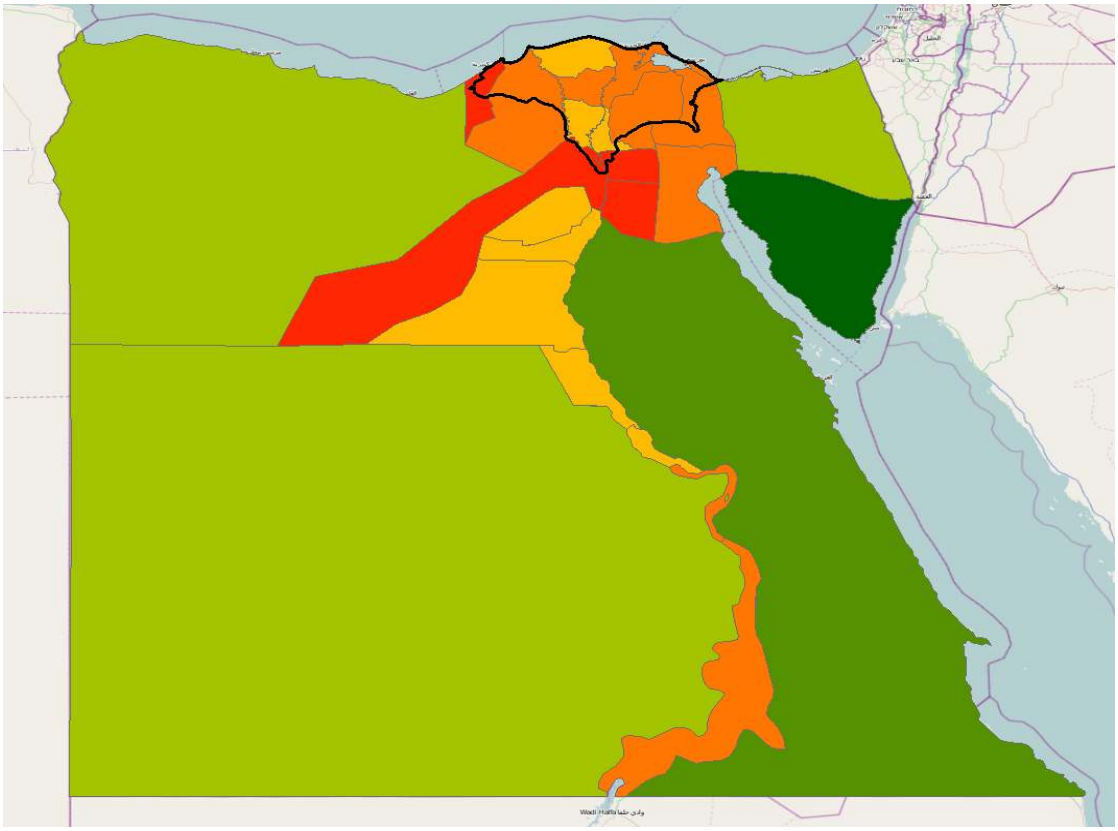

Figure 38: Annual Domestic and Industrial Water Demand by Governorate

Annual water demand is separated by governorate in a semi-logarithmic scale (million cubic meters per year): dark green (<1), green (1-10), lime green (10-30), yellow (30-100) (does not appear on this map), light orange (100-300), orange (300-1,000), and red (>1,000). The Nile Delta is outlined in black. (Image created from data taken from Rayan & Djebedjian, 2005)

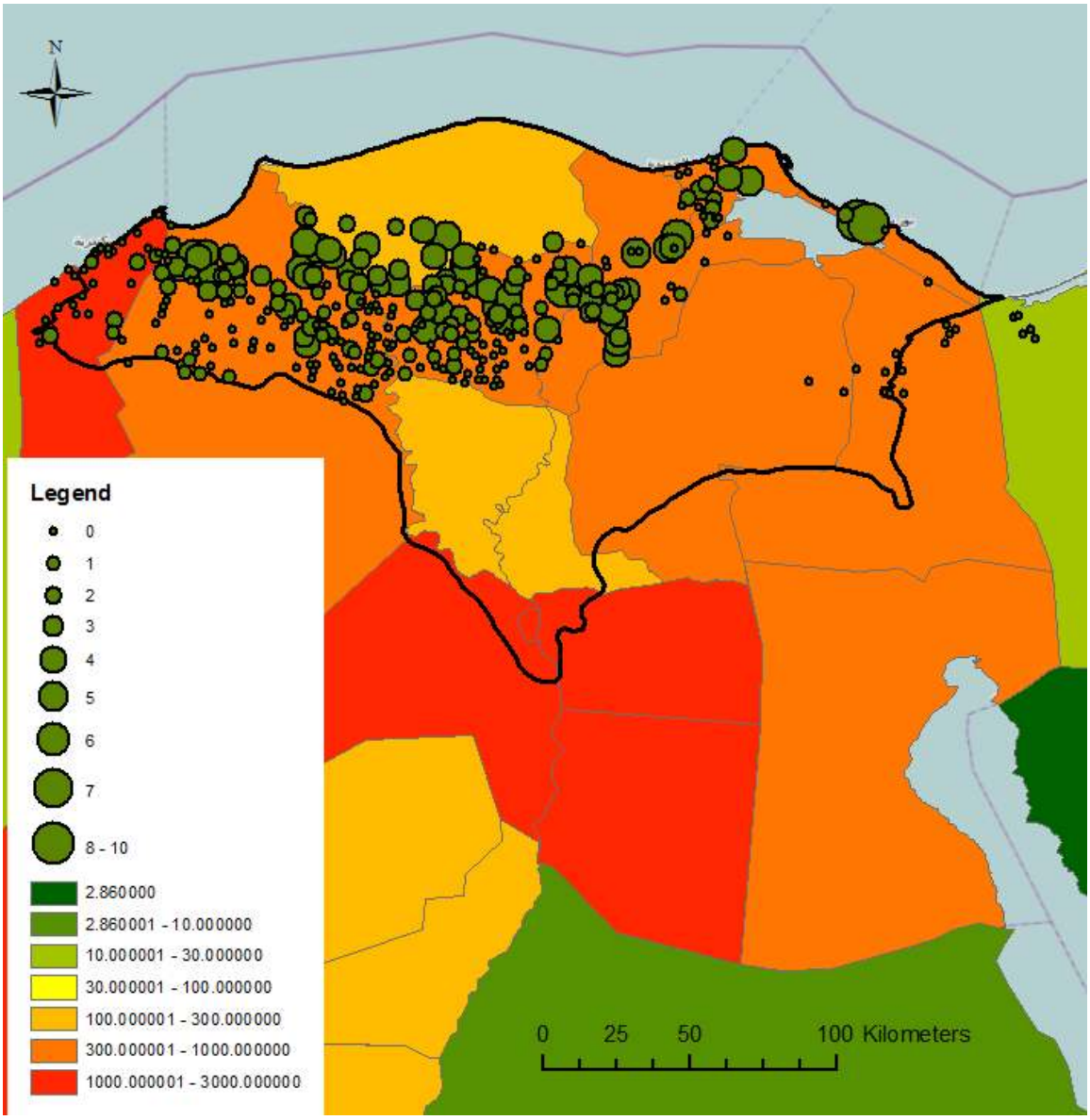

Figure 39: Subsidence Rates and Water Demand

The subsidence rates measured across the Nile Delta (using PSI) are shown as green circles and measured in mm/year. The water demand, are shown in units of millions of cubic meters per year – dark green (<1), green (1-10), lime green (10-30), yellow (30-100) (does not appear on this map), light orange (100-300), orange (300-1,000), and red (>1,000) – and are separated by governorate.

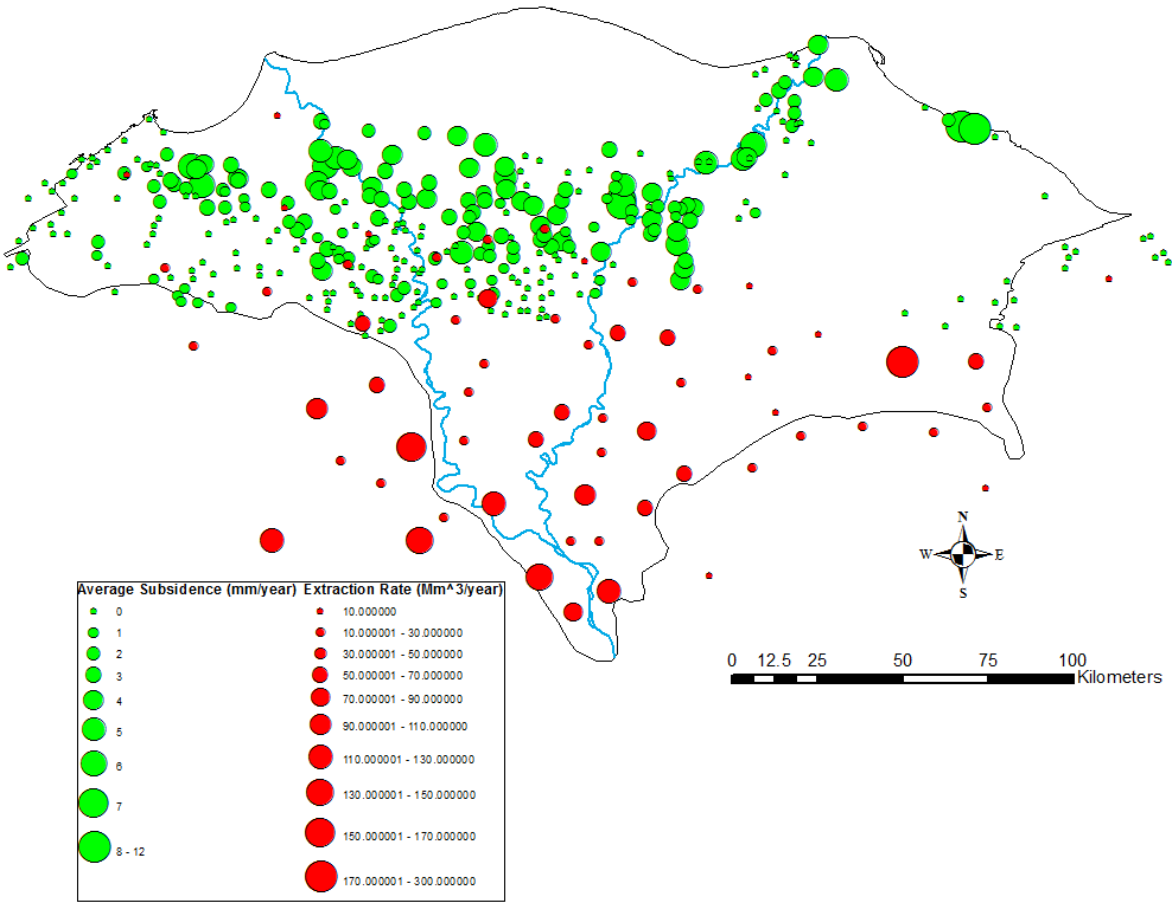

Figure 40: Average Subsidence and Groundwater Extraction Rates

Average subsidence rates (mm/year) compared to groundwater extraction rates (million cubic meters per year) calculated across and around the Nile Delta (outline). Groundwater extraction rates taken from RIGW, et al. (1992). Although this figure shows no extraction locations in the northern delta, the original map shows extraction rates approaching nill as one approaches the Mediterranean coastline.

Another indirect indication of high amounts of groundwater pumping may be observed when the piezometric head of groundwater levels is calculated. The piezometric head relates to hydrostatic pressure. A model of the piezometric head was created over the western Nile Delta by Dawoud et al. (2005) based on remote sensing observations (Figure 41). The first noticeable feature on the western delta piezometric map is the large positive groundwater surface anomaly (up to 11 meters) in the northwest region. This anomaly is quite high and is also fairly abrupt (tight contour lines on all sides of the anomaly). This entire positive anomalous section covers many large cities, including Alexandria (population: 4,030,582), Karf El-Dawar (population: 114,030), and Damanhour (population: 244,043) (UNSD, 2013) and illustrates the impact of groundwater pumping compared to the 'background' groundwater surface in the surrounding regions. The negative anomalies in the north surround lagoons and the negative westerly gradient in the south points towards the Western Desert.

Combining the data shown in Figures 21 and 37-42, there appears to be little correlation, on a regional scale, between average subsidence rates and groundwater extraction rates, although there is concrete evidence that over-extraction is occurring in the Nile Delta.

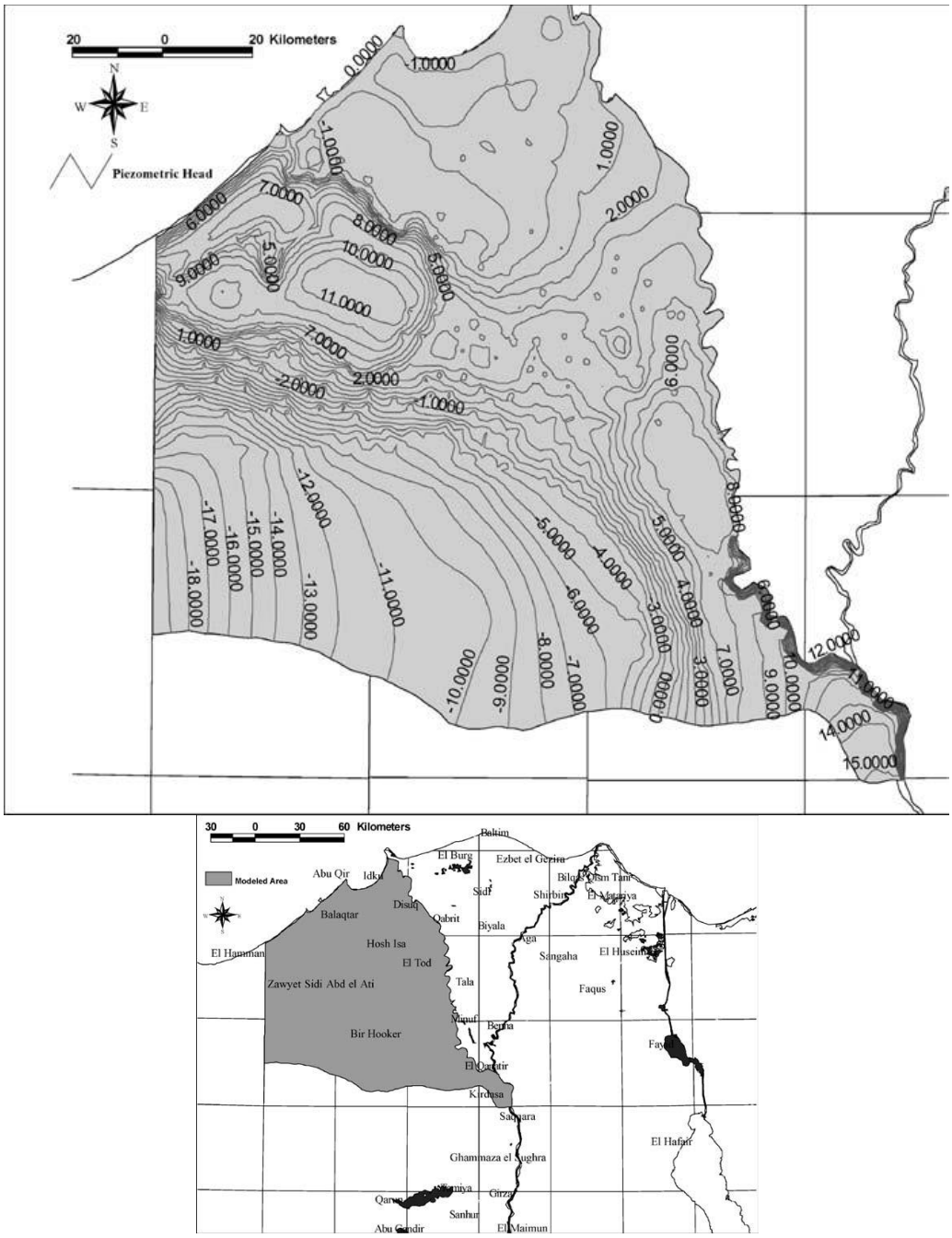

Figure 41: Piezometric Head Model in Western Nile Delta

(3) The piezometric head modeled over the western Nile Delta using GIS-based groundwater datasets; (B) Location of the study area in the Nile Delta, Egypt. Images from Dawoud et al. (2005).

Hydrocarbons: Natural Gas

Subsurface energy exploration in the Nile Delta began in 1947 when Standard Oil Company of Egypt (SOE) began carrying out large-scale gravity profile reconnaissance. Standard discovered large gravity minimums near the city of Tanta (located between the Damietta and Rosetta branches of the River Nile in north-central Egypt – Barakat, 2010). Serious exploration began in the early 1960s, where many onshore gravity lows were discovered and confirmed to be natural gas plays. Oil and natural gas production significantly increased as hydrocarbon detection and extraction techniques became more advanced during the late twentieth century. This was especially true for the offshore Nile Delta sedimentary deposits.

RWE Dea, a German-based oil and gas exploration company, took over all subsurface energy exploration in Egypt in 1999. Natural gas exploration began to increase in the Nile Delta. Cumulative gas reserves in the delta doubled between 1997 and 2005 (Figure 42). RWE Dea currently holds 11 concessions totaling 6,500 square kilometers (onshore and offshore) throughout northern Egypt (Figure 43). Nearly all the onshore subsurface energy exploration has occurred in the north-central Nile Delta, between the Damietta and Rosetta branches. Since 2005, RWE Dea has made five more natural gas discoveries within the Nile Delta (Barakat, 2010).

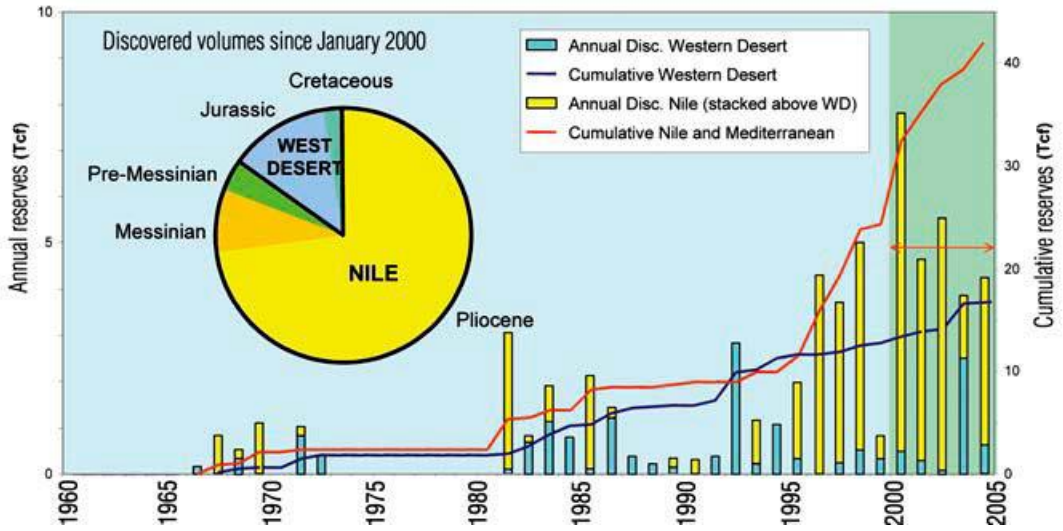

Figure 42: Annual and Cumulative Natural Gas Reserves in the Nile Delta and Western Desert of Egypt from 1960 to 2005

A substantial increase in the discovery of natural gas reserves in Egypt began in 1999 when RWE Dea took over all subsurface energy exploration (green background on bar graph). (Image from Abdel Aziz & Shann, 2005)

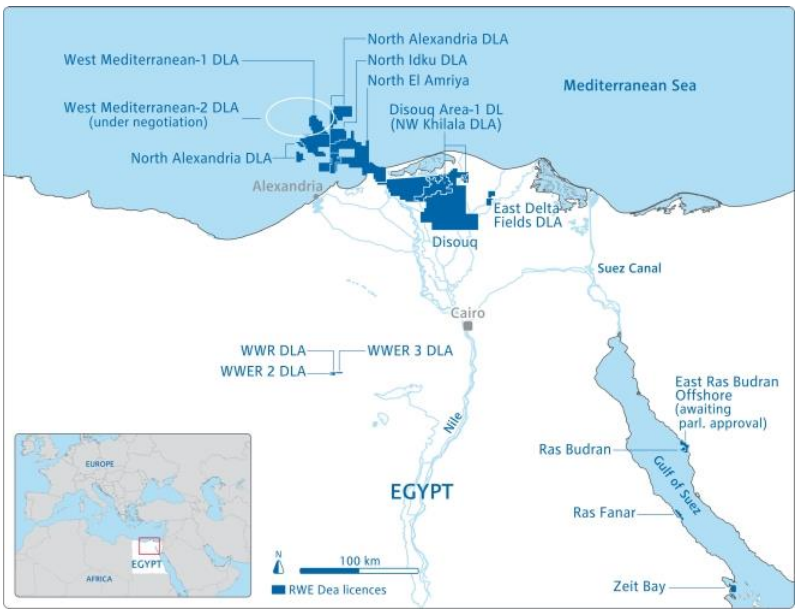

Figure 43: Current RWE Dea Licenses in Egypt (RWE Dea, 2013)

The areas of licensure owned by RWE Dea within the Nile Delta (Figure 43) do appear to overlap areas of high subsidence within the North Delta Block between the Damietta River Branch and the Rosetta River Branch. Whether these high subsidence rates are due in part to the extraction of natural gas, however, is difficult to say. Much more data (e.g., extraction rates, exact locations of natural gas plays) are required to confidently correlate (or show no correlation) measured subsidence rates to natural gas extraction. Additionally, PSI processing over the full area of natural gas extraction sites would be beneficial to see if there are high rates of subsidence across the RWE Dea license region. The data do not suggest any strong correlation.

Error Analysis

It is important to note the potential for errors, both random and systematic, when using radar interferometry. Random errors have measurement errors that lead to inconsistent results. They are unpredictable and uncontrollably fluctuate. Systematic errors are those that are predictable, may be taken into account, and eliminated if fully understood. Random errors have a null expected value, and hopefully, range close to the true value. Therefore, the summation of many random error values may cancel out. Systematic errors do not cancel out, as the summation of systematic errors would introduce even greater error.

Four potential causes of error are described below. The first describes random error due to the piecewise approach used when combining PSI results of multiple cropped regions in the Nile Delta.

The next three are systematic errors. Two of these error types are addressed by the interferometric stacking programs (SARscape and StaMPS) which attempt to eliminate these errors during the processing steps (atmospheric effects and long-wavelength errors).

The third systematic error is represented as a list of all of the assumptions used in this study, and the inherent errors that may arise from these assumptions.

The Piecewise Approach

The piecewise approach, described in Chapter 2, was required, in the absence of GPS stations, in order to create a subsidence rate map of the entire Nile Delta. Data from only one GPS station which is located in Alexandria, Egypt (active from 2002 to 2008) were available for the purposes of this study. The lack of additional GPS stations, and the consequential utilization of the piecewise approach, introduces a sub-millimeter/year averaging error. After the velocities between two groups of PS points are calculated from two cropped regions, where an overlapping area is common between one region of absolute velocities (e.g., the region with the known GPS station) and another region of relative velocities, the differences between all overlapping PS points are calculated and an *average velocity shift* is applied to the relative-velocity region. It is necessary to limit the averaging error, and for this reason, a velocity shift is only applied when the root-mean square (RMS) error is less than 0.5 mm/year. When the RMS error is greater than that value, the relative-velocity region is re-cropped and reprocessed to obtain different PS point locations with the desired RMS error.

The potential for error accumulation is one major concern with the piecewise approach. Every time the average velocity shift is performed, an RMS error is introduced. Therefore, the potential for error accumulation is directly proportional to the distance from the one known GPS station. The optimal solution to this problem would be the emplacement of a dense GPS network that would allow for no average velocity shifts. Every cropped region would ideally have an absolute reference point. Put simply, the more GPS stations (absolute reference points) the less potential RMS error is carried through the calculations. Unfortunately, for the purposes of this study, the lack of available GPS stations in the Nile Delta is the major limitation. Private, continuous GPS stations are known to exist; however, these data are currently unavailable. Refinement of the subsidence rates presented here would be possible if these data become available.

Atmospheric Effects

Chapter 3 describes the effects of the atmosphere on radar waves. Water vapor reduces the velocity of radar waves. Humidity and water vapor by itself does not cause problems for radar interferometric techniques. Instead, it is a variable (active) atmosphere across a processed region that is much more detrimental. Because PSI calculates the relative velocities of PS points within a cropped region, if the atmosphere exhibited a constant water vapor column across the entire cropped region, then the atmospheric effects on all transmitted/received radar waves would be constant. Trouble surfaces when the water vapor column varies across the cropped region, because then, deceleration of radar waves also varies. PS points beneath a relatively thick water vapor column, as a

result, would appear to be farther away from the satellite than PS points beneath a thinner water vapor column. This results in a greater false subsidence rate for the prior points with respect to the latter points.

Processed regions were cropped to relatively small areas to avoid atmospheric effects, and to lessen lateral atmospheric variability. Areas were restricted, if possible, to less than 100 square kilometers (the sparseness of large cities in the Nile Delta sometimes required the cropping/processing of larger regions, up to 400 square kilometers). This assumes that atmospheric variability occurs on a scale larger than the area of the cropped region. The smaller the area of each cropped region, the greater the number of regions required to process the delta, and that means an increase in the number of times the average velocity shift must be performed in the piecewise approach. This results in an increase in potential RMS error. This is a necessary compromise. The random error introduced via the piecewise approach is on a sub-millimeter/year scale, and therefore, it may cancel out. This is more acceptable than systematic error which is introduced via atmospheric effects, and can reach a centimeter/year scale (Zebkar et al., 1997). This error does not cancel out.

Long-Wavelength Errors

Long-wavelength errors are errors that occur on a large scale (hundreds of kilometers) across large scenes. Factors that cause long-wavelength errors include gradual atmospheric changes (such as a gradual temperature and/or pressure gradient) or the curvature of the earth (a geometric error). Long-wavelength errors are one-

dimensional errors which may occur in either the range and/or the azimuth direction. Long-wavelength errors attributable to gradual atmospheric gradients are eliminated using atmospheric filters in the processing programs. Geometric error due to the curvature of the earth (approximately 20 centimeters/kilometer) is easily negated with the use of a Digital Elevation Model (DEM) during the interferogram generation steps.

Potential Errors due to Assumptions

All assumptions have errors. Assumptions are educated guesses or hypotheses created to fill in gaps in observable data and, more likely than not, are not entirely correct. The quantification of errors due to assumptions is difficult. Therefore, instead of assigning assumed error bars to these assumptions, a complete list of every assumption made during the course of this study is listed below:

1. Any filtering or noise reduction involves a basic assumption. Certain data contain "signal" and must be included, while other data contain "noise" and must be excluded. The processing steps for both software (SARscape and StaMPS) are discussed in Chapter 2.
2. Atmospheric variability, the largest source of error for radar interferometric techniques, is assumed to have a negligible lateral gradient over small regions (usually less than 25 km by 25 km). Also, when PSI processing required larger areas, the high- and low-pass atmospheric filtering adequately dealt with potential atmospheric anomalies.

3. Averaging errors due to the piecewise approach are always less than 0.5 mm/year.
4. Factors influencing subsidence rates may be divided into two categories: (1) natural factors, and (2) anthropogenic factors. Subsidence due to natural sediment compaction is assumed to be the only natural factor. Anthropogenic factors are indistinguishable from each other when using radar interferometry.

Conclusions

Subsidence rates vary widely across the Nile Delta, from no subsidence or slight uplift in the southwestern region south of the hinge line to 13 mm/year in the cities of Ras El Bar and Damietta in the northeastern delta. The Nile Delta may be subdivided into two subsidence regimes: (1) the North Delta Basin, where high average subsidence rates (as much as 10 mm/year) are in regions of relatively thick, unconsolidated Holocene sediments, and (2) the South Delta Block, a relatively stable region where average subsidence rates vary, but are much lower (ranging from 0 mm/year to as much as 6 mm/year) and are bounded by inactive, subsurface faults within the flexure zone.

Radar interferometry is a viable tool to measure large-scale, regional ground deformations. There are some technical difficulties in some areas of the world such as the Nile Delta. Additional datasets make use of techniques, such as PSI, much easier and effective. These datasets include: (1) water vapor column data from the Medium Resolution Imaging Spectrometer (MERIS) which lessens effects of a variable atmosphere; (2) additional ground GPS stations across the delta which would allow for less error due to velocity averaging when calibrating relative velocities to absolute

velocities; (3) public and private datasets that include information about anthropogenic influences on that natural environment (such as groundwater, oil, and natural gas extraction; sediment deposition and accumulation rates across the delta; land use maps; qualitative observations and witness accounts of ground motions). All these datasets would guide future efforts in attempting better assess anomalously high subsidence rates.

REFERENCES

Aal., A., El Barkooky, A., Gerrits, M., Meyer, H. J., Schwander, M., & Zaki, H. (2001). Tectonic evolution of the Eastern Mediterranean Basin and its significance for the hydrocarbon prospectivity of the Nile delta deep-water area. *Geo Arabia*. 6, 363-384.

Abdel Aziz, H. & Shann, M. (2005). Egypt: Gas discoveries since 2000-continued, consistent success. *The Leading Edge*. 3, 242-244.

Abdel-Moati, M. A. R. & El-Sammak, A. A. (1997). Man-made impact on the geochemistry of the Nile delta lakes – A study of metals concentrations in sediments. *Water, Air, and Soil Pollution*. 97, 413-429.

Ahmed, R., Siqueira, P., Hensley, S., Chapman, B., & Bergen, K. (2011). A survey of temporal decorrelation from spaceborne L-Band repeat-pass InSAR. *Remote Sensing of Environment*. 115(11), 2887-2896.

Aly, M. H., Klein, A. G., Zebkar, H. A., & Giardino, J. R. (2012). Land subsidence in the Nile Delta of Egypt observed by persistent scatterer interferometry. *Remote Sensing Letters*. 3(7), 621-630.

Aly, M. H., Zebkar, H. A., Giardino, J. R., & Klein, A. G. (2009). Permanent Scatterer investigation of land subsidence in Greater Cairo, Egypt. *Geophysical Journal International*. 178(3), 1238-1245.

Askne, J. I. H., Dammert, P. B. G., & Smith, G. (1999). Understanding ERS InSAR coherence of boreal forests. *Geoscience and Remote Sensing Symposium, 1999*. 28 June 1999 – 02 July 1999. 4, 2111-2114.

Askne, J. I. H., Dammert, P. B. G., Ulander, L. M. H., & Smith G. (1997). C-Band Repeat-Pass Interferometric SAR Observations of the Forest. *IEEE Transactions on Geoscience and Remote Sensing*. 35(1), 25-35.

Attia, F. A. R. (1999). Role of Groundwater in Egypt Economic Development. *Seventh Nile 2002 Conference*. 15-19 March, Cairo, Egypt.

Bakr, N., Weindorf, D. C., Bahnassy, M. H., Marei, S. M., & El-Badawi, M. M. (2010). Monitoring land cover changes in a newly reclaimed area of Egypt using multi-temporal Landsat data. *Applied Geography*. 30, 592-605.

Bamler, R. & Hartl, P. (1998). Synthetic aperture radar interferometry. *Inverse Problems*. 14, R1-R54.

Barakat, M. K. A. (2010). Modern Geophysical Techniques for Constructing a 3D Geological Model on the Nile Delta, Egypt. Dissertation at the Technical University of Berlin. 158 pages.

Bartmettler, A., Pasquali, P., Small, D., & Nüesch, D. (1996). Cross-Compatibility of ERS-SLC Products. *FRINGE '96 Workshop: ERS SAR Interferometry*. 30 September 1996 – 2 October 1996.

Bayer, T., Winter, R., & Schreier, G. (1991). Terrain Influences in SAR Backscatter and Attempts to their Correction. *IEEE Transactions on Geosciences and Remote Sensing*. 29(3), 451-462.

Becker, R. H. & Sultan, M. (2009). Land subsidence in the Nile Delta: inferences from radar interferometry. *The Holocene*. 19(6), 949-954.

Boissonnat, J.-D. & Cazals, F. (2001). Natural neighbor coordinates of points on a surface. *Computational Geometry*. 19, 155-173.

Bürgmann, R., Hilley, G., Ferretti, A., & Novali, F. (2006). Resolving vertical tectonics in the San Francisco Bay Area from permanent scatterer InSAR and GPS analysis. *Geology*. 34(3), 221-224. doi: 10.1130/G22064.1.

Calafat, F. M. & Jordà, G. (2011). A Mediterranean Sea level reconstruction (1950-2008) with error budget estimates. *Global and Planetary Change*. 79(1-2), 118-133.

Cazenave, A. Bonnefond, P., Mercier, F., Dominh, K., & Toumazou, V. (2002). Sea level variations in the Mediterranean Sea and Black Sea from satellite altimetry and tide gauges. *Global and Planetary Change*. 34(1-2), 59-86.

Cazenave, A., Cabanes, C., Dominh, K., & Mangiarotti, S. (2001). Recent Sea Level Change in the Mediterranean Sea Revealed by Topex/Poseidon Satellite Altimetry. *Geophysical Research Letters*. 28(8), 1607-1610.

Crosetto, M., Monserrat, O., Iglesias, R., & Crippa, B. (2010). Persistent scatterer interferometry: Potential, limits and initial C- and X-band comparison. *Photogrammetric Engineering and Remote Sensing*. 76(9), 1061-1069.

Cutrona, L. J. (1990). Synthetic aperture radar. *Radar Handbook*, second edition, ed. M. Skolnik, McGraw-Hill, New York. Chapter 21, 24 pages.

Dawoud, M. A., Darwish, M. M., El-Kady, M. M. (2005). GIS-Based Groundwater Management Model for Western Nile Delta. *Water Resources Management*. 19, 585-604. doi: 10.1007/s11269-005-5603-z.

Defense Mapping Agency (DMA). (1993). Map series 1501, sheets NH-35-4, 35-5, 36-1, 36-2, 36-5, 36-6, and 36-9. United States Government, Washington (charts).

Delft Institute for Earth-oriented Space Research. (2008). Envisat precise orbits (EIGEN-CG03C orbits). Site created by Remko Scharroo and maintained by Eelco Doornbos. http://www.deos.tudelft.nl/ers/precords/orbits/.

Delft Institute for Earth-oriented Space Research (DEOS). (2008). *Envisat precise orbits (EIGEN-CG03C orbits)*. Site created by Remko Scharroo and maintained by Eelco Doornbos. http://www.deos.tudelft.nl/ers/precords/orbits.

Desnos, Y.-L., Buck, C., Guijarro, J., Suchail, J.-L., Torres, R., & Attema, E. (2010). ASAR – Envisat's Advanced Synthetic Aperture Radar: Building on ERS Achievements towards Future Earth Watch Missions. *ESA Bulletin 102 – May 2010*. 91-100.

Dolson, C. J., Shaan, V. M., Matbouly, S., Harwood, C., Rashed, R., & Hammouda, H. (2001). The petroleum potential of Egypt. Downey, W. M., Threet, C. J., & Morgan, A. W. (Eds.) *Petroleum of the twenty-first century*. Memoir No. 74. American Association of Petroleum Geologists. Tulsa, Oklahoma. 453-482.

Dubois, P. C., van Zyl, J., & Engman, T. (1995). Measuring Soil Moisture with Imaging Radars. *IEEE Transactions on Geoscience and Remote Sensing*. 33(4), 915-926.

Egyptian General Petroleum Corporation (EGPC). (1994). Nile Delta north Sinai fields, discoveries and hydrocarbon potentialities (as comprehensive overview). EGPC-Cairo, Egypt. 387 pages.

El Banna, M. M. & Frihy, O. E. (2009). Human induced changes in the geomorphology of the northeastern coast of the Nile delta, Egypt. *Geomorphology*. 107(1-2), 72-78.

El-Askary, H. & Kafatos, M. (2008). Dust storm and black cloud influence on aerosol optical properties over Cairo and the Greater Delta region, Egypt. *International Journal of Remote Sensing*. 29(24), 7199-7211.

Elassiouti, I. M. (1983). Egypt's water resources. Elassiouti, I. M. & Marks, D. M. (Eds.) *Water Resources Planning in Egypt.* Ministry of Irrigation, Cairo. 15-19.

Eldardir, M. (1994). Sedimentation in Nile High Dam Reservoir, 1987-1992, and sedimentary futurologic aspects. *Sediment*. 2, 23-39.

ESRI. (1999). World1999, Satellite Imagery – eSAT, i-cubed, 19990115.

European Space Agency (ESA). (2002). Envisat Instruments. https://earth.esa.int/instruments/.

European Space Agency (ESA). (2008). ERS-2 InSAR Restored to Life: Zero-Gyro Mode and Tandem Operation with ENVISAT. *The Living Planet* [Brochure]. 1-15.

European Space Agency (ESA). (2012a). ENVISAT. http://www.esa.int/Our_Activities/Operations/Envisat.

European Space Agency (ESA). (2012b). RADAR and SAR Glossary Table 5.2. https://earth.esa.int/handbooks/asar/CNTR5-2.htm.

European Space Agency (ESA). (2013). MERIS Products. https://earth.esa.int/instruments/meris/data-app/dataprod.html.

European Space Agency (ESA), Planetary Visions, Centre for the Observation and Modeling of Earthquakes, Volcanoes and Tectonics (COMET+), Natural Environment Research Council (NERC), & Japan Aerospace Exploration Agency (JAXA). (2013). Africa's Ups and Downs [Video]. http://www.esa.int/Our_Activities/Observing_the_Earth/Highlights/Africa_s_ups_and_downs.

Favez, O., Cachier, H., Sciare, J., Alfaro, S. C., El-Araby, T. M., Harhash, M. A., & Abdelwahab, M. M. (2008). Seasonality of major aerosol species and their transformations in Cairo megacity. *Atmospheric Environment*. 42(7), 1503-1516.

Ferretti, A., Prati, C., & Rocca, F. (2000). Nonlinear subsidence rate estimation using permanent scatterers in differential SAR interferometry. *IEEE Transactions on Geoscience and Remote Sensing*. 39(1), 8-20.

Ferretti, A., Prati, C., & Rocca, F. (2001). Permanent Scatterers in SAR Interferometry. *IEEE Transactions on Geoscience and Remote Sensing*. 39(1), 8-20.

Foster, S. S. D. & Chilton, P. J. (2003). Groundwater: the processes and global significance of aquifer degradation. *Philosophical Transactions: Biological Sciences*. 358(1440), 1957-1972.

Freeman, T. & Wong, A. (1996). What is Imaging Radar? http://southport.jpl.nasa.gov/GRFM/cdrom/2b/DOCS/HTML/IMGV3.HTM.

Frihy, O. E., Nasr, S. M., El Hattab, M. M., & El Raey, M. (1994). Remote sensing of beach erosion along the Rosetta promontory, northwestern Nile delta, Egypt. *International Journal of Remote Sensing*. 15(8), 1649-1660.

Goldstein, R. M., Zebker, H. A., & Werner, C. L. (1988). Satellite radar interferometry: Two-dimensional phase unwrapping. *Radio Science*. 23(4), 713-720.

Hamza, W. (2001). Mediterranean Forecasting System Pilot Project UALEX-FS-DES, final scientific report. MFSPP-ISAO-CRN-EU. Project. 172 pages.

Hooper, A. & Delft Institute of Earth Observation and Space Systems (DEOS). (2009). StaMPS/MTI Manual (Version 3.1). 29 pages.

Hooper, A., Segall, P., & Zebker, H. (2007). Persistent scatterer InSAR for crustal deformation analysis, with application to Volcán Alcedo, Galápagos. *Journal of Geophysical Research*, 112(B07407). doi: 10.1029/2006JB004763.

Hooper, A., Stanford University, University of Iceland, & Delft University of Technology. (2009). StaMPS/MTI (Version 3.1) [Software]. http://radar.tudelft.nl/~ahooper/stamps.

Hooper, A. & Zebker, H. (2007). Phase unwrapping in three dimensions with applications to InSAR time series. *Journal of the Optical Society of America A*. 24, 2737-2747.

Hooper, A., Zebker, H., Segall, P., & Kampes, B. (2004). A new method for measuring deformation on volcanoes and other non-urban areas using InSAR persistent scatterers. *Geophysics Research Letters*. 31(23), 1-5.

Ibrahim, Y. A. E., Nasr, N. E.-S., Ghalab, M. E.-S., & Abd El-Hakim, M. S. (1994). *Geography of Egypt* (in Arabic). General Egyptian Organization for Books, Egypt.

Kamel, H., Eita, T., & Sarhan, M. (1988). Nile Delta hydrocarbon potentialities. *14th Exploration and production conference, EGPC*. Cairo. 485-503.

Kampes, B. M., Hanssen, R. F., & Perski, Z. (2003). Radar interferometry with public domain tools. *Proceedings from FRINGE*. http://doris.tudelft.nl/Literature/kampes03b.pdf.

Karnevi, S., Dean, E., Carter, D. J. Q., & Hartley, S. S. (1993). Envisat's Advanced Synthetic Aperture Radar: ASAR. *ESA Bulletin*. 76, 30-35.

Kohlhase A. O., Feigl, K. L., Massonnet, D. (2003). Applying differential InSAR to orbital dynamics: a new approach for estimating ERS trajectories. *Journal of Geodesy*. 77, 493-502. doi: 10.1007/s00190-003-0336-3.

Li, T., Liu, J., Liao, M., & Xia, Y. (2006). ENVISAT ASAR orbit error analysis and case study. *Proceedings from SPIE 6419, Geoinformatics 2006: Remotely Sensed Data and Information.* 28 October 2006. doi: 10.1117/12.713418.

Lin, Q., Vesecky, J. F., & Zebker, H. A. (1994). Phase unwrapping through fringe-line detection in synthetic aperture radar interferometry. *Applied Optics*. 33, 201-208.

Lombardini, F. (1996). Absolute phase retrieval in a three-element synthetic aperture radar interferometer. *Proceedings from the CIE International Conference of Radar*. 08 October 1996 – 10 October 1996. 309-312.

Lopes, A., Nezry, E., Touzi, R., & Laur, H. (1993). Structure detection and statistical adaptive speckle filtering in SAR images. *International Journal of Remote Sensing*. 14(9), 1735-1758.

Mahmoud, S., Reilinger, R., McClusky, S., Vernant, P., & Tealeb, A. (2005). GPS evidence for northward motion of the Sinai Block: Implications for E. Mediterranean tectonics. *Earth and Planetary Science Letters*. 238, 217-224.

Marriner, N., Flaux, C., Morhange, C., & Kaniewski, D. (2012). Nile Delta's sinking past: Quantifiable links with Holocene compaction and climate-driven changes in sediment supply? *Geology*. 40(12), 1083-1086.

Massonnet, D., Rossi, M., Carmona, C., Adragna, F., Peltzer, G., Feigl, K., & Rabaute, T. (1993). The displacement field of the Landers earthquake mapped by radar interferometry. Nature. 364, 138-142. doi: 10.1038/364138a0.

Massonnet, D., Briole, P., & Arnaud, A. (1995). Deflation of Mount Etna monitored by spaceborne radar interferometry. Nature. 375, 567-570. doi:10.1038/375567a0.

McGraw-Hill Concise Encyclopedia of Science & Technology. (1984). Troposphere (entry).

Medina, C., Gomez-Enri, J., Alonso, J. J., & Villares, P. (2010). Water volume variations in Lake Izabal (Guatemala) from in situ measurements and ENVISAT Radar

Altimeter (RA-2) and Advanced Synthetic Aperture Radar (ASAR) data products. *Journal of Hydrology*. 382(1-4), 34-48.

Meijering, E. & Unser, M. (2003). A Note on Cubic Convolution Interpolation. *IEEE Transactions on Image Processing*. 12(4), 477-479.

National Geodetic Laboratory (NGL) (2013). Station ID: ALE1 Time Series Data. Data processed by Geoffrey Blewitt, Nevada Geodetic Lab. http://geodesy.unr.edu/NGLStationPages/stations/ALE1.sta.

Poscolieri, M., Parcharidis, I., Foumelis, M. & Rafanelli, C. (2011). Ground deformation monitoring in the Greater Cairo Metropolitan Region (Egypt) by SAR Interferometry. *Environmental Semeiotics*. 4(3), 17-45.

Rayan, M. A. & Djebedjian, B. (2005). Egypt's Water Demand, Supply and Management Policies. http://www.academia.edu/2085529/Egypts_Water_Demand_Supply_and_Management_Policies. 24 pages.

Research Institute for Groundwater (RIGW), Water Research Center (WRC), Ministry of Public Works and Water Resources (MPWWR), & Arab Republic of Egypt. (1992). Hydrogeological Map of Egypt: Nile Delta (1st ed.). Scale 1:500,000.

Resti, A., Benveniste, J., Roca, M., Levrini, G., & Johannessen, J. (1999). The Envisat Radar Altimeter System (RA-2). *ESA Bulletin*. 98. 8 pages.

Ross, D. A. & Uchupi, E. (1977). The structure and sedimentary history of the southeastern Mediterranean Sea-Nile Cone area. *AAPG Bulletin*. 61, 872-902.

RWE Dea Egypt. (2013). Worldwide Operations: Egypt. http://www.rwe.com/web/cms/en/54970/rwe-dea/operations-worldwide/operations/egypt/.

Said, R., Bentz, F. P., & Hughes, J. B. (1981). The Geological Evolution of the River Nile (6th edition). New York: Springer-Verlag. 151 pages.

Sarmap. (2013). ENVI SARscape (Version 5.0) [Software]. http://www.sarmap.ch.

Schlumberger. (1984). Geology of Egypt. Paper presented at the *Well Evaluation Conference*. Schlumberger, Cairo, Egypt. 1-64.

Sestini, G. (1989). Nile Delta: depositional environments and geological history. Pickering, K. & Whateley, T. (Eds.) *Deltas: sites and traps for fossil fuel. Geological Society of London Special Publication*. Blackwell Scientific Publications, London. 41, 99-128.

Sestini, G. (1992). Implications of climatic changes for the Nile delta. Jeftic, L., Milliman, J. D., & Sestini, G. (Eds.) *Climatic Change and the Mediterranean*. Edward Arnold, New York, 535-601.

Sharaf El Din, S. H. (1977). Effect of the Aswan High Dam on the Nile flood and on the estuarine and coastal circulation pattern along the Mediterranean Egyptian coast. *Limnology and Oceanography.* 22, 194-207.

Stanley, D. J. (1990). Recent subsidence and northeast tilting of the Nile delta, Egypt. *Marine Geology*. 94(1-2), 147-154.

Stanley, D. J. (1996). Nile delta: extreme case of sediment entrapment on a delta plain and consequential coastal land loss [Letter Section]. *Marine Geology*. 189-195.

Stanley, D. J. & Warne, A. G. (1993). Nile Delta: Recent Geological Evolution and Human Impact. *Science*. 260(5108), 628-634.

Stanley, D. J. & Warne, A. G. (1998). Nile Delta in its destructive phase. *Journal of Coastal Research*. 14, 794-825.

Stanley, D. J., McRea, Jr., J. E., & Waldron, J. C. (1996). Nile Delta Drill Core and Sample Database for 1985-1994: Mediterranean Basin (MEDIBA) Program. *Smithsonian Contributions to the Marine Sciences*. No. 37, 435 pages.

Telespazio France. (2012). Eoli-sa (Version 9.1.5) [Software]. http://earth.esa.int/EOLi/EOLi.html.

Telford, W.M., Geldart, L.P., & Sheriff, R.E. (1990). Applied Geophysics (2nd ed.). Cambridge University Press. 792 pages.

U. S. Geological Survey (USGS). (2013). Earthquake Hazards Program: Earthquake Archive Search. http://earthquake.usgs.gov/earthquakes/search/.

United Nations Statistical Division (ENSD). (2013). UN Data: A world of information. http://data.un.org/Data.aspx?d=POP&f=tableCode%3A240.

Vandr, C., Cramer, B., Gerling, P., & Winsemann, J. (2007). Natural gas formation in the western Nile delta (Eastern Mediterranean): Thermogenic versus microbial. *Journal of Organic Geochemistry*. 38, 523-539.

White, K. & El Asmar, H. M. (1999). Monitoring changing position of coastlines using Thematic Mapper imagery, an example from the Nile Delta. *Geomorphology*. 29(1-2), 93-105.

Wolff, C. (1998). Synthetic Aperture Radar. http://www.radartutorial.eu/20.airborne/ab07.en.html.

Yakoub, N. G. R. (1996). Conjunctive use of ground and surface water in the Middle East. *First International Water Technology Conference* (IWTC '96), 26-29 February, Alexandria, Egypt, 199-208.

Yu, C., Loureiro, C., Cheng, J.-J., Jones, L. G., Wang, Y. Y., Chia, Y. P., & Faillace, E. (1993). Data collection handbook to support modeling impacts of radioactive material in soil. *RESRAD Data Collection Handbook*. http://web.ead.anl.gov/resrad/documents/data_collection.pdf. 172 pages.

Zaghloul, Z. M., Elgamal, M. M., Shaaban, F. F., & Yossef, A. F. A. (2001). Plates interactions and petroleum potentials in the Nile Delta. Zaghloul, Z. & El-Gamal, M. (Eds.) *Deltas (ancient and modern)*. 41-53.

Zaghloul, Z. M., Taha, A. A., & Gheith, A. M. (1977). Microfacies studies and paleoenvironment trends on the subsurface sediments of Kafr El Sheikh well No. 1, Nile Delta area. *Bulletin of Mansoura University*. 5, 113-138.

Zebker, H. A., Rosen, P. A., & Hensley, S. (1997). Atmospheric effects in interferometric synthetic aperture radar surface deformation and topographic maps. *Journal of Geophysical Research*. 102(B4), 7547-7563.

Zekster, S., Loáiciga, H. A., & Wolf, J. T. (2005). Environmental impacts of groundwater overdraft: selected case studies in the southwestern United States. *Environmental Geology*. 47(3), 396-404.

Zink, M. (2002). Introduction to the ASAR calibration/validation project. *The Envisat calibration review*. Noordwijk (The Netherlands). 8 pages.